8-9-2014

GROWTH, FABRICATION AND CHARACTERIZATION OF $Cu_2ZnSn(S_xSe_{1-x})_4$ PHOTOVOLTAIC ABSORBER AND THIN-FILM HETEROJUNCTION SOLAR CELLS

Sandip Das
University of South Carolina - Columbia

GROWTH, FABRICATION AND CHARACTERIZATION OF $Cu_2ZnSn(S_xSe_{1-x})_4$ PHOTOVOLTAIC ABSORBER AND THIN-FILM HETEROJUNCTION SOLAR CELLS

by

Sandip Das

Bachelor of Engineering
Indian Institute of Engineering, Science and Technology, Shibpur, 2004

Master of Engineering
University of South Carolina, 2012

Submitted in Partial Fulfillment of the Requirements

For the Degree of Doctor of Philosophy in

Electrical Engineering

College of Engineering and Computing

University of South Carolina

2014

Accepted by:

Krishna C. Mandal, Major Professor

Guoan Wang, Committee Member

Herbert L. Ginn, Committee Member

Richard D. Adams, Committee Member

Raghu N. Bhattacharya, Committee Member

Lacy Ford, Vice Provost and Dean of Graduate Studies

DEDICATION

This dissertation is dedicated to my beloved *family and friends*. A special gratitude to my loving parents and my brother, whose relentless encouragement and support during this extraordinary odyssey has helped me to put my best efforts toward this research work. I also dedicate this dissertation to many of my friends who have supported me throughout the tenure of my doctoral studies.

ACKNOWLEDGEMENTS

I would like to thank my advisor Dr. Krishna C. Mandal for giving me the opportunity to work with him and providing me a world-class research environment. It would not have been possible to carry out this research work without his continued support and guidance. I would also like to thank my dissertation committee member Dr. Raghu N. Bhattacharya from National Renewable Energy Laboratory (NREL) for his valuable suggestions throughout the duration of this work that guided me to the successful completion of this research. Also, I would like to thank rest of my dissertation committee members, Dr. Guoan Wang, Dr. Herbert L. Ginn, and Dr. Richard D. Adams for taking the time to oversee my research and their strong support of my work.

I would also like to thank the following people for their contributions to the research performed in this work:

- Dr. Sandeep K. Chaudhuri (Electrical Engineering, University of South Carolina) for his assistance in conducting defect studies on thin-film $Cu_2ZnSn(S_xSe_{1-x})_4$ solar cells by deep level transient spectroscopy (DLTS).
- Dr. Ramesh M. Krishna (Electrical Engineering, University of South Carolina) for his assistance in the Cu_2ZnSnS_4 bulk crystal growth by vertical gradient freeze technique and simulation of furnace temperature profile.
- Dr. Shuguo Ma (College of Engineering and Computing, University of South Carolina) for performing the XPS characterization.

- Dr. Lingling Zhang and Dr. Kevin Huang (Mechanical Engineering, University of South Carolina) for their assistance and support in conducting Impedance Spectroscopy (IS) measurements.
- Yating Mao and Dr. Harry J. Ploehn (Chemical Engineering, University of South Carolina) for their assistance and support in conducting Atomic Force Microscopy (AFM) measurements.
- Dr. Kevin Daniels and Dr. Christopher T. Williams (Electrical / Chemical Engineering, University of South Carolina) for their assistance and support in conducting Raman spectroscopy measurements.
- The staffs of Electron Microscopy Center (EMC) at the University of South Carolina for their assistance with Scanning Electron Microscopy (SEM) and Energy Dispersive X-ray Spectroscopy (EDX) studies.

Finally, I would like to thank all those faculty members and staffs in the Electrical Engineering department at the University of South Carolina whose cumulative efforts have contributed to the successful completion of my doctoral research. Without their contributions, this work would have been impossible to perform.

ABSTRACT

Current thin-film solar cell technologies based on $CuIn_xGa_{1-x}Se_2$ (CIGS) and CdTe photo-absorber materials use rare and expensive elements, such as In, Te, Ga, and toxic Cd which severely limit the mass production and deployment of these solar cells. Thus, a major research effort is focused toward the development of new photovoltaic (PV) absorber materials comprising of earth-abundant, low-cost, and environmentally benign constituent elements that can support terawatt (TW)-scale PV generation in the near future and be economically sustainable. Cu-based I_2-II-IV-VI_4 quaternary kesterite compound $Cu_2ZnSn(S_xSe_{1-x})_4$ (CZTSSe) have recently emerged as a potential photo-absorber material for thin-film solar cells. All constituent elements in CZTSSe are abundant in earth's crust, are much cheaper and possess no acute toxicity. CZTSSe is an intrinsically p-type material with a large optical absorption coefficient ($\alpha>10^4$ cm^{-1}) and exhibits a tunable direct optical bandgap in the range of 1.0 eV $\leq E_g \leq$ 1.5 eV corresponding to chalcogen ratios of $0 \leq x \leq 1$. The theoretical Shockley-Queisser efficiency limit for a single junction CZTSSe solar cell is estimated to be ~32% – similar to that of CIGS solar cells. All these merits make CZTSSe an ideal photo-absorber material for thin-film solar cells.

In this dissertation, a comprehensive investigation is undertaken on the growth and characterization of $Cu_2ZnSn(S_xSe_{1-x})_4$ photovoltaic absorber material followed by thin-film solar cell fabrication and cell characterization. CZTSSe films were fabricated by a vacuum-based two-step process of ZnS/Cu/Sn stacked precursor layer deposition on bi-layer molybdenum (Mo)-coated soda-lime glass (SLG) substrates via thermal evaporation and

successive annealing of the precursor stacks under a mixed sulfur and selenium vapor at 550°C. The heterojunction was formed by deposition of n-CdS layer on top of p-CZTSSe absorber film via a low-cost chemical bath deposition (CBD) technique. The structural, compositional and morphological characterization of the CZTSSe films were carried out by Raman spectroscopy, scanning electron microscopy (SEM), energy dispersive X-ray spectroscopy (EDX), X-ray photoelectron spectroscopy (XPS), and atomic force microscopy (AFM). The best solar cell was obtained with a Cu-poor and slightly Zn-rich absorber composition corresponding to elemental ratios of Cu/(Zn+Sn) = 0.773, Zn/Sn = 1.13 and S/(S+Se) = x = 0.58. Thickness of the CZTSSe film was measured to be 1.3-1.4 μm with an estimated bandgap of ~1.3 eV. The photovoltaic performance of the fabricated cells were evaluated under simulated AM1.5G (100 mW/cm^2) solar radiation. The champion cell exhibited an open-circuit voltage (V_{OC}) of 506 mV, a short-circuit current density (J_{SC}) of 22.92 mA/cm^2, and a fill-factor (FF) of 35% resulting in a total area efficiency (η) of 4.06% without any antireflection coating.

Performance of the fabricated solar cells were found to be limited by high series resistance (R_S), low shunt resistance (R_{Sh}), and poor fill factor (FF). The sources of high series resistance were attributed to the small multi-grain microstructure of the polycrystalline CZTSSe film, presence of micro air-voids, and a $Mo(SSe)_x$ interfacial layer at the Mo back contact. AFM studies revealed micro-pores on the film surface which act as low resistance shunt paths and are attributed to the source of low shunt resistance. Impedance spectroscopy were performed on the solar cells to model and extract the equivalent AC circuit parameters. Fitting of the experimental results showed the presence of a blocking barrier at the back contact and a recombination center resembling a constant

phase element (CPE). Temperature dependent illuminated current-voltage (J-V) studies indicated a major recombination phenomena occurring at the heterojunction interface corresponding to an activation energy of 1.12 eV. Further investigation of the electronic defect levels in the fabricated solar cells have been carried out by current-mode deep level transient spectroscopy (I-DLTS). Two dominant deep acceptor defects at E_v+0.12 eV, and E_v+0.32 eV have been observed and were identified as the Cu_{Zn}(-/0) and Cu_{Sn}(2-/-) antisites respectively.

TABLE OF CONTENTS

LIST OF TABLES

LIST OF FIGURES

LIST OF SYMBOLS

V	Voltage (V).
V_{OC}	Open-circuit voltage (V).
I	Current (mA).
J	Current density (mA/cm^2).
J_{SC}	Short-circuit current density (mA/cm^2).
J_0	Reverse saturation current density (mA/cm^2).
n	Ideality factor.
q	Electronic charge (C).

LIST OF ABBREVIATIONS

AFM ..... Atomic Force Microscopy

AM0 ..... Air Mass 0

AM1.5 ..... Air Mass 1.5

ASTM ..... American Society for Testing and Materials

at% ..... Atomic Percentage

CIGS ..... $CuIn_xGa_{1-x}Se_2$

CZTS ..... Cu_2ZnSnS_4

CZTSe ..... $Cu_2ZnSnSe_4$

CZTSSe ..... $Cu_2ZnSn(S_xSe_{1-x})_4$

DFT ..... Density Functional Theory

EDS ..... Energy Dispersive X-ray Spectroscopy

FRA ..... Frequency Response Analyzer

FWHM ..... Full Width at Half Maxima

IS ..... Impedance Spectroscopy

SEM ..... Scanning Electron Microscopy

SCCM ..... Standard Cubic Centimeters per Minute

SLG ..... Soda-Lime Glass

TFSC ..... Thin-Film Solar Cell

XPS ..... X-ray Photoelectron Spectroscopy

ZR ..... Zone Refined

UHP ..... Ultra High Purity

CHAPTER 1: INTRODUCTION

1.1 OVERVIEW OF THE DISSERTATION

In this dissertation, a comprehensive investigation has been undertaken on the growth and characterization of $Cu_2ZnSn(S_xSe_{1-x})_4$ photovoltaic absorber material, fabrication and characterization of thin-film solar cell, and identification of the cell performance limiting factors that may lead to further improvement of CZTSSe-based photovoltaic devices.

This dissertation is divided into six chapters. Chapter 1 provides a background of the existing photovoltaic (PV) technologies and discuss the issues associated with the current technologies. The merits of $Cu_2ZnSn(S_xSe_{1-x})_4$ as a photo-absorber material for thin-film solar cells are then scrutinized in this context. Important general properties of CZTSSe, such as crystal structure, ternary phase diagram, composition sensitivity to photovoltaic performance, formation of secondary phases, and intrinsic point defects are then discussed based on the review of published literature. An introduction to the standard solar spectra for photovoltaic measurements (AM0 and AM1.5) is included along with a discussion on the maximum theoretical efficiency achievable with different PV materials under terrestrial solar radiation. Finally, at the end of this chapter, the fundamental operating principle of heterojunction solar cells is explained.

Chapter 2 details the fabrication method and the characterization results of the polycrystalline CZTSSe photo-absorber films. Crystal Structure, composition, and morphology of the films were studied by Raman spectroscopy, scanning electron

microscopy (SEM), energy dispersive X-ray spectroscopy (EDX), X-ray photoelectron spectroscopy (XPS), and atomic force microscopy (AFM). Characterization results are presented for the CZTSSe absorber film yielding the best photovoltaic performance (η=4.06%). A high-efficiency (η=7.05%) CZTSe solar cell received from NREL was used as a reference.

Chapter 3 presents the details of complete solar cell fabrication process, the device structure, and electrical characterization results. Photovoltaic performance of the solar cells were evaluated under simulated AM1.5G solar spectrum and diode parameters were extracted from dark current-voltage characteristics.

Chapter 4 focuses on the impedance spectroscopy measurement and AC equivalent circuit analysis. Impedance analysis provides valuable insight into the device operation. Small signal AC circuit parameters were extracted by fitting of the experimental data and a major recombination phenomena was identified in the device characterized by a frequency dependent constant phase element.

Chapter 5 presents the investigation of electronic defect levels in the CZT(S,Se) solar cells by current-mode deep level transient spectroscopy (I-DLTS). Two deep acceptor levels were identified from the I-DLTS measurements in the fabricated CZTSSe solar cells. The possible impact of the defects on the cell performance are discussed with reference to the high performance CZTSe cell.

Chapter 6 presents the growth and characterization of single-phase $Cu_2ZnSn(S_xSe_{1-x})_4$ bulk crystals employing a novel vertical gradient freeze (VGF) method. Bulk CZTSSe absorber materials were characterized by XRD, Raman spectroscopy, EDS, and XPS. It was found that VGF technique promises to produce large volume, high quality CZTSSe

crystals at reduced cost. The detailed crystal growth technique and characterization results are presented.

Finally, Chapter 7 concludes the research presented in this work, and provides suggestions for the future work.

1.2 Introduction to Photovoltaic Technologies

Currently, about 80% of the world's energy demand is met by burning fossil fuels, such as coal, oil, and natural gas. These fuels produce greenhouse gases upon combustion causing significant environmental pollution and is the primary contributor to global warming and man-made climate change. In addition, all these energy sources have finite reserve in the earth's crust and are depleting fast. Solar energy is unlimited, non-polluting, and can provide a substantial fraction of the world's energy demand in the near future. In fact, the entire global energy demand can be met if only ~0.1% of the earth's surface area is covered with ~10% efficient solar cells. According to the international energy agency (IEA), photovoltaics (PV) is estimated to provide around 11% of global electricity production by 2050 and avoid 2.3 gigatonnes (Gt) of CO_2 emissions per year [1]. Thin-film solar cell technology is considered to play a major role to meet this terawatt (TW)-scale PV power demand at an affordable price.

Several photovoltaic technologies have been developed over the past 50 years for terrestrial applications. At present, crystalline silicon (c-Si) and multi-crystalline silicon (mc-Si) together holds the major market share (~85%) among all photovoltaic technologies. So far, c-Si solar cell technology has reached the highest photoconversion efficiency of 25%. However, PV grade Si is highly expensive and currently the major bottleneck to the mass deployment of photovoltaics as a primary renewable energy source

is the high cost of modules. Thin-film solar cell (TFSC) technology potentially reduces the cost of module fabrication. Unlike Si, the semiconductor light-absorbing material chosen for thin-film solar cells are direct bandgap with a large optical absorption co-efficient that can absorb the incident light much more efficiently and thus requires a very thin absorber layer (~1-3 μm) compared to Si (~300-400 μm). This reduces the material uses and the material cost significantly. Moreover, TFSC fabrication techniques allow large-area monolithic integration of individual solar cells allowing high-throughput roll-to-roll manufacturing which further cuts down the module fabrication cost making it significantly cheaper than Si-based modules. Also, there are several other advantages offered by thin-film solar cells compared to Si cells. Due to much less material use, thin-film solar cells are light weight and thus reduces logistical problems and cost of module support structures –a major advantage for building integrated photovoltaic (BIPV) installations. Also, thin-film solar cells can be fabricated on flexible substrates, such as plastics, aluminum/stainless steel foils that allows ultra-light weight portable modules to be fabricated for mobile power source applications.

Current benchmark TFSC technologies based on polycrystalline $CuIn_xGa_{1-x}Se_2$ (CIGS) and CdTe absorbers have reached record efficiencies of 20.8% and 19.6% for laboratory-scale devices and have already reached the commercial production stage [2]. However, several factors are hindering the mass-scale production and deployment of these solar cells resulting in a smaller market share of ~15% for TFSCs. Such factors include serious issues of toxicity, sky-rocketing material cost and/or low abundance of raw materials; which is predicted to severely limit the production and economic sustainability of these solar cells [3] [4] [5] [6] [7] [8] [9] [10]. Indium (In), gallium (Ga), and tellurium

(Te) supply have been categorized as 'critical' by the US Department of Energy (DOE) and the European Commission (EC) [11] [12]. Particularly, In supply for CIGS production could be stringent as more than 80% of In produced worldwide is consumed by the flat panel display (FPD) industry and with ever increasing demand of such displays, sustainability and economic viability of CIGS photovoltaic (PV) technology could be in great danger in upcoming years [13]. Also, due to the environmental health concerns, use of toxic cadmium (Cd) hinders the mass production and deployment of CdTe solar cells [14]. Thus, an intense research effort is focused toward the development of alternative thin-film solar absorber materials comprising of earth-abundant, low-cost, and non-toxic elements which can yield high efficiency devices, be economically competitive to the conventional energy sources, and support terawatt (TW)-scale PV generation in the near future.

Copper (Cu)-based I_2-II-IV-VI_4 quaternary kesterite compounds – Cu_2ZnSnS_4 (CZTS), $Cu_2ZnSnSe_4$ (CZTSe), and mixed chalcogenide $Cu_2ZnSn(S_xSe_{1-x})_4$ (CZTSSe) have emerged as the potential alternative to the existing CIGS, and CdTe absorbers in thin-film solar cells. CZTSSe is an attractive choice for thin-film solar cell absorber owing to its tunable direct bandgap of 1.0-1.5 eV with a large optical absorption coefficient ($\alpha>10^4$ cm^{-1}), and p-type conductivity [15] [16] [17] [18] [19] [20]. The constituent elements of CZTSSe are earth abundant, inexpensive, and environmentally benign. Reserve of Cu, Zn, Sn, and sulfur on earth's crust are 68 ppm, 79 ppm, 2.2 ppm, and 420 ppm respectively compared to 0.16 ppm of In, 0.15 ppm of Cd, and 0.001 ppm of Te [21]. The availability of Zn and Sn are about 500 and 14 times higher and the annual global production is 20 times and 340 times more compared to the scarce and expensive In [22]. Also, the Zn price

is nearly two orders and Sn price is one order of magnitude less than indium, while the In price is sharply rising [22] [23]. Abundance and recent cost of the constituent elements for CZTSSe, CIGS, and CdTe compounds are shown in Figure 1.1.

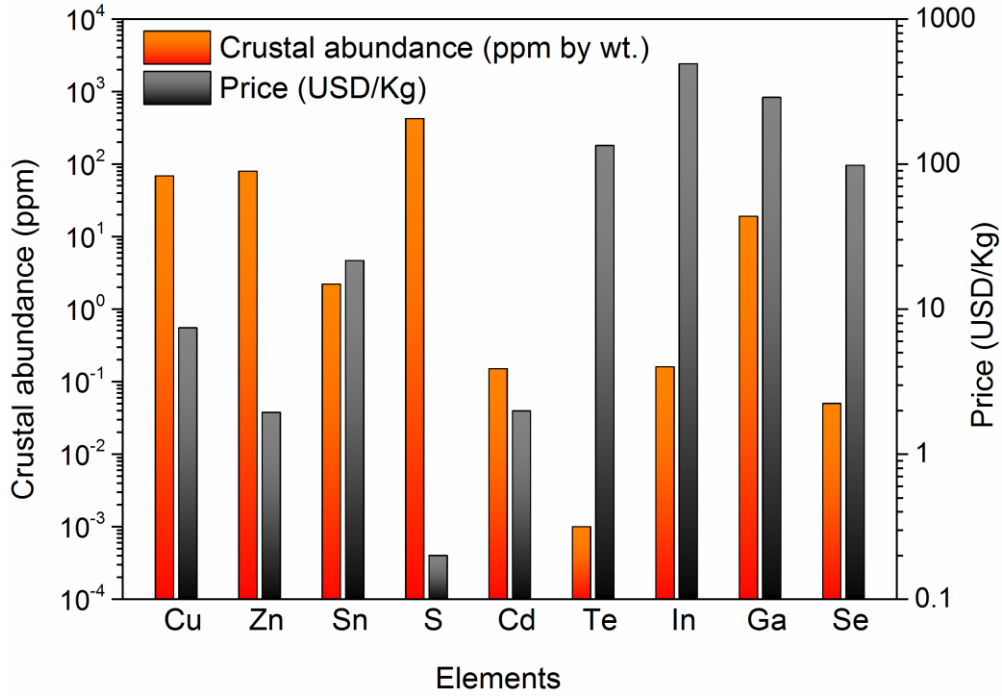

Figure 1.1. Crustal abundance and cost of constituent elements for CIGS, CdTe, and CZTSSe photo-absorber materials for thin-film solar cells.

Calculations according to the Schokley-Queisser photon balance equations have estimated the theoretical conversion efficiency of single-junction CZTSSe solar cells to be as high as 32.2% [24]. In the light of above mentioned advantages, CZTSSe shows extreme promise to be the ideal thin-film solar cell material for low-cost, sustainable, high-efficiency, and environment friendly PV technology.

1.3 General Properties of $Cu_2ZnSn(S_xSe_{1-x})_4$

1.3.1 Crystal Structure

$Cu_2ZnSn(S_xSe_{1-x})_4$ (CZTSSe) belongs to the I_2–II–IV–VI_4 quaternary material system with a crystal structure similar to the ternary chalcopyrite material $CuInSe_2$ (space group $I\bar{4}2d$) (Figure 1.2), in which one half of In atoms (group III) are replaced by Zn (group II) and other half by Sn atoms (group IV). CZTSSe crystallizes in two primary crystalline structures known as kesterite (space group $I\bar{4}$) and stannite (space group $I\bar{4}2m$) [25] [26] [27] [28]. These two crystal structures are very similar; both have cations located at tetrahedral sites but differ in the stacking arrangement of Cu and Zn atoms along the c-axis [26] [27] [28] [29] [30] [31]. The crystal structure and the atomic arrangements for the chalcopyrite, kesterite and stannite structures are illustrated in Figure 1.2.

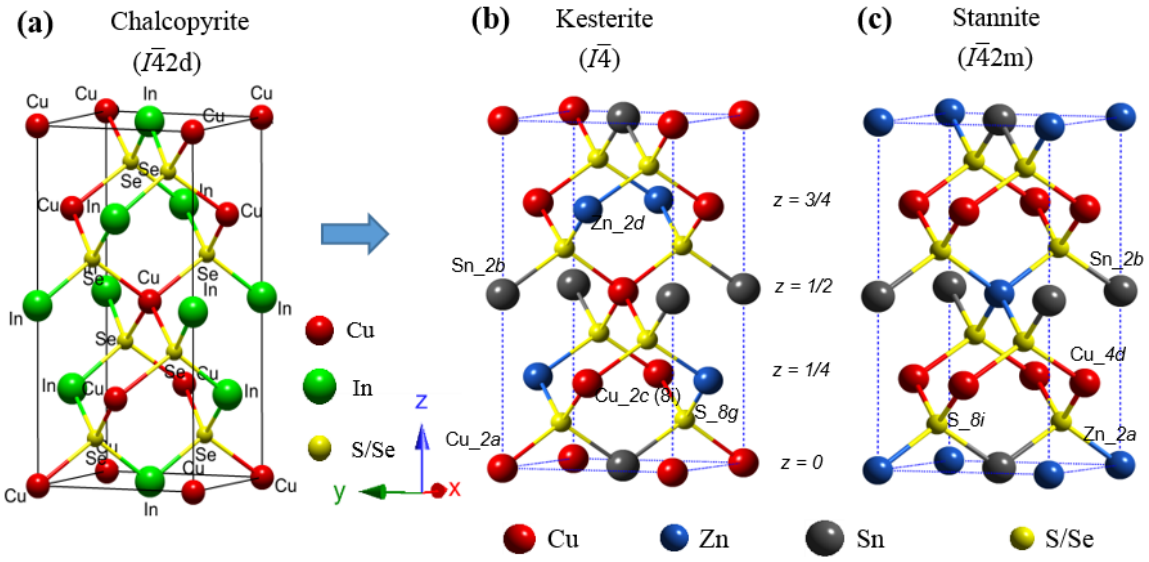

Figure 1.2. Crystal structures of (a) chalcopyrite $CuInSe_2$, (b) kesterite CZTSSe, and (c) stannite CZTSSe.

In kesterite structure, the cationic layers along the c-axis are arranged in Cu-Sn, Cu-Zn, Cu-Sn, and Cu-Zn fashion. One Cu atom is located at 2a position; Zn atom and the

other Cu atom are located at 2d and 2c positions respectively with corresponding Madelung potentials of -15.04 V, -21.88 V, and -15.21 V [32]. In stannite structure, a periodic arrangement of Zn-Sn cationic layer sandwiched in between Cu-Cu layers are repeated where both Cu atoms are located at 4d position and the Zn atom at 2a position with Madelung potentials of -15.30 V and -21.62 V respectively. Sn atom site is located at 2b position in both structures [32] [33]. Theoretical studies have predicted that the kesterite phase has slightly lower energy compared to the stannite phase and therefore should be thermodynamically more stable than the stannite counterpart [33] [34] [35] [36] [37] [38] [39] [40]. As predicted theoretically, most of the CZTS(Se) samples have been reported to have kesterite structure.

Due to the similar structural properties and isoelectronic nature of Cu^{+} and Zn^{2+}, it is very difficult to distinguish between the kesterite and stannite phases experimentally by X-ray diffraction. Recently, neutron diffraction [31] and anomalous diffusion [41] studies confirmed that CZTSSe compounds crystalizes in kesterite structure and is dominant at temperature <876°C. It is suggested that observations of stannite structure in CZT(S,Se) compounds could be due to partial disorders of Cu and Zn atom sites in the I-II (001) layer of kesterite phase [31] [42] [43]. This lattice disorder could be due to the formation of mixed kesterite and stannite phases during the crystallization process since there is only a small difference in the lattice parameters and the total energy of these two phases.

1.3.2 Phase Diagram

It is extremely challenging to grow pure single phase kesterite CZTS/CZTSe. CZT(S,Se) can be grown via solid state chemical reactions of Cu_2S, ZnS, and SnS_2 (or Cu_2Se, ZnSe, and $SnSe_2$). Due to the complexity of the quaternary material system, several

binary and ternary sulfides (or selenides) including Zn(S,Se), $Cu_x(S,Se)$, $Sn(S,Se)_x$, and $Cu_xSn(S,Se)_y$ phases can easily form during the absorber film fabrication which may adversely affect the photovoltaic performance of the resulting device. The ternary phase diagram of the Cu_2S-ZnS-SnS_2 (or Cu_2Se-ZnSe-$SnSe_2$) system exhibits very narrow region of stability for single phase kesterite CZTS/CZTSe crystals (Figure 1.3) [44] [45] [46] [47]. Kesterite structure is highly sensitive to composition compared to the chalcopyrite structure [48] [49] [50] [51]. Only 1–2% deviation from the ideal stoichiometric composition is allowed compared to ~ 4% deviation in chalcopyrites [52]. Also, the stability region of CZTSSe for Cu-rich condition in the chemical potential μ_{Sn}-μ_{Zn} diagram is about 0.1 eV wide [48] [49] [50] [51] [53] compared to the 0.5 eV wide stability region for chalcopyrite $CuInSe_2$ [54]. Based on ab-initio calculations and experimental results, it is considered that single phase kesterite is far more difficult to prepare compared to chalcopyrites.

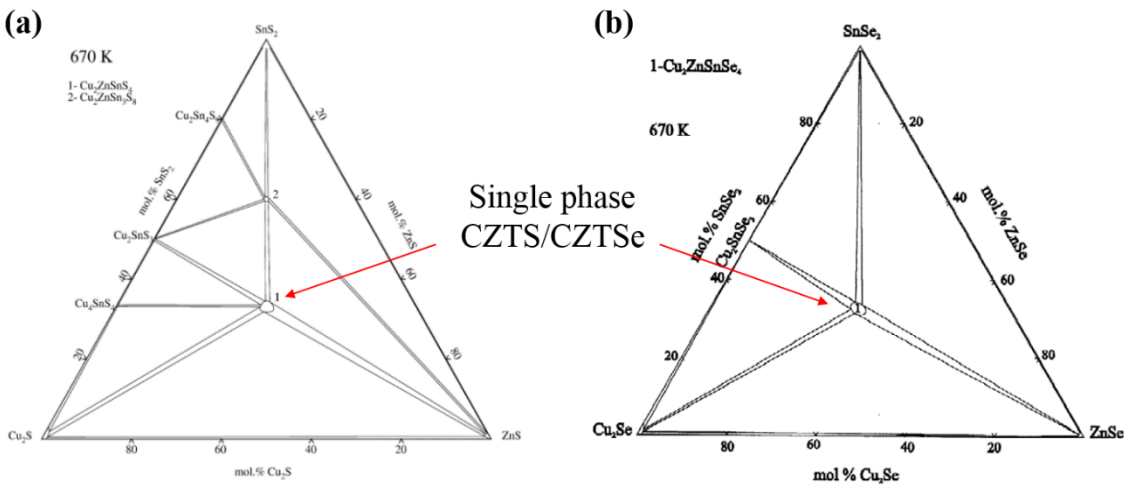

Figure 1.3. Phase diagrams of (a) Cu_2S-ZnS-SnS_2 [44], and (b) Cu_2Se-ZnSe-$SnSe_2$ pseudo-ternary systems at 670K [45].

1.3.3 Secondary Phases and Intrinsic Defects

High efficiency CZTSSe solar cells were found to have Cu-poor and slightly Zn-rich composition in general. It was observed that irrespective of the deposition technique or absorber preparation method, the best solar cells reported in the literature were obtained with an elemental ratio of ~0.8-0.9 for Cu/(Zn+Sn) and ~1.1-1.2 for Zn/Sn. During the absorber layer fabrication process, secondary phases such as Zn(S,Se) and $Cu_2Sn(S,Se)_3$ may form in the Zn-rich regime. Nagoya et al. [48] and Maeda et al. [55] have theoretically predicted ZnS to be the predominant impurity phase under the Cu-poor and Zn-rich growth condition with Cu_{Zn} antisite being the most stable defect in the entire stability region of CZTS [53].

Recently, the existence of ZnSe secondary phase in $Cu_2ZnSnSe_4$ films have been experimentally confirmed [56] [57]. Zn(S,Se) has a wider band gap and exhibits high resistivity and therefore is not considered to be responsible for reduced open-circuit voltage or reduced shunt resistance, but can lead to high series resistance of the solar cell [30] [56]. Other secondary phases, such as $Sn(S,Se)_x$, $Cu_x(S,Se)$, and $Cu_2Sn(S,Se)_3$ phases are considered to have more detrimental effect because of their lower band gap and high conductivity, which can significantly reduce the open-circuit voltage (V_{OC}) and decrease the shunt resistance (R_{Sh}) leading to inferior performance of the solar cell [42].

Defects play an important role in the resulting optoelectronic properties of semiconductor materials. There are thirteen possible isolated intrinsic point defects in kesterite CZTS structure that may form during the film/crystal growth including vacancies (V_{Cu}, V_{Zn}, V_{Sn}, and V_S), antisites (Cu_{Zn}, Zn_{Cu}, Cu_{Sn}, Sn_{Cu}, Zn_{Sn}, and Sn_{Zn}), and interstitial

defects (Cu_i, Zn_i, and Sn_i). Existence of point defects and deviation from the ideal stoichiometry is attributed to the intrinsic p-type conductivity of CZTSSe.

Several theoretical defect studies based on density functional theory (DFT)/first principle calculations have been employed to investigate the defect mechanism and formation energies of different possible point defects in kesterites [48] [49] [51] [53] [55] [58] [59] [60]. Chen and co-workers have carried out detailed theoretical studies of the defect characteristics in CZT(S,Se) [38] [53] [61] [62]. Out of the possible thirteen point defects mentioned above, the lowest five formation energies in ascending order correspond to Cu_{Zn}, V_{Cu}, Zn_{Sn}, V_{Zn}, and Cu_{Sn} respectively for Cu-poor composition.

All investigations converge to the general agreement that the acceptor defects, such as Cu_{Zn} or Cu_{Sn} antisites and the Cu vacancy (V_{Cu}) has lower energy of formation with the lowest formation energy for Cu_{Zn} antisite defect. The donor defects, such as the S vacancy (V_S) and the Zn_{Cu} antisite have much higher energy of formation. Such low formation energies of the acceptor defect levels, particularly Cu_{Zn} antisite suggests the favorable formation of acceptors and is generally attributed for the evolution of p-type characteristic of Cu_2ZnSnS_4 [63] [64] [65] [66] [67] [68] [69] [70] [71] and $Cu_2ZnSnSe_4$ [72] [73] [74] [75]. This explains why CZT(S,Se) had always been reported to be of p-type regardless of the deposition method and high efficiency solar cells have been reported to have Cu-poor and Zn-rich stoichiometry.

The Cu_{Zn} substitution occurs at the 2d site and Zn_{Cu} substitution occurs at the 2c site [76] [77]. The existence of charge-compensated electrically neutral defect complexes, such as $[Cu_{Zn}^{-} + Zn_{Cu}^{+}]^0$ and $[V_{Cu}^{-} + Zn_{Cu}^{+}]^0$ are also predicted for Cu-rich, Zn-poor and Cu-poor, Zn-rich CZTS respectively [49]. However, such electrically benign defect pairs

are believed to help in screening and electronic passivation of the deep levels, thus reducing the charge carrier recombination resulting in improved device performance [48] [53] [55].

1.4 THE SOLAR SPECTRUM

The solar radiation on the earth's outer space closely matches the black body radiation corresponding to ~5800 K. The solar spectrum is distributed over a wide range of wavelengths from deep ultraviolet to far infrared. As the sunlight passes through the atmosphere, various chemicals (e.g. O_3, H_2O, CO_2 etc.) absorb lights of certain wavelengths resulting in a solar spectrum with attenuated absorption lines on the earth's surface. Various standards for solar spectra have been developed by ASTM for the different amounts of solar radiation received at different altitudes on earth defined by the 'Air Mass' (AM). The solar spectrum on earth's outer space is defined by ASTM standard E490 which is used in PV measurements for extra-terrestrial applications, such as satellites etc. and is commonly referred to as AM0. For terrestrial applications, the PV measurement is carried out under the solar spectrum incident on the earth's surface designated as AM1.5G (global) based on the ASTM standard G173 [78]. The photovoltaic response of a solar cell is dependent on the bandgap of the semiconductor material used as the active photo-absorber. The AM0 and AM1.5G spectral distributions along with the absorption band edges of various photovoltaic materials are shown in Figure 1.4.

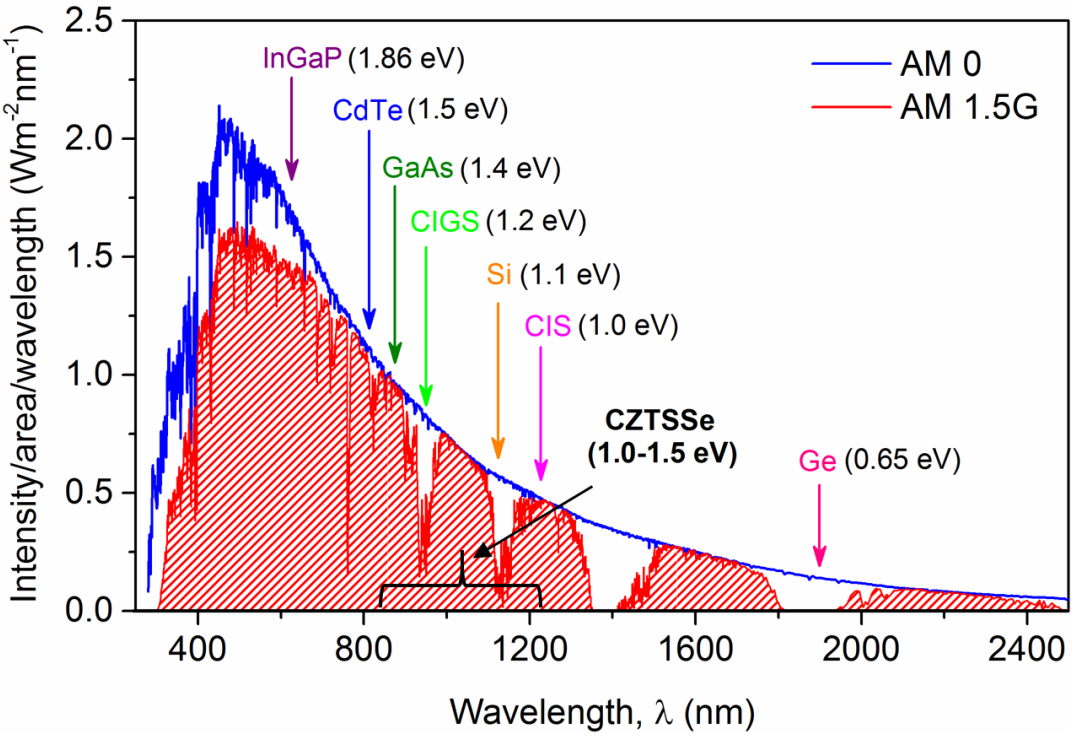

Figure 1.4. The solar spectrum outside the earth's atmosphere (AM0) and on the sea level (AM1.5G). Band edges of different PV absorber materials are marked by arrows.

Semiconductor materials with narrow bandgap can produce higher currents since it can be excited by light with longer wavelengths. However, the V_{OC} is limited due to the narrow bandgap. On the contrary, wide bandgap absorber materials can generate higher V_{OC} but the resulting current would be lower since only the high energy photons at shorter wavelengths can excite the electrons in these materials and therefore will only absorb a small fraction of the available solar spectrum. Hence, there is an optimum range of the absorber material's bandgap to obtain the best photoconversion efficiency. The limit of maximum theoretical efficiency of a single junction solar cell can be estimated from the detailed photon balance equations developed by Shockley and Queisser [24]. The maximum efficiency curve as a function of material bandgap is shown in Figure 1.5.

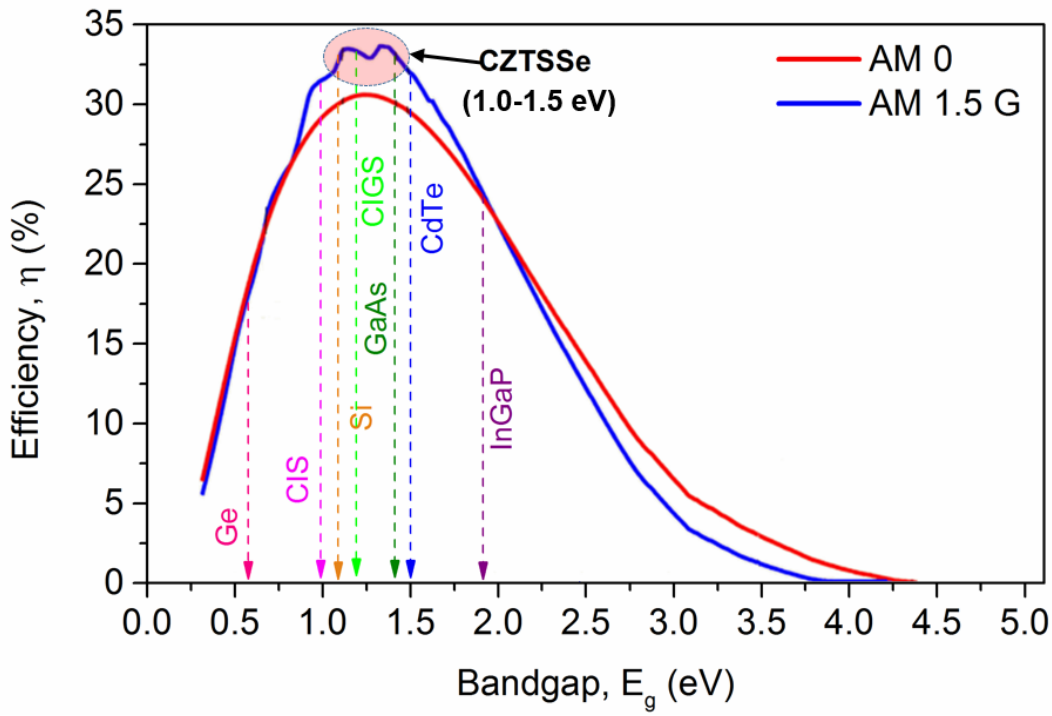

Figure 1.5. The maximum theoretical efficiency curves of a single junction solar cell as a function of photo-absorber bandgap calculated from Shockley-Queisser detailed photon balance equations.

The Shockley-Queisser efficiency limit of a solar cell can be estimated from these curves corresponding to the absorber material's bandgap. It is observed that the maximum theoretical efficiency can be achieved with a semiconductor having bandgap in the range of ~1.2-1.5 eV. It is clearly seen that the bandgap of CZTSSe falls in the range for highest photoconversion efficiency.

1.5 Heterojunction Solar Cell: Principle of Operation

The fundamental operating principle of a heterojunction solar cell is essentially the same as that of a homojunction Si solar cell except that the p-type and n-type materials are different. CZTSSe exhibits intrinsic p-type conductivity and n-CdS shows good band alignment with p-CZTSSe. Also, superior junction properties have been achieved using

CdS as the heterojunction partner in CIGS-based solar cells resulting in best performing devices in the past. Thus, CdS is most exclusively used as the n-type heterojunction partner for CZTSSe-based solar cells as well.

The energy band diagram of p-CZTS and n-CdS is shown in Figure 1.6 indicating the positions of conduction band minima (CBM) and valence band maxima (VBM) of each material. The standard literature values for electron affinity and bandgaps of CZTS and CdS have been used to draw the band diagram. After formation of the heterojunction, the equilibrium band diagram of the solar cell including the p-n junction is shown in Figure 1.7.

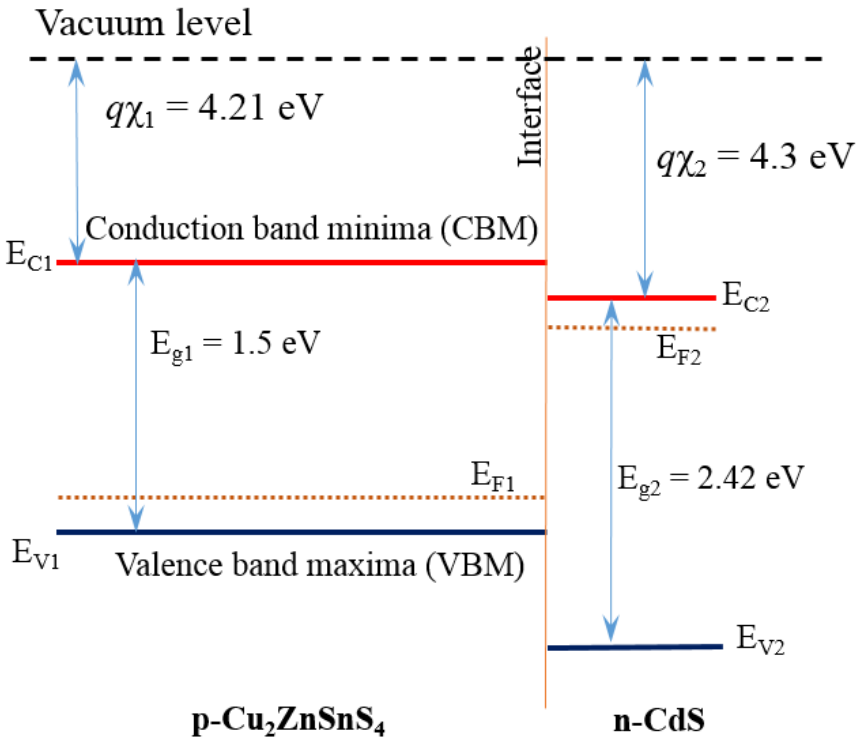

Figure 1.6. Energy band diagrams of isolated p-Cu_2ZnSnS_4 and n-CdS before the heterojunction formation.

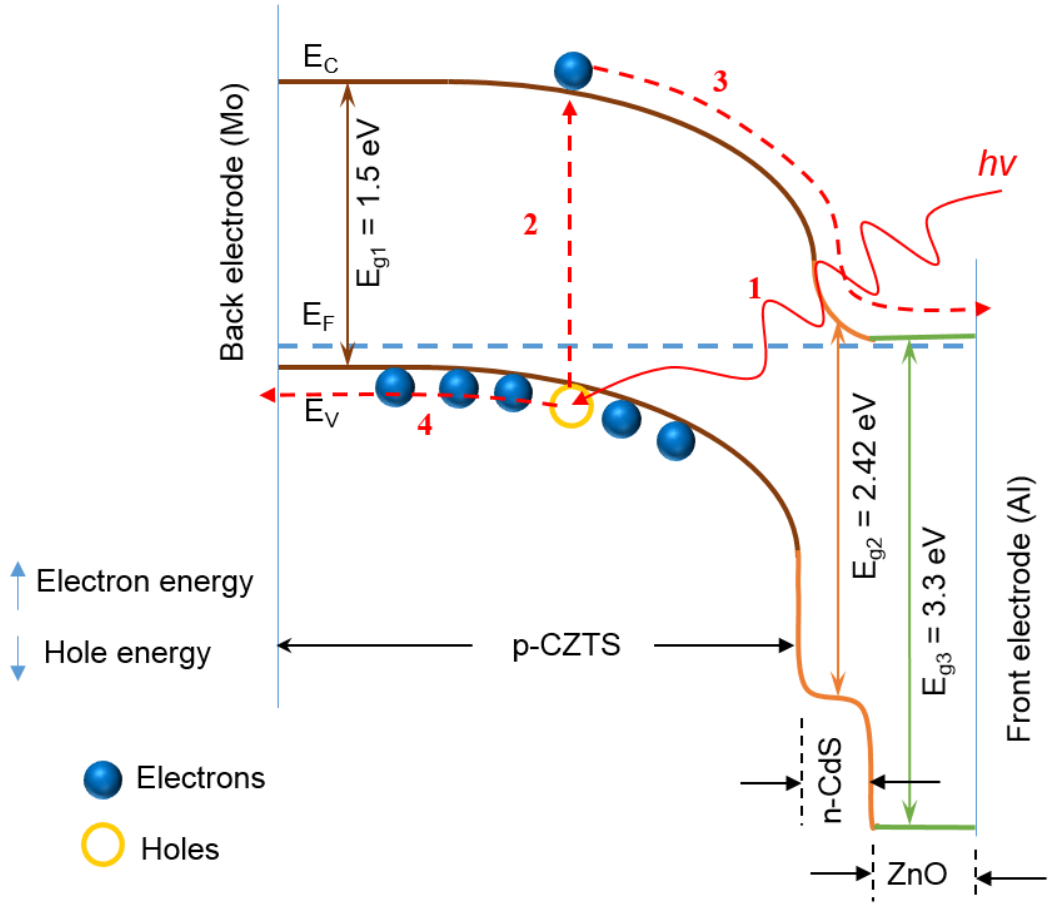

Figure 1.7. Energy band diagram of a CZTS-based heterojunction solar cell showing the band bending near the junction and schematic representation of photo-generation and separation of charge carriers.

In p-type CZTS, the Fermi level (E_F) is closer to the valence band and in n-CdS the Fermi level (E_F) is closer to the conduction band. During the formation of the heterojunction, charge transfer occurs across the junction until the Fermi levels align up and equilibrium is reached. This charge transfer leads to the formation of a space charge region (depletion region) near the junction causing a band bending as shown in Figure 1.7.

The working principle of the solar cell can be understood referring to the band diagram of Figure 1.7. Photo-generation of charge carriers and the current collection process is shown in four steps (1-4) marked in red. In step 1 and 2, the incident photon

interacts with the CZTS absorber layer and the photon energy is transferred to an electron lying in the valence band resulting in the creation of an electron-hole pair (the electron shifts to the conduction band from the valence band leaving a hole in the valence band). This process (step 1 and 2) is known as the photo-generation of charge carriers. The built-in electric field in the space charge region forces the electron and the hole to travel in the opposite directions and eventually reaching the front and back electrodes respectively. This process (step 3 and 4) is referred to as the charge carrier separation and current collection. The collected charges then flow through an external circuit to power an electrical load.

CHAPTER 2: CZTSSe THIN-FILM FABRICATION AND CHARACTERIZATION

2.1 OVERVIEW

This chapter is subdivided into two segments. In section 2.2, CZTSSe thin-film fabrication process is described in details. Structural, compositional, and morphological properties of the fabricated films were studied by Raman Spectroscopy, SEM/EDX, XPS, and AFM measurements and the results are presented in section 2.3. Characterization results are reported for the CZTSSe film corresponding to the best performing solar cell (η = 4.06%) achieved in this work. The microstructural and morphological studies were also performed on a high efficiency (η = 7.05%) CZTSe solar cell obtained from NREL and the results are incorporated in section 2.3.2 and 2.3.5 for a direct comparison to the 4.06% CZTSSe cell. Microstructures of these two cells showed significantly different features and their effect on the cell electrical parameters and photovoltaic performance are discussed in Chapter 3:.

Several fabrication routes have been investigated for the preparation of CZTSSe thin-films since the first working photovoltaic cell reported by Katagiri et al. in 1997 [69]. CZTSSe films and solar cells have been fabricated by vacuum based evaporation [15] [18] [69] [79] [80] [81] [82] [83] [84] [85] [86] [87] [88] and sputtering techniques [89] [90] [91] [92] [93] [94] [95] [96] [97], as well as non-vacuum approaches using nanoparticle inks [98] [19] [99] [100], hydrazine-based solution-particle slurry [101] [102] [103] [104], electrodeposition [105] [106] [107] [108], spray pyrolysis [109] [110] [111] [112], and

open atmosphere chemical vapor deposition (OACVD) methods [113]. Recently, an astounding photo-conversion efficiency of 12.6% has been reported for CZTSSe solar cell with the absorber layer prepared by a non-vacuum process using hydrazine-based hybrid solution-particle slurry [104]. However, use of highly toxic and hazardous hydrazine severely limits the scalability of this process for high volume commercial production. Other non-vacuum thin-film fabrication approaches promise cost reduction, however the reproducibility and film quality is compromised.

On the other hand, vacuum-based physical vapor deposition methods are well-established standards for growing high quality thin-films in the semiconductor industry. Particularly, evaporation has been proved to be a commercially scalable and cost effective method for growing superior quality CIGS and CdTe films in the past with unprecedented reproducibility achieving high efficiency solar cells. In this dissertation, a vacuum-based thermal evaporation technique was used for the fabrication of polycrystalline CZTSSe photo-absorber films.

2.2 CZTSSe THIN-FILM ABSORBER LAYER PREPARATION

The CZTSSe thin-film absorber layer was prepared by a two-step process. In the first step, high purity ZnS (99.99%), Cu (99.999%), and Sn (99.999%) were sequentially evaporated on molybdenum (Mo) coated soda-lime glass (SLG) substrates forming a ZnS/Cu/Sn stacked precursor layer on SLG/Mo. In the second step, substrates with the vacuum deposited precursor stacks were annealed under a mixed sulfur and selenium vapor at 550°C to react with the precursor forming the polycrystalline CZTSSe film. The two-step film fabrication process is illustrated in Figure 2.1.

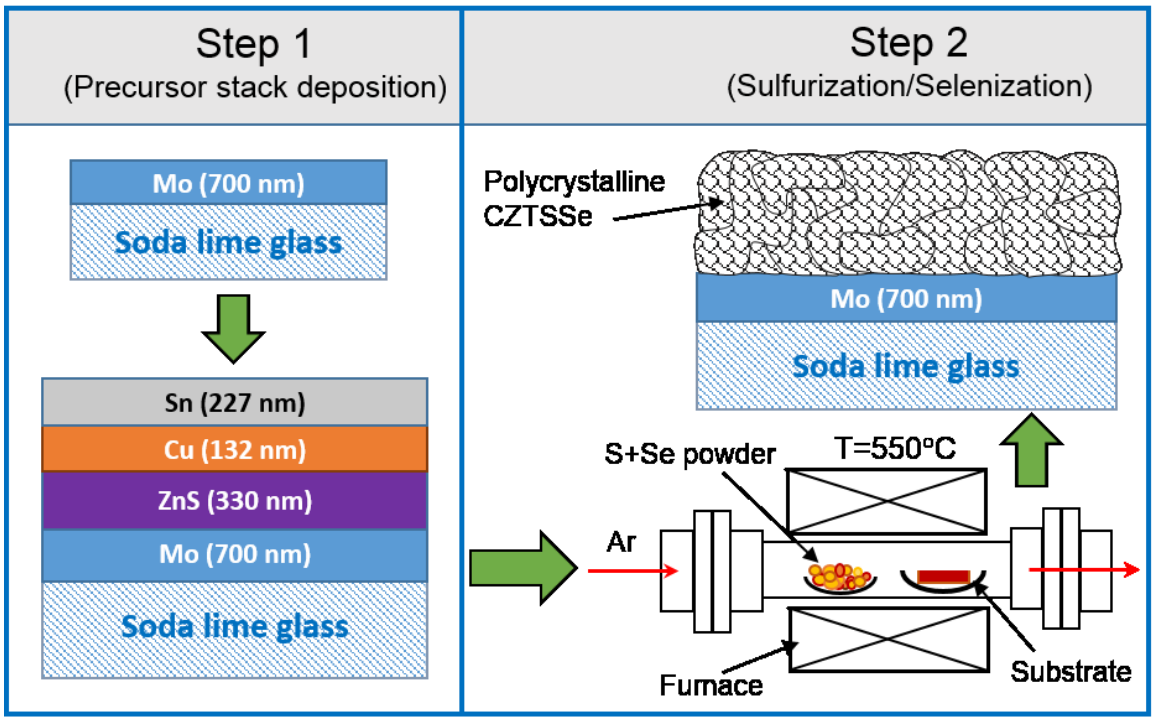

Figure 2.1. Schematic representation of the two-step CZTSSe thin-film fabrication process.

Bi-layer DC sputtered Mo-coated SLG substrates were used for the solar cell fabrication. Total thickness of the Mo film was approximately 700 nm. A vacuum thermal evaporator (CHA-SE600) shown in Figure 2.2 was used for the physical vapor deposition (PVD) of ZnS, Cu, and Sn precursors forming the ZnS/Cu/Sn stacked layer (Figure 2.1). The evaporation system is equipped with three individual sources that can be operated one at a time which allowed sequential deposition of all three layers of the precursor stacks in one vacuum cycle. A base vacuum of 2×10^{-6} torr was attained prior to the deposition evacuated by a diffusion pump. An Inficon XTC/2 thin-film deposition controller connected to a quartz crystal thickness monitor was programmed for automated deposition of all precursor layers. The tooling factor for each material deposition was precisely

calculated in order to accurately control the deposited film thickness within ±1% of the desired value.

Figure 2.2. CHA-SE600 thermal evaporation system used for the deposition of ZnS, Cu, and Sn to prepare the precursor stacks for CZTSSe films.

The sulfurization/selenization setup consisted of a horizontal quartz tube furnace (GSL-1100X, MTI Corporation) as shown in Figure 2.3. The chamber was evacuated by a mechanical pump and successively purged with argon to eliminate any residual oxygen in the system. 0.5 gm of high purity sulfur (99.999%) and 2.0 gm of zone refined (ZR) selenium (>7N) powders loaded in a quartz boat was used as the (S+Se) source. Dry UHP Ar flown at ~10 SCCM was used as the carrier gas. The reaction was carried out at 550°C

for one hour under atmospheric pressure following which the furnace was turned off and subsequently cooled down to room temperature.

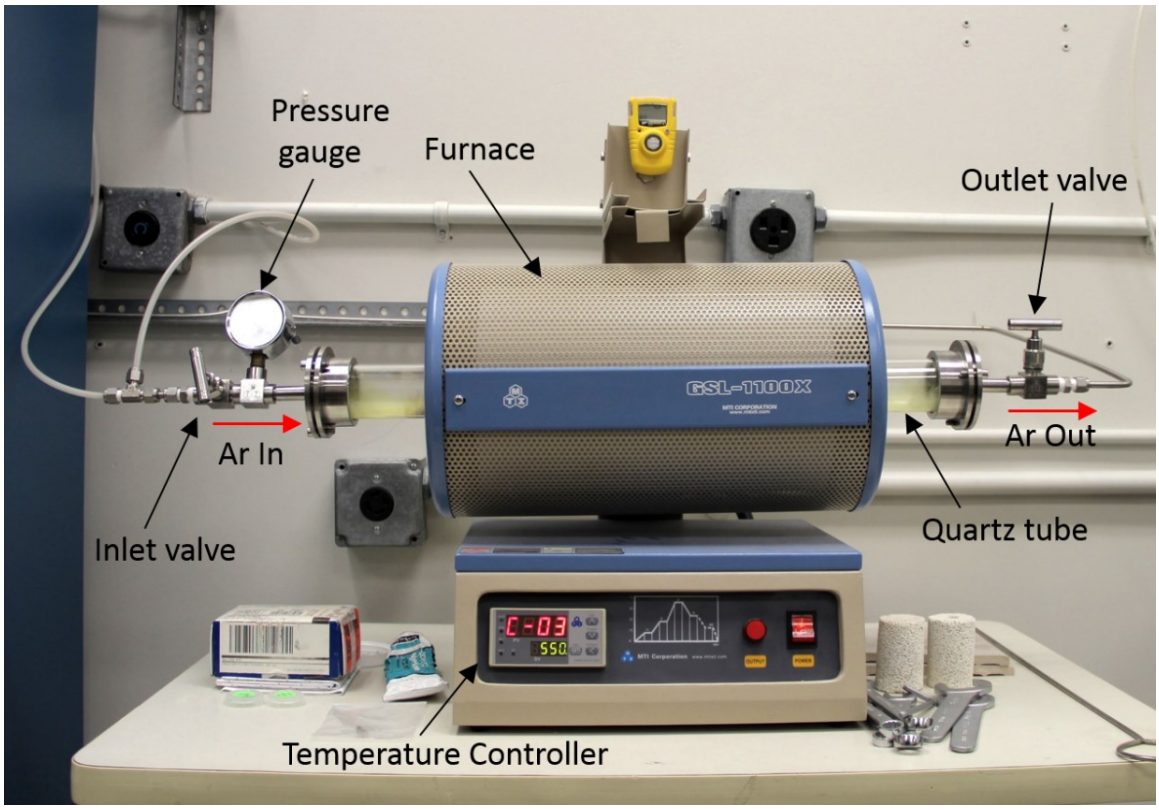

Figure 2.3. The sulfurization/selenization setup.

There are several challenges in fabricating CZTSSe absorber film that leads to an efficient solar cell. Performance of a CZTSSe cell is highly composition sensitive. As a general consensus, high efficiency solar cells could be obtained with a Cu-poor and slightly Zn-rich composition in the absorber, whereas stoichiometric films have been reported to show inferior photovoltaic performance. Also, during the high temperature sulfurization/selenization process, Sn loss from the precursor film as volatile $Sn(S,Se)_x$ have been reported [19] [114] [115]. Moreover, the processing parameters, such as temperature profile, peak reaction temperature, annealing duration etc. play a key role in

the final composition, microstructure, and resulting optoelectronic properties of the fabricated films. Therefore, obtaining a PV-grade absorber film requires optimization of several process parameters and is a challenging task.

Initial attempts of CZTSSe film preparation with stoichiometric precursors revealed approximately 20% Sn loss during the sulfurization/selenization process resulting in a highly Zn-rich and Cu-rich film. Results from these preliminary studies suggested that a highly Cu-poor precursor is necessary to obtain the desired final film composition with Cu/(Zn+Sn) ratio in the range of 0.8-0.9. Therefore, seven sets of highly Cu-poor precursor stacks with fixed Cu/(Zn+Sn) ratio of 0.7 and varying Zn/Sn ratios from 0.75-1.50 were fabricated. For simplicity, the ZnS thickness was kept constant at 300 nm and the thickness of Cu and Sn layers were varied to obtain the desired Zn/Sn ratio in the precursor. Thickness of ZnS, Cu, and Sn layers in all seven stacks and the corresponding elemental composition of the precursors are summarized in Table 2.1. The best solar cell was obtained from the precursor stack layer with 300 nm ZnS, 132 nm Cu, and 227 nm Sn (Stack ID: 3c in Table 2.1).

After annealing the substrates under (S+Se) vapor, the elemental atomic composition of the final CZTSSe films significantly changed from the parent precursor. Structural, compositional, and morphological properties of the CZTSSe films have been characterized by Raman spectroscopy, SEM/EDX, XPS, and AFM measurements and the results are presented in the next section.

Table 2.1. Summary of the precursor layer thickness and compositions for seven sets of precursor stacks.

Stack ID	Precursor stack layer thickness (nm)				Precursor elemental ratios		
	ZnS	Cu	Sn	Total thickness	$\frac{Cu}{(Zn+Sn)}$	$\frac{Zn}{Sn}$	$\frac{Chalcogen}{Metals}$
2c	300	146	273	719	0.7	0.75	0.252
3c	300	132	227	659	0.7	0.90	0.279
8a	300	126	205	631	0.7	1.00	0.293
3b	300	120	186	606	0.7	1.10	0.308
5b	300	116	172	588	0.7	1.20	0.319
2d	300	111	158	569	0.7	1.30	0.332
4d	300	105	136	541	0.7	1.50	0.353

2.3 CZTSSe FILM CHARACTERIZATION

2.3.1 Raman Spectroscopy

Raman spectroscopy is a powerful non-destructive characterization technique which can identify the chemical structure of a material under investigation and provides information specific to the chemical bond vibrations. Raman spectroscopy was performed on the grown CZTSSe absorber film to investigate the structure and phase purity of the films and is shown in Figure 2.4. The micro-Raman system used for the measurement was equipped with a 632 nm laser excitation with ~2 μm spot size. The setup was calibrated to known Si peak at 520.7 cm^{-1} prior to the measurement.

As shown in Figure 2.4, the major peak corresponding to 326.6 cm^{-1} is attributed to the A1 vibrational mode of the sulfur atoms present in the CZTSSe crystal lattice. The other broad peak at lower wavenumber region consists of two individual peaks – one at

211.5 cm^{-1} and the other at 218.1 cm^{-1}. The peak at 211.5 cm^{-1} is attributed to the A1 mode vibration originated from the Se atoms in CZTSSe and is in well agreement with the reported Raman shifts observed in CZTSSe bulk crystals and thin films [116] [117]. The other peak at 218.1 cm^{-1} corresponds to a SnS secondary phase which formed during sulfurization/selenization process [116]. Also, the small peak detected at 191.8 cm^{-1} can be attributed to the $SnS/SnSe_2$ phases. However, no other eminent peaks corresponding to secondary phases, such as β-ZnS/ZnSe (353 cm^{-1}/205 cm^{-1} and 251 cm^{-1}), $Cu_{2-x}S/Cu_{2-x}Se$ (475 cm^{-1}/260 cm^{-1}), and Cu_2SnS_3/Cu_2SnSe_3 (318 cm^{-1}/180 cm^{-1}) were observed. Two other relatively less intense Raman peaks related to CZTS/CZTSe were found at 176.4 cm^{-1} and 229 cm^{-1} as indexed in Figure 2.4. The peak positions observed here are further supported by the Raman spectra acquired on bulk single phase CZTSSe (S:Se = 1:1) crystals as presented in section 6.3.

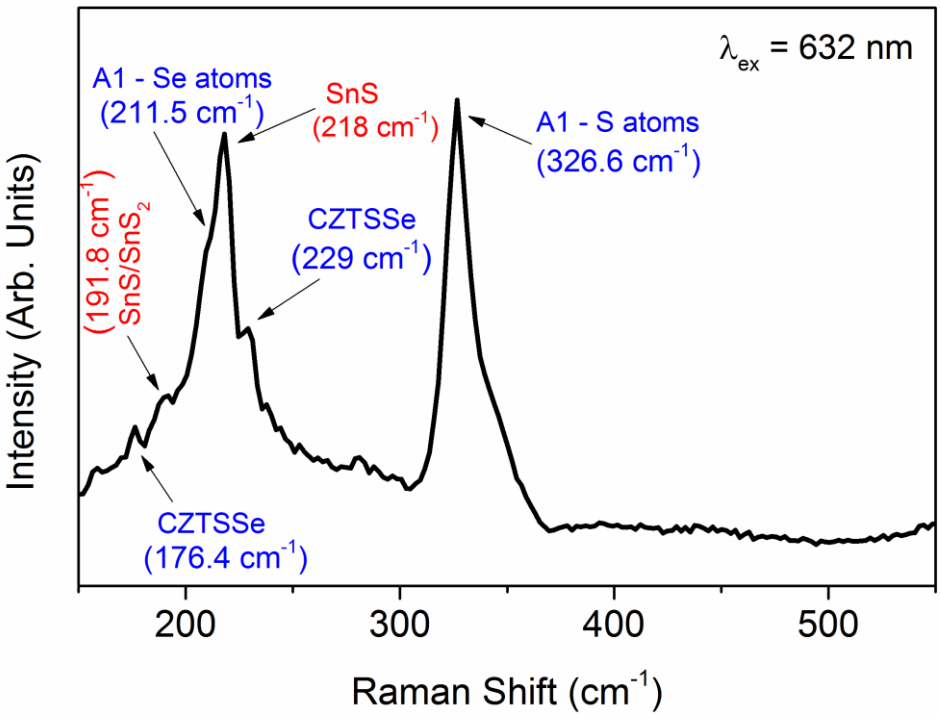

Figure 2.4. Raman spectra acquired on the fabricated CZTSSe absorber film.

2.3.2 Scanning Electron Microscopy (SEM)

The cross-sectional scanning electron microscopy (X-SEM) analysis was performed on the completed solar cells using a Zeiss Ultraplus thermal field emission scanning electron microscope (FESEM) equipped with EDX microanalysis. The X-SEM images of the CZTSSe cell and the NREL fabricated high efficiency CZTSe cell are shown in Figure 2.5.

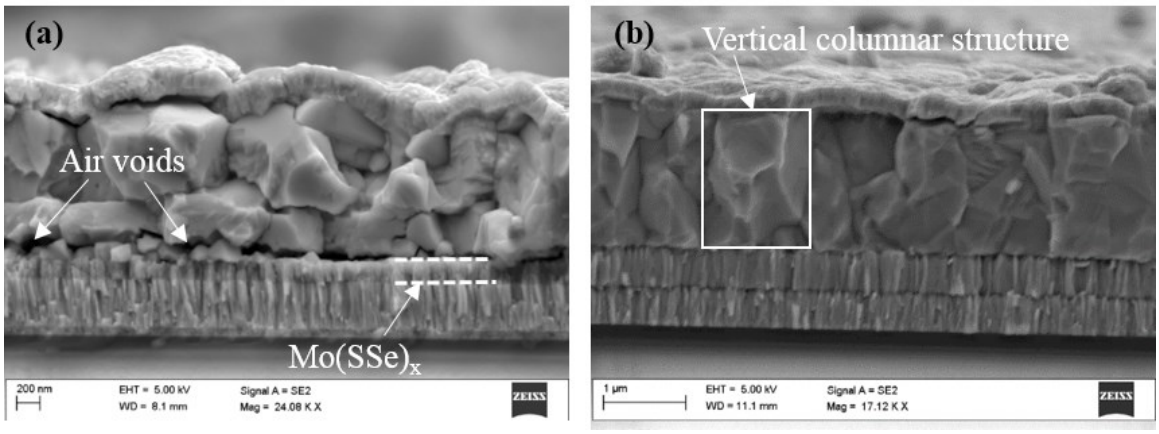

Figure 2.5. X-SEM images of (a) CZTSSe solar cell (η=4%), and (b) CZTSe solar cell (η=7%) respectively.

A number of notable features were observed from the SEM images. The CZTSSe cell showed small multiple grains in the z-direction with different grain sizes ranging from ~0.3-0.8 µm. Such smaller multigrain structure presents grain boundaries in the transverse direction to the transport path of the photo-generated carriers across the cell which act as recombination center and hinders carrier transport. These phenomena are well known for limiting the photo-generated current and reduce fill factor in polycrystalline thin-film solar cells. The second notable observation was the presence of micro air-voids at the back contact. This reduces the effective contact area leading to an increased series resistance. We believed that further optimization the film growth parameters will lead to the

elimination of these undesired air-voids. Unlike the low efficiency CZTSSe cell, the CZTSe absorber layer of the high-efficiency (η=7.05%) cell showed closely packed vertical columnar grain structure without any air voids. Also, a thin interfacial $Mo(SSe)_x$ layer was observed at the Mo back contact in the CZTSSe cell, but the high efficiency CZTSe cell was free from any such interfacial layer.

2.3.3 Energy Dispersive X-ray Spectroscopy (EDX)

The EDX analysis was performed on the CZTSSe absorber layer (corresponding to precursor stack 3c in Table 2.1) to measure the elemental composition and the calculated elemental ratios are tabulated in Table 2.2. It is observed that the final film became Zn-rich although the parent precursor had a Sn-rich composition (see Table 2.1). This happened due to Sn-loss in the form of volatile Sn(S,Se) during the annealing process.

The EDX line scan on the device cross-section is presented in Figure 2.6. The formation of a Mo(SSe)x interfacial layer at the back contact can be observed in the Se scan line.

Table 2.2. Elemental ratios in the CZTSSe photo-absorber films.

Composition of CZTSSe film: Cell 4					Elemental ratios			
Cu (at%)	Zn (at%)	Sn (at%)	S (at%)	Se (at%)	$\frac{Cu}{(Zn+Sn)}$	$\frac{Zn}{Sn}$	$\frac{S}{(S+Se)}$	$\frac{Chalcogen}{Metals}$
15.49	10.64	9.41	37.56	26.91	0.773	1.13	0.583	1.815

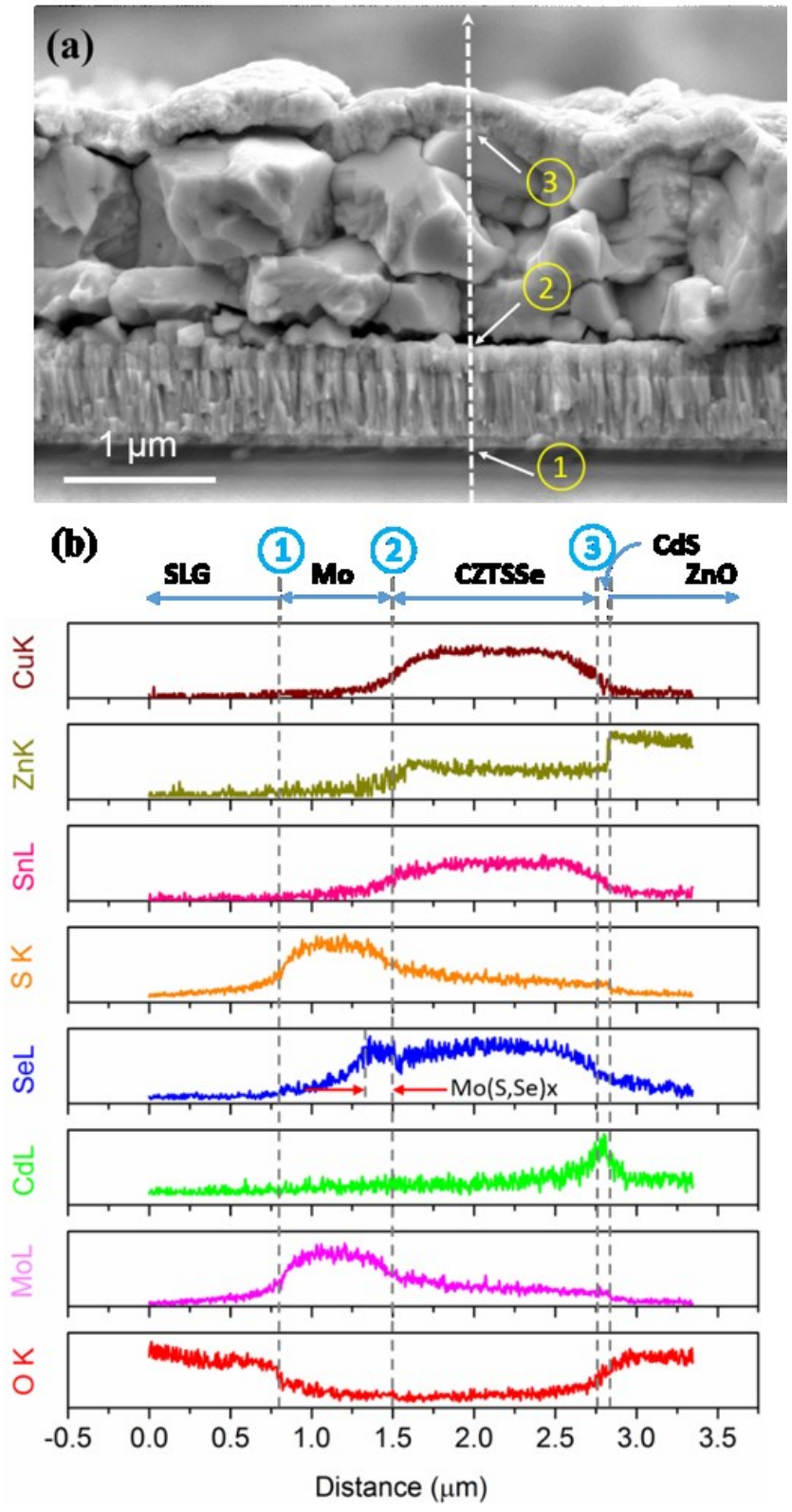

Figure 2.6. The EDX line scans of different elements in the CZTSSe solar cell.

2.3.4 X-ray Photoelectron Spectroscopy (XPS)

X-ray photoelectron spectroscopy (XPS) measurements were carried out on the $Cu_2ZnSn(S_xSe_{1-x})_4$ absorber film to identify the electronic states of the constituent elements. XPS is a surface characterization technique which can identify elemental composition, chemical states, bonding information, and predicts types of compounds present in a material.

In this experiment, a photon of known energy, $h\nu$, bombards the surface of a material and is absorbed by the material (Figure 2.7) resulting in ionization and emission of an inner shell electron into the vacuum according to the following equation:

$$E_k = h\nu - E_b \qquad 2.1$$

Where, E_k is the kinetic energy of the emitted photoelectron, $h\nu$ is the photon energy, and E_b is the binding energy of the electron. All elements exhibit characteristic binding energies, E_b, associated with its atomic orbit. This means that each element and molecule will give rise to specific peaks in the XPS spectrum at the kinetic energies E_k, depending on the photon energies and binding energies. Most modern XPS systems use monochromatic X-ray sources, which emit photons with a fixed energy. When subtracted from the kinetic energy, the binding energy of the detected photoelectrons are known, and the element and electron core level related to these counted photoelectrons can be determined.

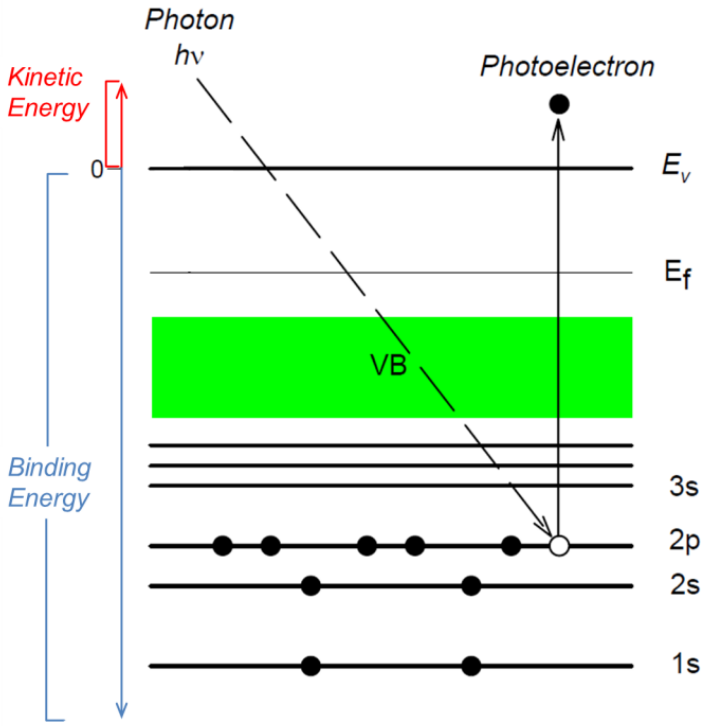

Figure 2.7. Schematic diagram of binding energy and kinetic energy of a displaced electron due to x-ray interaction with a material.

XPS measurements were conducted with a Kratos AXIS Ultra DLD XPS system equipped with a hemispherical energy analyzer and a monochromatic Al Kα source with energy 1486.6 eV. The Al Kα source was operated at 15 keV and 150 W incident on surface at 45° with respect to the surface normal. The pass energy was kept fixed at 40 eV for the detail scans. The sample chamber was kept under ultra-high vacuum of 2×10^{-9} torr and a high performance charge neutralizer was used to compensate for the sample surface charge. The binding energy of the analyzer was calibrated with an Ag foil to the value of 368.21 ± 0.025 eV. The spot size for analysis was approximately 0.3×0.7 mm^2. During XPS scanning, the reproducibility of spectra were assured by multiple scanning cycles to reach accuracy better than ±0.05 eV.

XPS survey spectrum of the CZTSSe film is shown in Figure 2.8. Strong photoelectron lines from Cu, Zn, Sn, Se, and S core levels along with a trace amount of carbon (C) and oxygen (O) lines are detected. The photoelectron peaks of interest and the pronounced auger peaks are identified and indexed in the figure. No foreign impurities were observed from the survey spectrum.

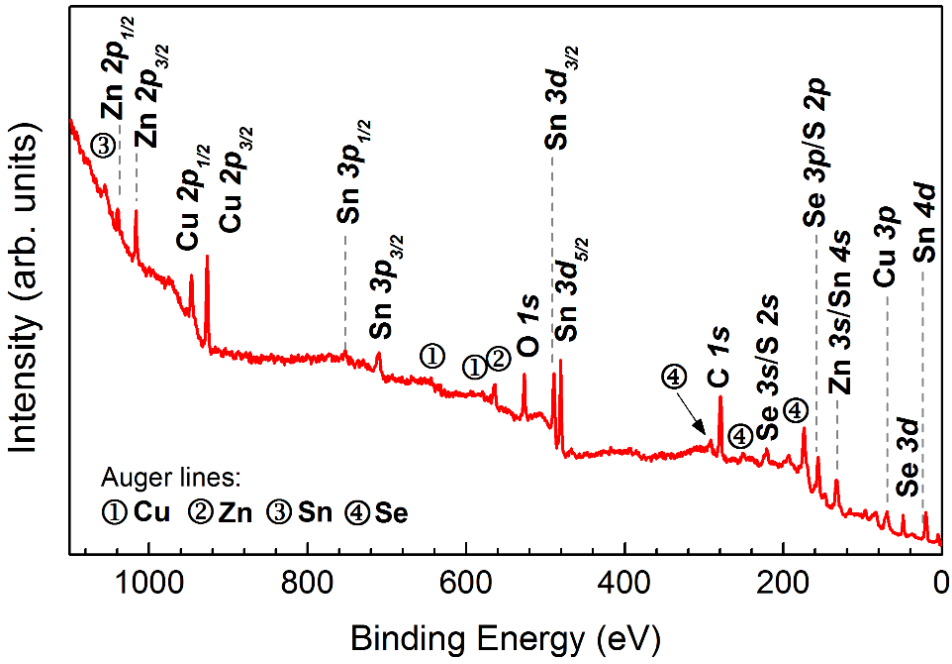

Figure 2.8. XPS survey spectrum of CZTSSe absorber film.

High resolution spectra of Cu 2p, Zn 2p, Sn 3d, Se 3d, and S 2p core levels were acquired to determine the electronic states of the elements. Since the XPS observations for all three crystals were similar, only the results of CZTSSe crystal is discussed in this section. The high resolution XPS spectra for CZTSSe crystal are shown in Figure 2.9. Cu 2p, Zn 2p, and Sn 3d core levels were found to be split into two spin orbitals— $2p_{1/2}$, $2p_{3/2}$, and $3d_{1/2}$, $3d_{3/2}$, respectively. S 2p and Se 3p peaks were merged together and Se $3d_{3/2}$ and $3d_5/2$ spin orbitals were overlapped. The superimposed peaks were de-convoluted using

XPS peak fitting program to locate precise peak positions. A Shirley background subtraction was applied for all Gaussian peak fittings.

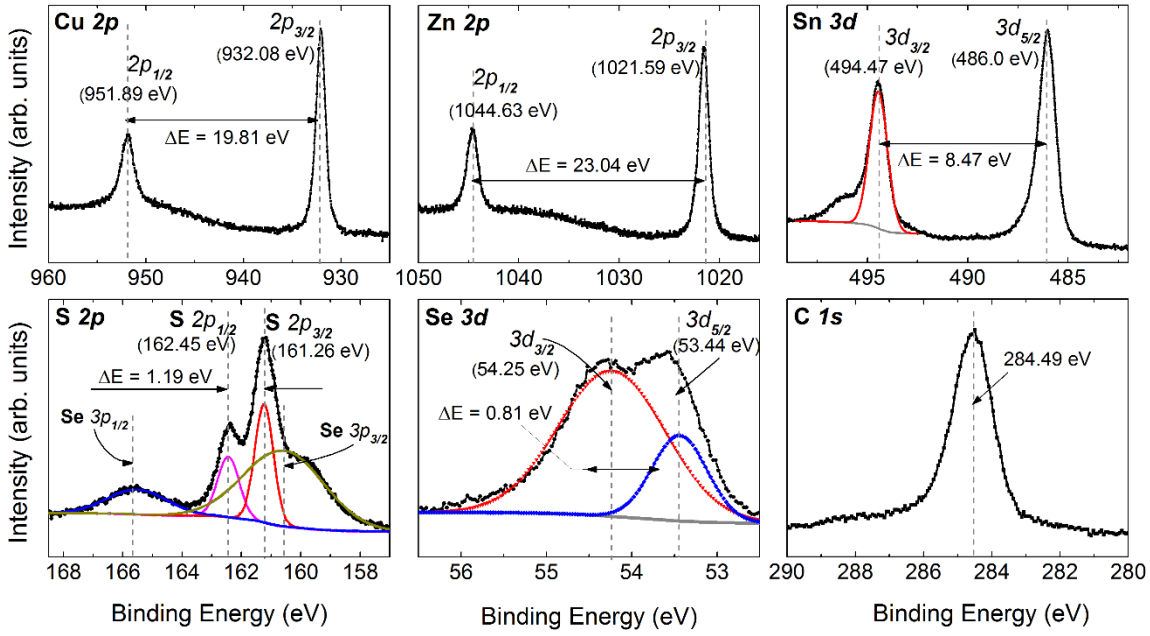

Figure 2.9. XPS survey spectrum of CZTSSe absorber film.

The two spin orbits of Cu 2p core levels were split into a doublet separated by ΔE=19.81 eV ($2p_{1/2}$ at 951.89 eV and $2p_{3/2}$ at 932.08 eV), which is indicative of Cu (I). The Zn 2p core level orbitals at 1044.63 eV and 1021.59 eV corresponding to $2p_{1/2}$ and $2p_{3/2}$ with a peak separation of ΔE=23.04 eV suggests the presence of Zn (II) state. Sn 3d spin orbitals, ($3d_{3/2}$ located at 494.47 eV and $3d_{5/2}$ located at 486.0 eV) can be attributed to the existence of Sn (IV) electronic state. The S 2p doublet separated by an energy gap of 1.19 eV ($2p_{1/2}$ at 162.45 eV and $2p_{3/2}$ at 161.26 eV) and Se 3d doublet separation of 0.81 eV ($3d_{3/2}$ at 54.25 eV and $3d_{5/2}$ at 53.44 eV) can be assigned to the formation of metal sulfo-selenides, which are consistent with the standard reference values. The peak positions,

FWHM, and energy separation between the split orbitals (ΔE) for all elements are summarized in Table 2.3.

Table 2.3. Summary of XPS core level peak parameters of CZTSSe film.

Core level	Binding energy (eV)	FWHM	Peak separation, ΔE (eV)
Cu $2p_{1/2}$	951.89	1.67	19.81
Cu $2p_{3/2}$	932.08	1.23	
Zn $2p_{1/2}$	1044.63	1.41	23.04
Zn $2p_{3/2}$	1021.59	1.30	
Sn $3d_{3/2}$	494.47	1.07	8.47
Sn $3d_{5/2}$	486.00	1.13	
Se $3d_{3/2}$	54.25	1.47	0.81
Se $3d_{5/2}$	53.44	0.76	
S $2p_{1/2}$	162.45	0.83	1.19
S $2p_{3/2}$	161.26	0.74	
C 1s	284.49	1.39	-
O 1s	532.04	1.55	-

2.3.5 Atomic Force Microscopy (AFM)

Surface morphology and the roughness of the CZTSSe and CZTSe films were studied by atomic force microscopy (AFM). A Picoplus AFM was operated in tapping mode and a Si tip with a nominal frequency of 61 KHz was used for the scanning. The scan area was 10 μm × 10 μm with a resolution of 256 lines per scan.

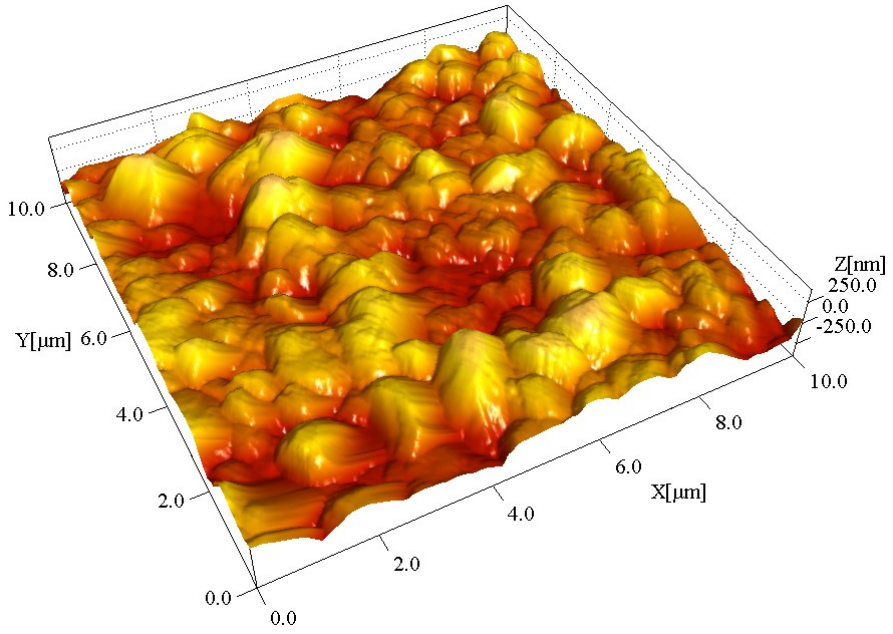

Figure 2.10. Three-dimensional AFM image showing the surface morphology of the CZTSSe absorber layer.

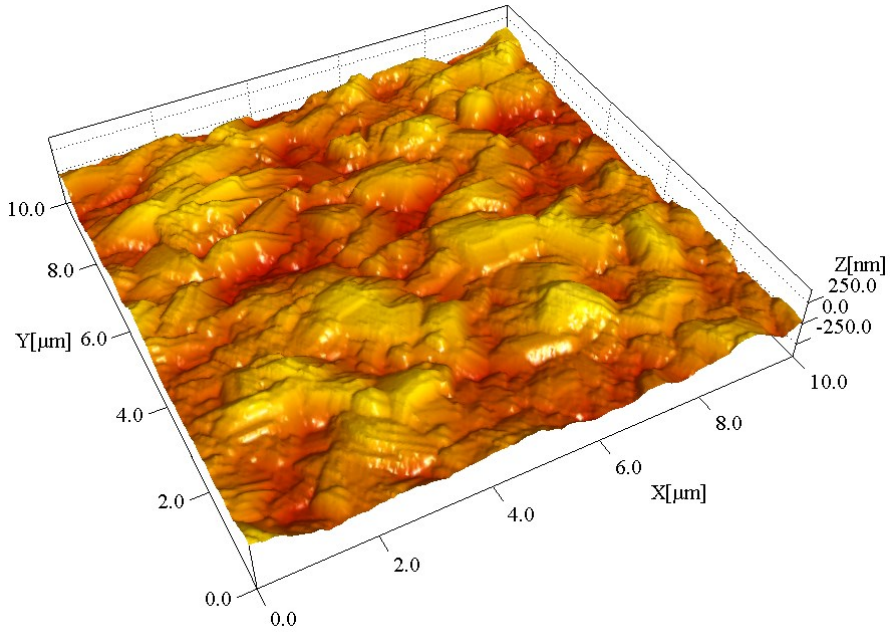

Figure 2.11. Three-dimensional AFM image showing the surface morphology of NREL fabricated CZTSe absorber layer.

The tip details and the AFM setup photograph are included in APPENDIX B –. The three-dimensional surface scans of the CZTSSe and CZTSe cells are plotted in Figure 2.10 and Figure 2.11 respectively. The CZTSSe film surface was found to be much rougher than the CZTSe absorber film prepared by vacuum co-evaporation at NREL. In Figure 2.12, the two dimensional images are shown with surface line scans.

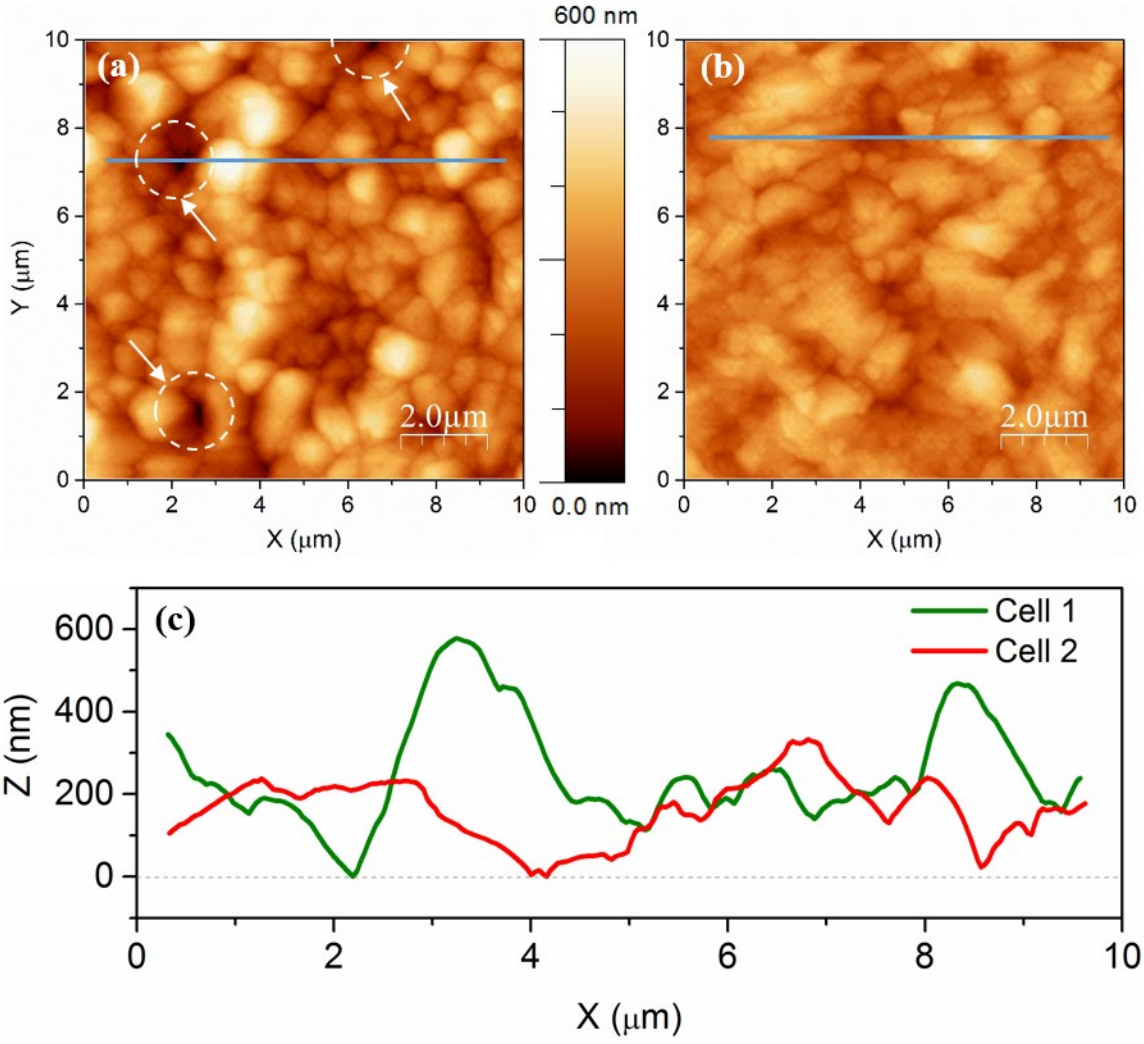

Figure 2.12. Two-dimensional AFM images of the (a) CZTSSe and (b) CZTSe films respectively, and (c) line scan roughness profile of the two absorber films.

The average and rms roughness values were calculated using the following formula:

$$R_{avg} = \frac{1}{N}\int_0^L |Z(x)|\,dx \approx \frac{1}{N}\sum_{n=1}^{N}|Z_n - \bar{Z}| \qquad 2.2$$

$$R_{rms} = \sqrt{\frac{1}{N}\int_0^L |Z^2(x)|\,dx} \approx \sqrt{\frac{1}{N}\sum_{n=1}^{N}(Z_n - \bar{Z})^2} \qquad 2.3$$

Where N is the total number of points within the analysis area, L is the evaluation length over which the analysis is performed, $Z(x)$ is the function defining the measured surface profile, $\bar{Z}$ is the mean surface height relative to the center plane within the analysis area, Z_n is the height of point n in the z-direction. The rms and average roughness of the CZTSSe film was calculated to be 88.4 nm and 70.8 nm respectively. The CZTSe film had a smoother morphology with rms and average roughness values of 57.5 nm and 46.7 nm respectively. A notable feature in the low efficiency CZTSSe cell is the presence of micro-pores on the film surface as encircled and marked by arrows in Figure 2.12. These pores act as low-resistance shunt paths contributing to the low shunt resistance as discussed in section 3.3.1.

CHAPTER 3: SOLAR CELL FABRICATION AND CHARACTERIZATION

3.1 OVERVIEW

This chapter provides details of CZTSSe-based heterojunction solar cell fabrication process and electrical characterization results of the cells including current-voltage (I-V) characteristics under illumination and under dark conditions, illumination dependent performance, and capacitance-voltage (C-V) measurements. Photovoltaic performance of the fabricated solar cells were studied and the diode parameters were extracted. The complete solar cells were fabricated on the as-prepared CZTSSe absorber films as discussed in Chapter 2:.

3.2 DEVICE STRUCTURE AND SOLAR CELL FABRICATION

The well-studied CIGS thin film solar cell structure is usually inherited for CZTS-based devices. The schematic structure of a typical CZTSSe solar cell is shown in Figure 3.1 along with the corresponding cross-sectional SEM image of the fabricated CZTSSe device. Sputtered bi-layer molybdenum (Mo) film with a thickness of ~0.7 μm deposited on soda-lime glass (SLG) substrate was used as the standard back contact. The p-type CZTSSe absorber layer thickness was measured to be ~1.2-1.4 μm. A thin (~50 nm) n-type CdS window layer was deposited on the p-CZTSSe film by a low-cost chemical bath deposition technique forming the heterojunction. Subsequently, the device structure was completed by deposition of ~50 nm thick high resistive intrinsic ZnO (i-ZnO) buffer layer followed by the deposition of ~200 nm thick Al doped ZnO (Al:ZnO) layer by RF

magnetron sputtering. Finally, front Al grid lines were evaporated on top of the ZnO transparent conducting oxide (TCO) for improved current collection. The finished solar cells had a configuration of SLG/Mo/CZTSSe/CdS/i-ZnO/Al:ZnO/Al. No anti-reflection coatings were used for the solar cells studied in this dissertation.

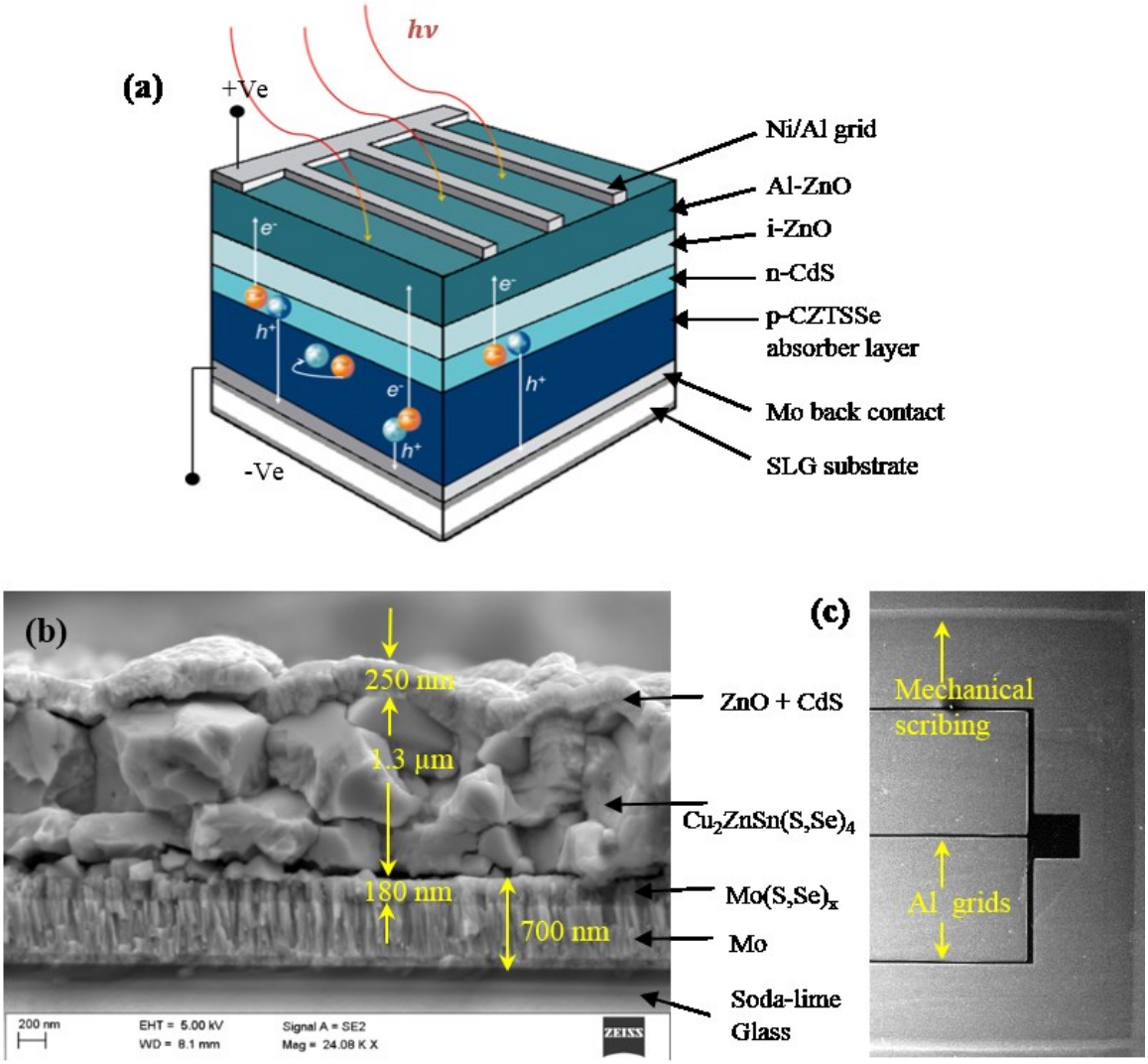

Figure 3.1. (a) Three dimensional schematic of the device structure, (b) cross-sectional SEM images of the CZTSSe solar cell (η=4.06%), and (c) SEM image taken from top of the solar cell.

The best performing solar cell array (prepared with the precursor stack ID: 3c in Table 2.1) with seven individual cells is shown in Figure 3.2. The Cell # 4 of this array exhibited the best photovoltaic performance corresponding to an efficiency of 4.06%.

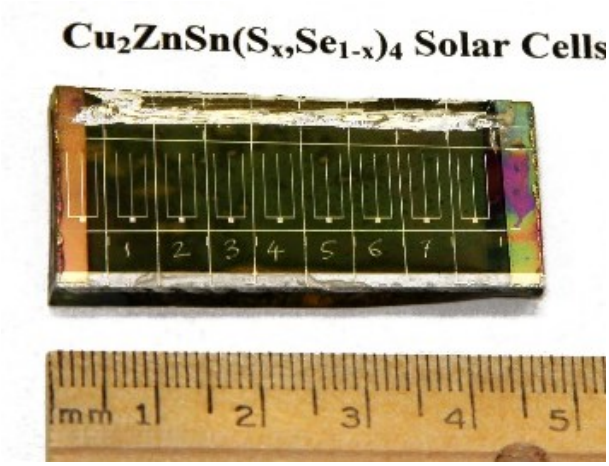

Figure 3.2. Photograph of the CZTSSe solar cell array prepared at the University of South Carolina (USC).

3.3 SOLAR CELL CHARACTERIZATION

3.3.1 Current-Voltage (I-V) Measurements:

The current-voltage (I-V) characteristics of the fabricated solar cells were measured under illumination and under dark conditions. The dark and illuminated J-V plots for the CZTSSe cell are shown in in Figure 3.3. The photovoltaic performance of a solar cell is generally characterized by the following four important parameters: the open-circuit voltage (V_{OC}), short-circuit current (I_{SC}), fill factor (FF), and the photo-conversion efficiency (η). V_{OC} is the maximum voltage that a cell exhibits under open-circuit condition, i.e. with an infinite load resistance connected across the cell. I_{SC} is the maximum current that a cell produces while short-circuited, i.e. with a zero load resistor connected to the cell. In both open-circuit and short-circuit conditions the output power is zero. The maximum power that a cell can deliver to a practical load is found somewhere in between

and the corresponding voltage and the current is denoted by V_{mp} and I_{mp} respectively. The maximum power output (P_{max}) of a cell is given by the following relation.

$$P_{max} = V_{mp} \times I_{mp} \quad 3.1$$

The fill factor is a measure of the fraction of the theoretical maximum power to the actual maximum power deliverable by the cell. The theoretical maximum power is defined by $V_{OC} \times I_{SC}$ and the actual maximum power P_{max} is given by equation 3.1. The fill factor of the cell is then defined by equation 3.2.

$$FF = \frac{V_{mp} \times I_{mp}}{V_{OC} \times I_{SC}} \quad 3.2$$

The photoconversion efficiency (η) of the cell is defined as the fraction of the incident light energy (P_{in}) converted into electrical energy for use and is given by equation 3.3.

$$\eta = \frac{P_{max}}{P_{in}} = \frac{P_{max}}{A \times P_{Opt}} \quad 3.3$$

In equation.3.3, P_{opt} is the incident optical power density and A is the total cell area. For the fabricated CZTSSe cells, the total cell area was measured to be ~0.42 cm^2 and the optical power density was 100 mW/cm^2 for simulated AM1.5G illumination.

The I-V measurements were performed using a Keithley 237 source measure unit (SMU) and the data acquision and analysis was performed by custom made LabVIEW programs. The best performing CZTSSe cell exhibited an open-circuit voltage (V_{OC}) of 506 mV, a short-circuit current density (J_{SC}) of 22.92 mA/cm^2 and a FF of 35% resulting in an efficiency of η = 4.06% under AM1.5G illumination measured at 297K. The maximum power output (P_{max}) at this illumination level was 1.694 mW corresponding to a voltage (V_{mp}) of 294 mV and a current (I_{mp}) of 5.763 mA.

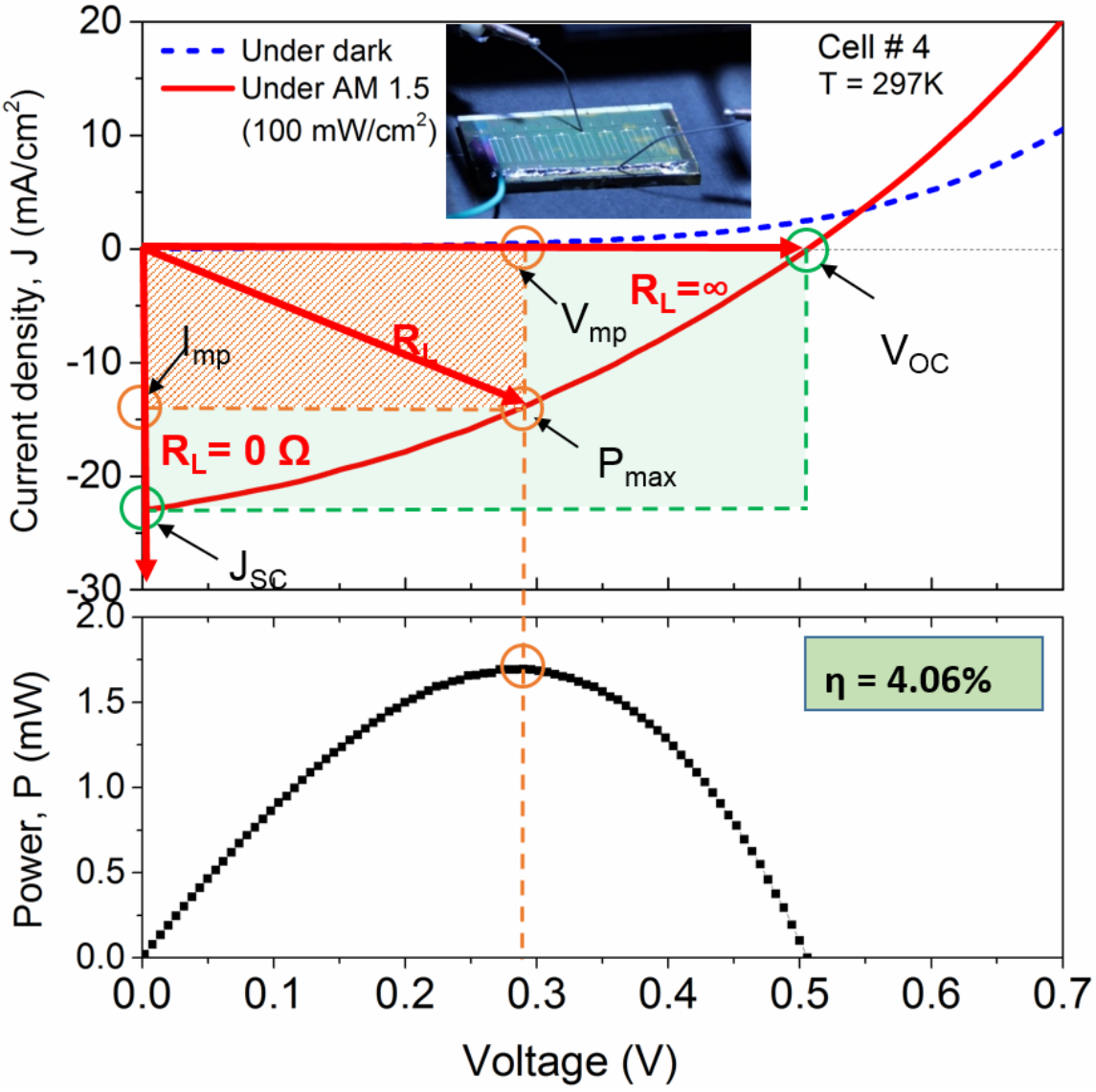

Figure 3.3. Dark and illuminated I-V characteristics of the best performing CZTSSe cell # 4 (top) and corresponding power curve of the cell (bottom).

The dark J-V characteristics of the solar cell can be modelled by a standard two-diode equation as below:

$$J = J_{01}\left[exp\left(\frac{V - JR_S}{n_1 kT}\right) - 1\right] + J_{02}\left[exp\left(\frac{V - JR_S}{n_2 kT}\right) - 1\right] + \frac{V - JR_S}{R_{Sh}} \qquad 3.4$$

where, J_{01}, J_{02} are the reverse saturation current densities and n_1, n_2 are the ideality factors of diode 1 and diode 2 respectively. V is the applied voltage, T is temperature in kelvin and k is the Boltzmann constant. The experimental dark J-V data was fitted following equation 3.4 as shown in Figure 3.4. A value of $J_{01} = 1.8\times10^{-5}$ A/cm^2, $n_1 = 3.9$ and $J_{02} = 5.1\times10^{-9}$ A/cm^2, $n_2 = 2.15$ were extracted from the fitting results. The series and shunt resistances were estimated to be ~31 Ω and 125 Ω respectively. Cell performance is found to be limited by the high series resistance, low shunt resistance accompanied with a poor fill factor. The cell microstructure is attributed to the origin of such high R_S and low R_{Sh} as discussed in section 2.3.2 and 2.3.5 respectively.

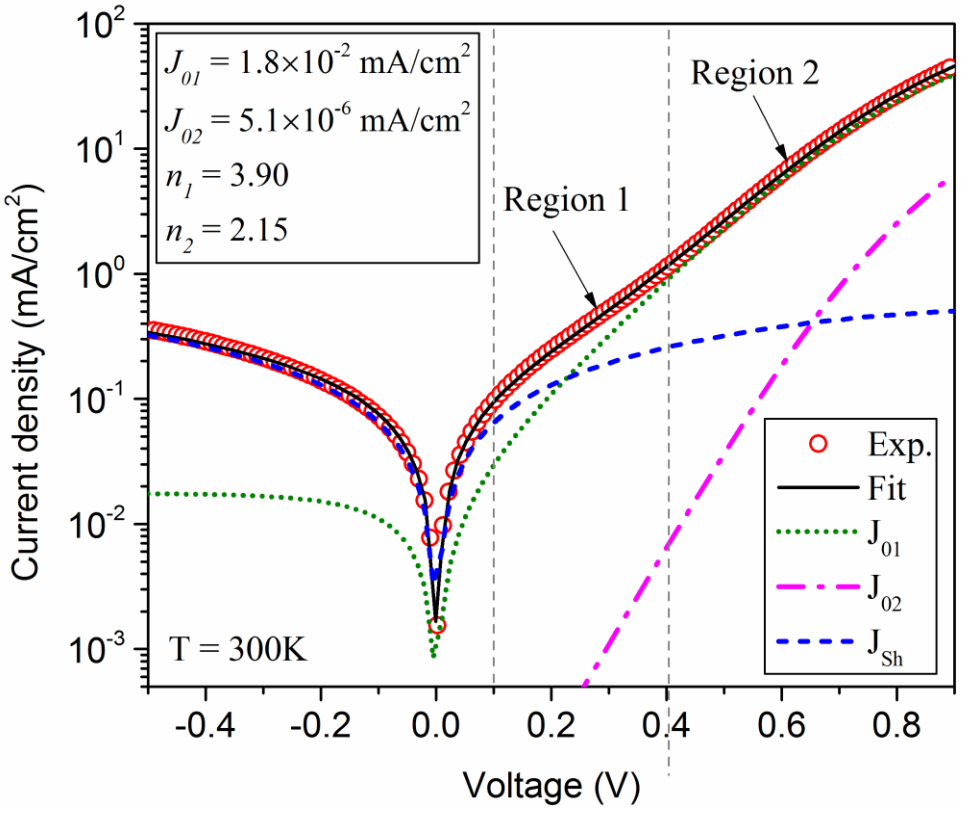

Figure 3.4. Fitting of the dark J-V data using the two-diode model of equation 3.4.

Recombination of the charge carriers is often a major contributor hindering the cell performance in polycrystalline thin-film solar cells. The V_{OC} of a cell dominated by a recombination process is given by equation 3.5.

$$V_{OC} = \frac{E_A}{q} - \frac{nKT}{q} \ln\left(\frac{J_0}{J_{Ph}}\right) \qquad 3.5$$

Where E_A is the activation energy of the recombination center. Thus, a temperature dependent V_{OC} measurement was performed to evaluate the recombination process in the cells and are shown in Figure 3.5. From the Y-axis intercept of the straight line fitting at higher temperature region, the activation energy associated with the recombination process can be extracted. It is seen that both cells show a lower activation energy of recombination compared to their bandgaps. This suggests that the dominant recombination process in these cells are occurring at the p-CZTSSe/n-CdS heterojunction interface most likely due to the presence of detrimental interfacial states.

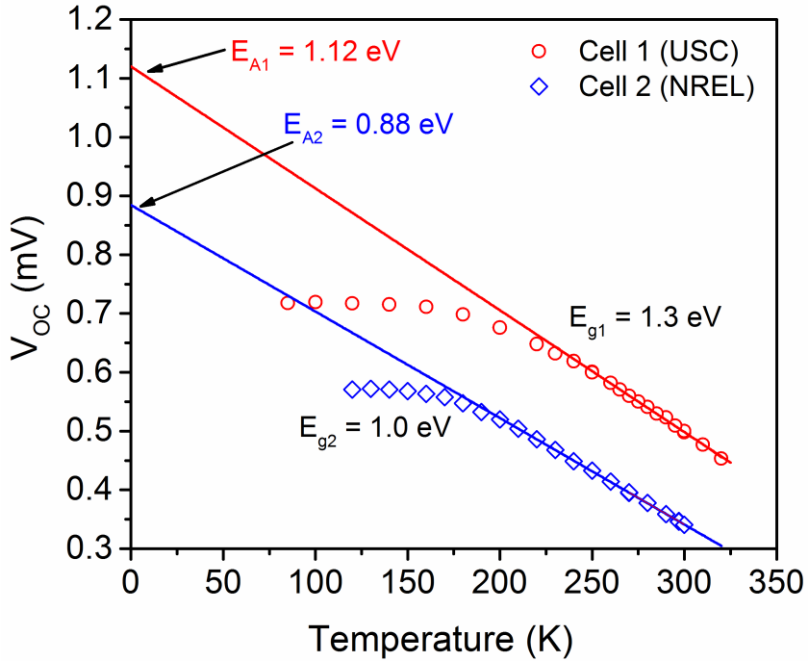

Figure 3.5. V_{OC} as a function of temperature for CZTSSe (Cell 1) and CZTSe (Cell2).

3.3.2 Illumination Dependent Performance:

The low-light performance of the cells were further investigated by I-V measurements under various illumination levels from 10 mW/cm^2 to 100 mW/cm^2. Neutral density filters were used to attenuate the incident light from the solar simulator. The open-circuit voltage (V_{OC}) of a solar cell has a logarithmic dependence on the incident light intensity and is given by equation 3.6.

$$V'_{OC} = \frac{nKT}{q} ln\left(X\frac{I_{SC}}{I_0}\right) = \frac{nKT}{q}\left[ln\left(\frac{I_{SC}}{I_0}\right) + ln(X)\right] = V_{OC} + \frac{nKT}{q} ln(X) \qquad 3.6$$

In Eq. 3.4, n is the ideality factor of the diode, K is the Boltzmann's constant, T is the temperature in K, q is the electronic charge, I_0 is the incident light intensity and X is the illumination factor. The short-circuit current of a cell is linearly dependent on the incident light intensity and is given by equation 3.7.

$$I'_{SC} = XI_{SC} \qquad 3.7$$

The I-V curves at different illumination intensities are shown in Figure 3.6. It is observed that the effective efficiency increases as the light intensity is decreased and reaches to 6.38% under 10 mW/cm^2 illumination. The dependence of the V_{OC} and I_{SC} as a function of illumination intensity are shown in Figure 3.7. A perfect logarithmic dependence of V_{OC} and linear dependence of I_{SC} on the incident light intensity was observed.

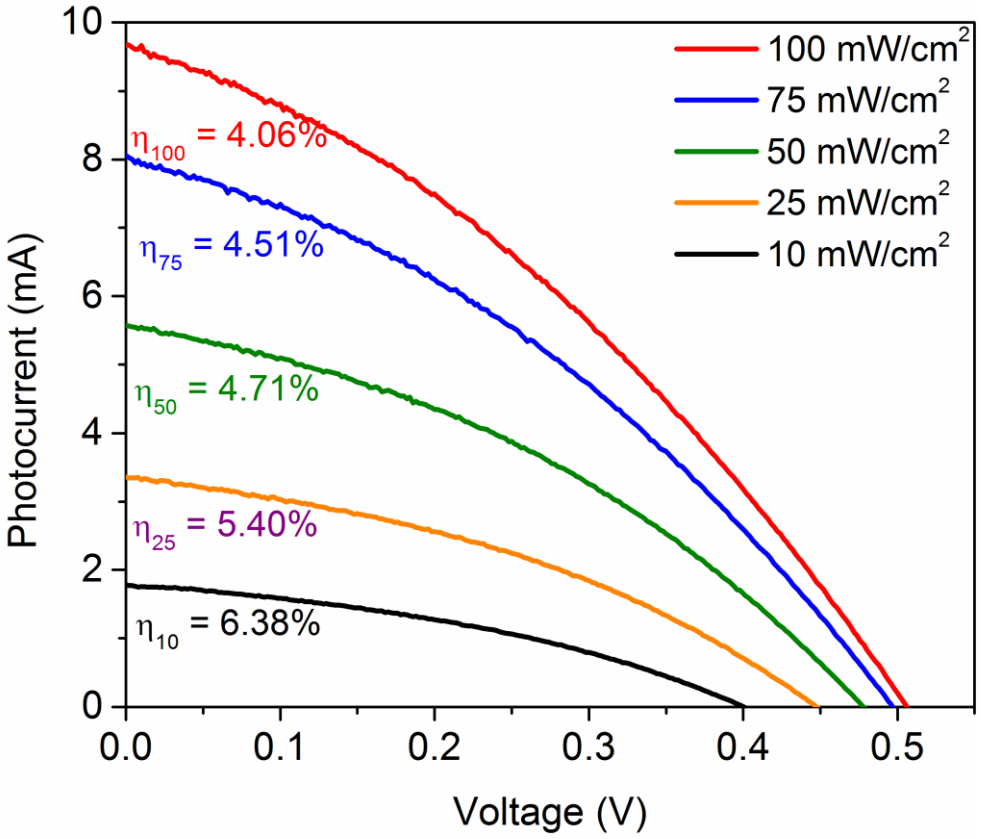

Figure 3.6. (a) I-V characteristics of CZTSSe cell # 4 under varying illumination levels and dependence of (b) V_{OC} and (c) I_{SC} with incident light intensity

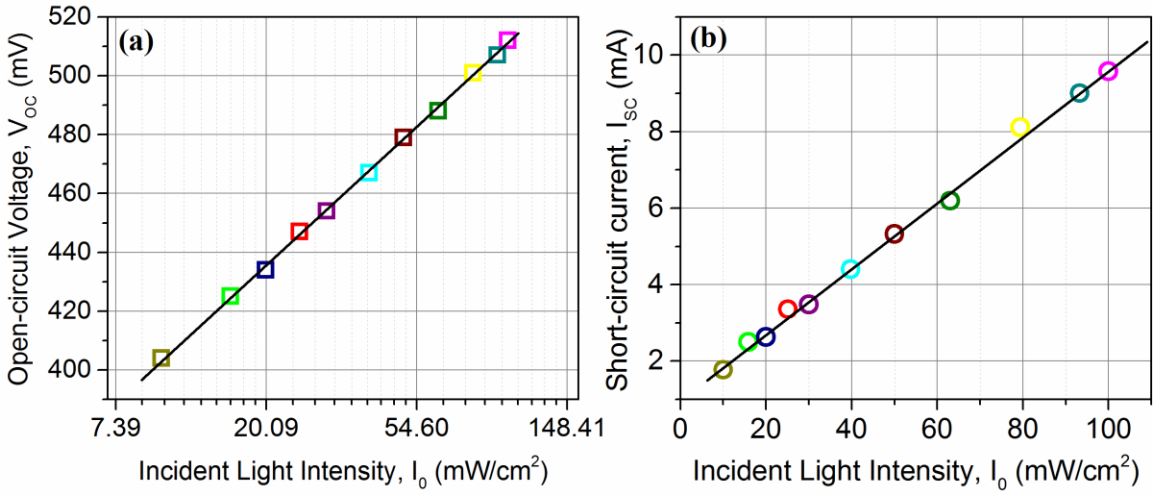

Figure 3.7. (a) I-V characteristics of CZTSSe cell # 4 under varying illumination levels and dependence of (b) V_{OC} and (c) I_{SC} with incident light intensity.

Table 3.1. Summary of cell performance parameters at different illumination intensities.

Light Intensity (mW/cm^2)	V_{OC} (mV)	I_{SC} (mA)	FF (%)	V_m (mV)	I_m (mA)	η (%)
100	506	9.63	34.8	294	5.76	4.06
75	498	8.06	35.4	284	5.00	4.51
50	478	5.57	37.1	284	3.48	4.71
25	447	3.36	37.8	268	2.12	5.40
10	400	1.78	37.6	238	1.13	6.38

3.3.3 Capacitance-Voltage (C-V) Measurements

Capacitance voltage (C-V) measurements provide useful information on the carrier concentration and barrier height of the device. C-V measurements were carried out using a Solartron 1470E multi-channel Cell Test System connected with a Solartron 1255B Frequency Response Analyzer (FRA). The effective carrier concentration is given by equation 3.8.

$$N_A = \frac{2}{q\varepsilon_0\varepsilon_r A^2 \left[\frac{d\left(1/C^2\right)}{dV}\right]} \qquad 3.8$$

where, ε_0 and ε_r are the free space permittivity and the dielectric constant of CZTSSe. A literature reported value of $\varepsilon_r = 7$ has been considered for our calculation. According to Eq. 3.7, the $1/C^2$ vs V plot should be a straight line whose intercept with the Y-axis represents the carrier concentration N_A.

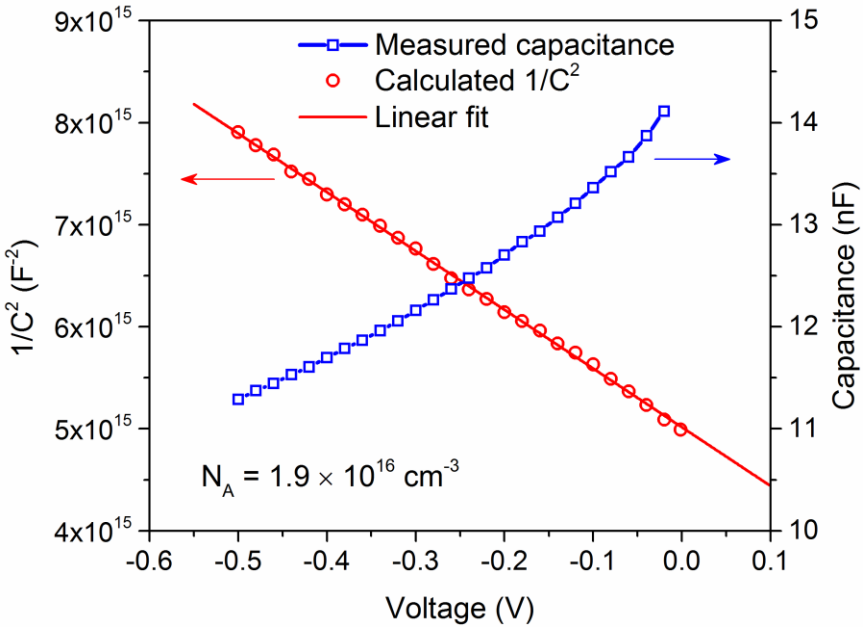

Figure 3.8. Capacitance vs voltage and Mott-Schottky plots for CZTSSe Cell # 4.

The capacitance were measured at 100 KHz at a reverse bias sweep from zero to -0.5 V and the data is plotted in Figure 3.8. From the Mott-Schottky plot ($1/C^2$ vs V) straight line fitting, a free carrier concentration of 1.9×10^{16} cm^{-3} was estimated for the CZTSSe device.

3.4 CONCLUSION

The fabricated solar cells were characterized by current-voltage and capacitance-voltage measurements. PV performance of the cells were evaluated under illumination and the diode characteristics were extracted from dark I-V measurement. The best cell showed an efficiency of 4.06% and the cell performance was limited by a recombination process at the junction as suggested by temperature dependent V_{OC} measurements.

CHAPTER 4: IMPEDANCE SPECTROSCOPY AND AC EQUIVALENT CIRCUIT ANALYSIS

4.1 OVERVIEW

Impedance spectroscopy (IS) or admittance spectroscopy (AS) is a powerful characterization tool commonly used in electrochemistry for the investigation of bulk materials and solid-electrolyte interfaces. This method had been employed to study the charge carrier dynamics and equivalent circuit modelling of various devices, such as fuel cells, photo-electrochemical solar cells, solid state inorganic p-n junction solar cells, rechargeable batteries and porous electrodes. Also, temperature dependent AS measurements had been used to identify the majority carrier trap levels in solid state p-n junction solar cells. In this work, the impedance spectroscopy was performed to model a small signal ac equivalent circuit of the fabricated CZTSSe solar cells and extract the equivalent circuit parameters. This study provides important information on the electrical behavior of the cell that directly correlates to the physical phenomena inside the device.

4.2 THEORY

The impedance measurement technique involves application of a small alternating voltage signal $v(t) = V_m \sin(\omega t) = V_m e^{j\omega t}$ across the cell followed by the measurement of the resulting current, $i(t) = I_m \sin(\omega t - \theta) = I_m e^{j(\omega t - \theta)}$; where θ is the phase difference between the voltage and the current signals and ω is the cyclic frequency ($\omega = 2\pi f$). The complex impedance of the cell is then calculated using the following formula:

$$Z(t) = \frac{v(t)}{i(t)} = \frac{V_m \ sin\,\omega t}{I_m \ sin(\omega t - \theta)}$$

$$= \frac{V_m \, e^{j\omega t}}{I_m \, e^{j(\omega t - \theta)}}$$

$$= \left(\frac{V_m}{I_m}\right) e^{j\theta} = Z_0 e^{j\theta} = Z_0 \, (\cos\theta + j \sin\theta)$$

$$= Z_0 \, (\cos\theta + j \sin\theta)$$

$$Z(t) = Z' + j\, Z'' = \left(\frac{1}{G}\right) + \, j \, \left(\frac{1}{\omega C}\right) \qquad 4.1$$

The magnitude and the phase shift of the complex impedance are given by:

$$|Z| = \sqrt{(Z')^2 + (Z'')^2} \qquad 4.2$$

$$\theta = \tan^{-1}\left(\frac{Z''}{Z'}\right) \qquad 4.3$$

To study the frequency response of the device under test (DUT), the complex impedance Z is measured over a wide frequency range. The real part ($Z' = Re(Z)$) and the imaginary part ($Z'' = Im(Z)$) of the complex impedance (Z) are then separated out (see equation 4.1) and Z'' is plotted against Z' in a complex impedance plane for the selected frequency range – the plot is known as the 'Nyquist plot' or 'Cole-Cole plot'. Fitting of the experimentally measured data is then carried out to identify the equivalent circuit parameters.

4.3 Experimental Procedure

The Impedance spectroscopy (IS) was performed using a Solartron 1470E multi-channel cell test system connected with a Solartron 1255B frequency response analyzer (FRA). The experimental setup is shown in Figure 4.1. In our study the frequency sweep was carried out from 0.1 Hz to 1 MHz and the amplitude of the applied AC signal was

fixed at 25 mV. All measurements were carried out under dark condition and at 297K ambient temperature. The instrument control, data acquisition and analysis was performed by 'ZView' software.

Figure 4.1. Photograph of the impedance measurement setup: Solartron 1255B FRA connected to Solartron 1470E Cell Test System.

4.4 RESULTS AND DISCUSSION

The impedance spectra were collected under dark at different reverse bias conditions. Nyquist plots of Cell # 4 at different DC biases are shown in Figure 4.2. The amplitude |Z| and the phase shift θ as a function of frequency are plotted in Figure 4.3. respectively. The real and the imaginary parts of the complex impedance as a function of frequency are plotted in Figure 4.4. The real part and the imaginary part of the complex impedance as a function of frequency at different DC bias levels.

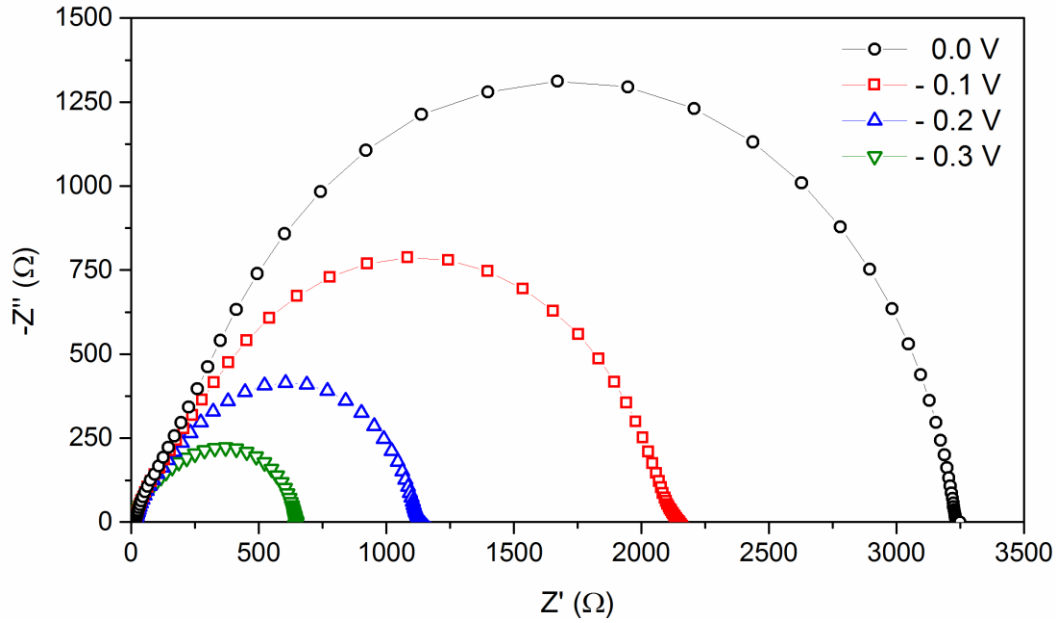

Figure 4.2. Nyquist plot of Cell # 4 under different DC bias measured under dark.

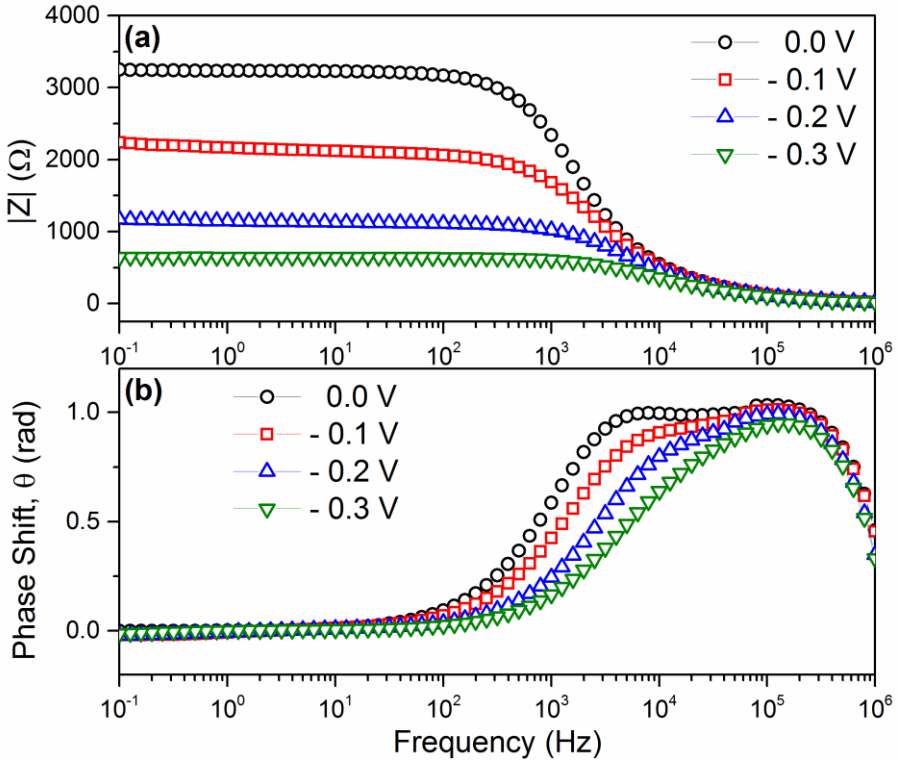

Figure 4.3. (a) The amplitude of the complex impedance (|Z|) and the phase shift (θ) as a function of frequency at different DC bias levels corresponding to the impedance data presented in Figure 4.2.

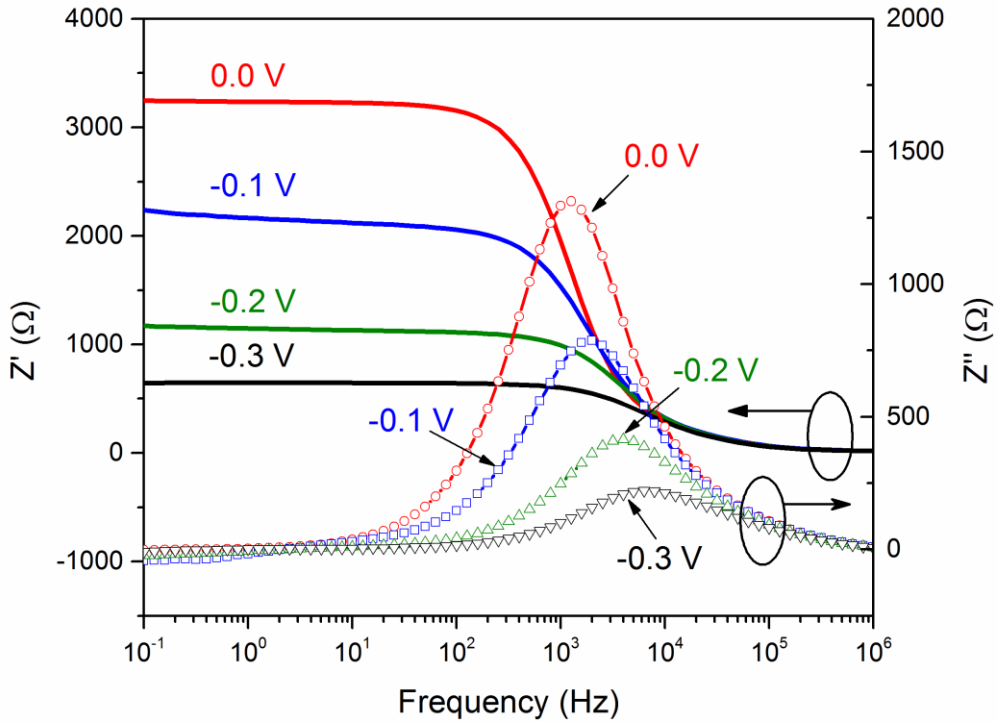

Figure 4.4. The real part and the imaginary part of the complex impedance as a function of frequency at different DC bias levels.

In order to fit the experimentally measured data, we reviewed possible equivalent circuit models and evaluated the frequency response of different models compared to the measured impedance data. Four different models have been analyzed in this study, starting from the simplest one – Model 1, to the most complex one – Model 4. Each of these four equivalent circuit models are investigated in the following section. Fitting was performed on the experimental data obtained at 0 V DC bias.

The simplest equivalent circuit of a heterojunction solar cell can be modeled by a network of three circuit elements considering a defect-free ideal p-n junction device and perfect Ohmic contacts at the front and back electrodes. The circuit consists of a resistance (R_S) connected in series with another resistance (R_J) and capacitance (C_J) connected in parallel as shown in Figure 4.5. The series resistance R_S accounts for the bulk and contact

resistances, and the CZTSSe/CdS heterojunction is modeled by the parallel network of the resistance R_J and the capacitance C_J. The real and the imaginary parts of this electrical network are calculated as follows:

$$Z' = Re(Z) = R_S + \frac{R_J}{1 + \omega^2 C_J^2 R_J^2} \quad 4.4$$

$$Z'' = Im(Z) = -\frac{\omega C_J R_J^2}{1 + \omega^2 C_J^2 R_J^2} \quad 4.5$$

According to Eq. 4.4 and Eq. 4.5, the impedance characteristic of this electrical network should be a perfect semicircle on the complex plane, as shown in Figure 4.5. The diameter of the semicircle is equal to the junction resistance R_J, and the displacement of the semicircle from the origin is measured by R_S on the real axis. The maximum value of the imaginary impedance Z_0'' (corresponding to the real impedance Z_0' shown in Figure 4.5, lying at the center of the semicircle) is given by Eq. 4.6 from which the junction capacitance C_J can be calculated.

$$Z_0'' = R_j = \frac{1}{\omega_0 C_j} \quad 4.6$$

$$\omega_0 = \frac{1}{R_j C_j} = \frac{1}{\tau} \quad 4.7$$

This simple R-RC model has a single time constant τ. An attempt to fit the experimental data (acquired at 0V DC bias) using Model 1 showed large deviation between the simulated and measured data which suggests presence of more circuit elements in the device. The data fit and the deviation in impedance amplitude ($|Z|$) are shown in Figure 4.9 and Figure 4.10 respectively. It is clearly visible from Figure 4.2 that the plots are not perfect semicircle in nature and therefore it is justified that Model 1 is not sufficient to represent the electrical characteristic of the solar cell under test.

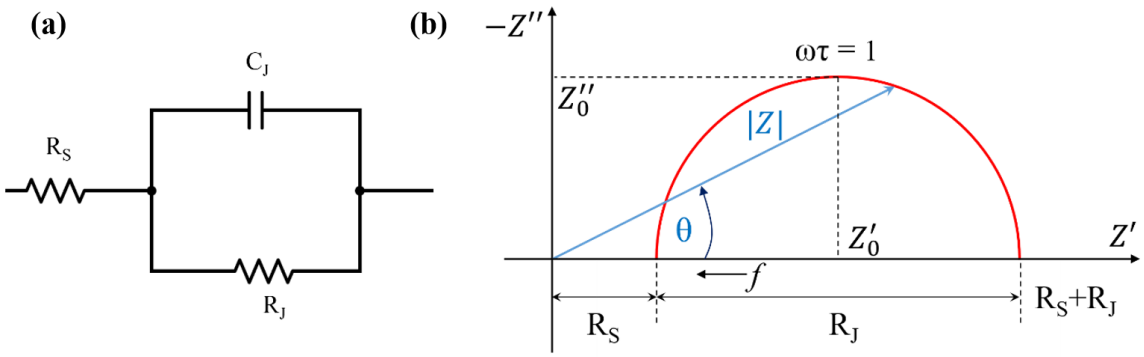

Figure 4.5. (a) The simple R-RC three component equivalent circuit 'Model 1' considering a perfect heterojunction solar cell and (b) the simulated Nyquist plot of the network representing various equivalent circuit parameters.

It is evident from Figure 4.2 that the circular shape is distorted at the high frequency region which is most likely due to the superposition of another smaller semicircle with the main one. Presence of another superimposed semicircle suggests another parallel RC network to be connected in series with the existing R-RC network. This second RC network represents another diode in the device which is most likely due to the presence of a blocking barrier at the back contact that was ignored in Model 1. This speculation is further supported by the cross-sectional SEM studies where a $Mo(SSe)_2$ interfacial layer was observed at the rear contact. Existence of such blocking diode at the Mo-CZTSSe interface have been reported by many research groups. Therefore, in Model 2 we incorporated another parallel RC network ($R_B||C_B$) as shown in Figure 4.6 taking the back contact blocking layer into account.

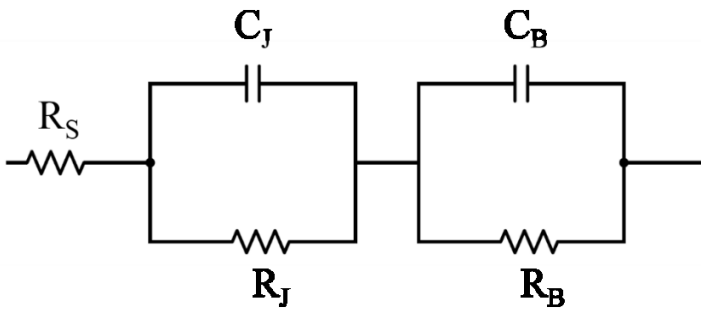

Figure 4.6. The equivalent circuit 'Model 2' with two parallel RC networks including the back contact blocking diode.

A significant improvement of the fitting was achieved using Model 2 compared to Model 1 with a much smaller $|Z|$ deviation as shown in Figure 4.9 and Figure 4.10 respectively. However, ~10% residual mismatch between the experimental and simulated result indicates that further correction of the equivalent circuit 'Model 2' is necessary.

In the next step, in Model 3 we account for the contribution from any possible defect levels in the cell. Defects in the absorber layer is represented by a series connected capacitance and resistance in parallel ($R_1||C_1$) to the heterojunction RC network. The resulting equivalent circuit is shown in Figure 4.7.

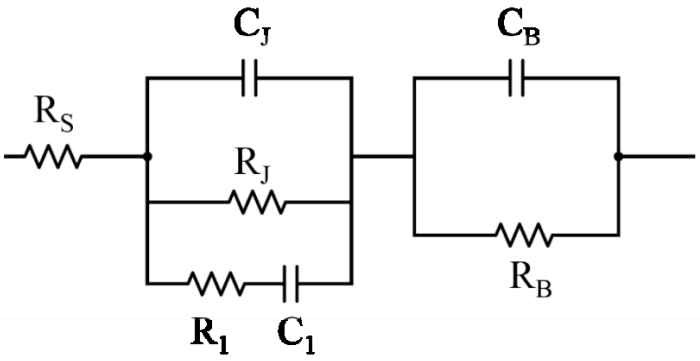

Figure 4.7. The equivalent circuit 'Model 3' showing circuit elements representing the heterojunction, back contact blocking diode, and the contribution from defect levels in the CZTSSe absorber layer.

The simulated frequency response of this system is shown in Figure 4.9 and Figure 4.10 respectively. The simulated data fit well to the experimental data in the low frequency region and a residual mismatch of about ±5% between 1 KHz to 1 MHz was observed. However, from Figure 4.9, it is evident that 'Model 3' requires modification to fit the measured impedance values.

One key observation in Figure 4.9 is that the actual semicircle is depressed compared to all three simulated circles. This suggests the existence of a Constant Phase Element (CPE) in the system. CPE-R sub-networks had been used to account for the non-ideality in solid state heterojunction solar cells. A CPE is a 'capacitor-like' passive element that exhibits frequency dependent electrical impedance with a constant phase difference over the frequency range. The complex impedance of a CPE is given by Eq. 4.8.

$$Z = \frac{1}{T(j\omega)^P} \qquad 4.8$$

where T is a frequency independent term and P defines the non-ideality of the element. The value of P lies in between 0 and 1 ($0 \leq P \leq 1$) and for P = 1, Eq. 4.8 becomes identical to that of an ideal capacitor. Equivalent circuit models using CPE had been previously used to define CdTe/CdS thin film solar cells and it has been demonstrated that some defects in the absorber bulk or at the junction show frequency dependent behavior and can only be modeled using a constant phase element. In Figure 4.8, the modified 'Model 4' is shown which has the same structure as 'Model 3' except that the capacitance C_1 in 'Model 3' has been replaced by a constant phase element CPE_1.

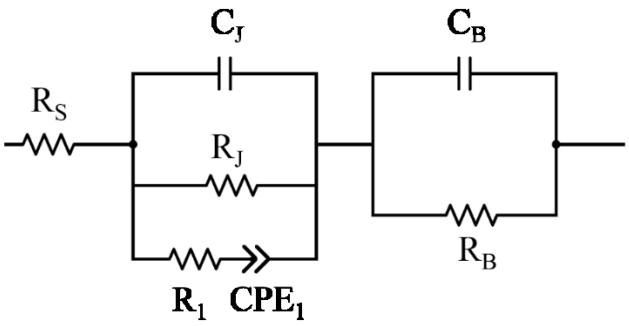

Figure 4.8. The equivalent circuit 'Model 4' obtained by replacing C_1 in 'Model 3' by a constant phase element CPE_1 that defines the electrical behavior of the defects in the CZTSSe absorber layer more accurately.

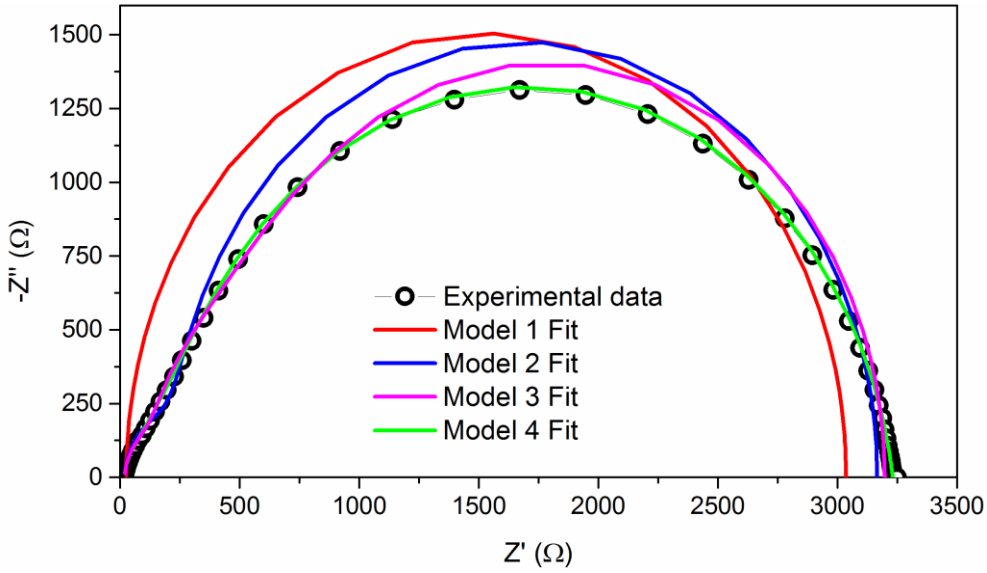

Figure 4.9. Fitting of the simulated ac response of different equivalent circuit model to the experimental data.

It can be observed in Figure 4.9 that 'Model 4' fits the experimentally measured data near perfectly. The residual mismatch is less than ±2% within 100 KHz and above that showed a minimal mismatch of ~±4%. It is possible to have pronounced contribution from more than one type of defect in the cell. However, adding more R-CPE elements to the existing network did not show any improvement over 'Model 4'. Therefore, we conclude

that ‘Model 4’ represents the ‘ac equivalent circuit’ of the fabricated CZTSSe solar cell that is sufficient to accurately define the ac response of the device.

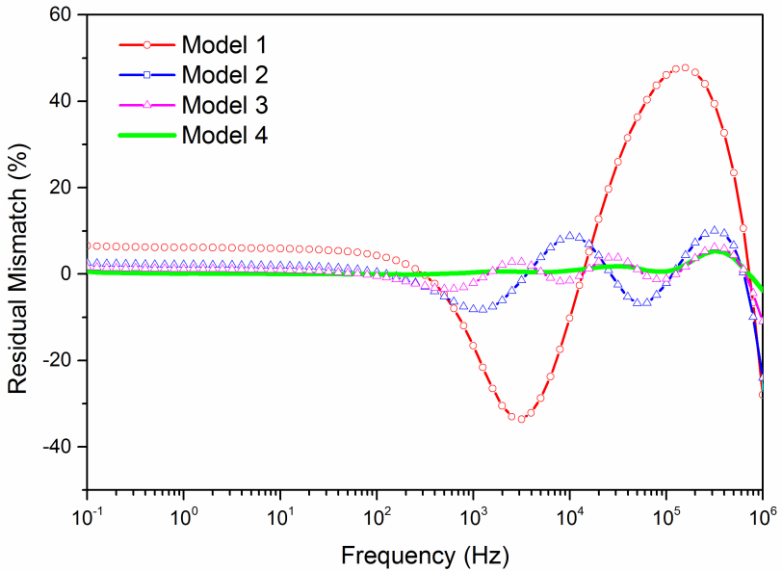

Figure 4.10. Residual mismatch of the fitted impedance amplitude data (|Z|) to the actual experimental result.

4.5 CONCLUSION

Impedance spectroscopy was performed on the fabricated CZTSSe solar cells and an AC equivalent circuit model was proposed. The impedance analysis confirmed the presence of a blocking diode at the Mo-back contact and also suggested the presence of a major recombination phenomena exhibiting frequency dependent behavior and was modelled by a constant phase element. The AC equivalent circuit parameters were calculated from the fitted model.

CHAPTER 5: DEFECT LEVEL STUDY BY DEEP LEVEL TRANSIENT SPECTROSCOPY

5.1 DEEP LEVEL TRANSIENT SPECTROSCOPY (DLTS)

5.1.1 Introduction

The conventional capacitive DLTS (C-DLTS) technique is a very sensitive tool to identify electrically active defects in semiconductors in terms of activation energy, defect type, and trap concentration [118] and have been widely used for deep and shallow level defect characterization of chalcopyrites and chalcogenides. [119] [120] The CZTSSe cells under investigation exhibited large depletion capacitance (C_d) beyond the detection limit of our DLTS system and therefore we have used current-mode DLTS (I-DLTS) technique which uses current transient measurements to identify the defect levels. Although, unlike C-DLTS, I-DLTS cannot distinguish between a majority and minority carrier trap, but it provides valuable information relating to the defect activation energies, defect concentration, and the capture cross-sections of the defect centers.

In this section the cell prepared at USC (lower efficiency CZTSSe cell) is referred to as 'Cell 1' and the higher efficiency cell prepared at NREL is referred to as 'Cell 2'. Both cells were characterized by I-DLTS measurements in this study and their photovoltaic performances are correlated to the identified defect levels. For a comparison of the PV performance, the J-V characteristics of both cells under dark and under simulated AM 1.5 illumination are presented in Figure 5.1. Cell 1 showed a higher open-circuit voltage (V_{OC}) of 506 mV compared to Cell 2, which exhibited a maximum V_{OC} = 350 mV at 297K.

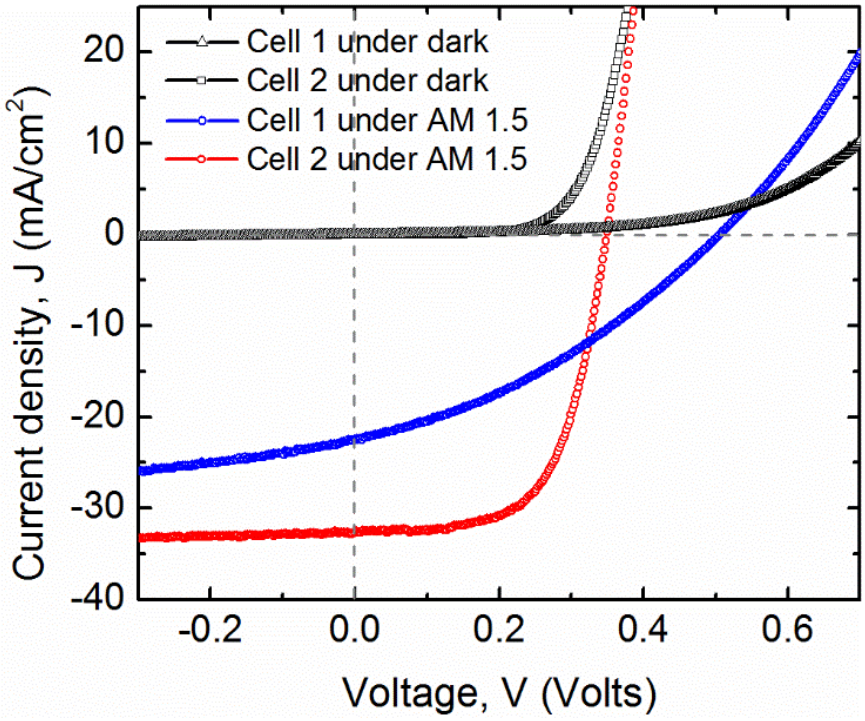

Figure 5.1. J-V characteristics of the two cells under dark and under AM 1.5 simulated illumination.

5.1.2 Theory of DLTS Measurement

In a semiconductor material, defect centers could either act as an electron trap or a hole trap. Associated with these trap levels four fundamental phenomena may occur as illustrated in Figure 5.2. Electrons could be trapped by a defect level acting as an electron trap, the process known as electron capture and consequently a trapped electron may get de-trapped if sufficient thermal energy is available, the process is known as electron emission. Similarly, a hole capture process is characterized by trapping of a hole by a defect level and the hole emission process by de-trapping of a previously captured hole.

Different defect levels are activated at different temperatures and a temperature scan of the current transients are analyzed to extract the defect parameters. In Figure 5.3, a double boxcar method is shown by which a DLTS signal is generated from a temperature

dependent scan of the current transients. As shown in Figure 5.3, current transients are recorded within a rate window t1-t2. Transients at increasing temperatures from T1 to T9 are shown and it is considered that a defect level is activated somewhere in this selected temperature range. The current difference (ΔI) within the rate window is then plotted against the temperature to generate the DLTS signal. At low temperatures, the transients take long duration to decay. As the temperature is increased, the decay becomes steeper as the trapped carriers get more thermal energy and is easily de-trapped. However, at much higher temperature, the decay is so fast that it comes back to its equilibrium before the initial delay time. Hence, a current deviation (ΔI) within the rate window is plotted against temperature to form the DLTS signal.

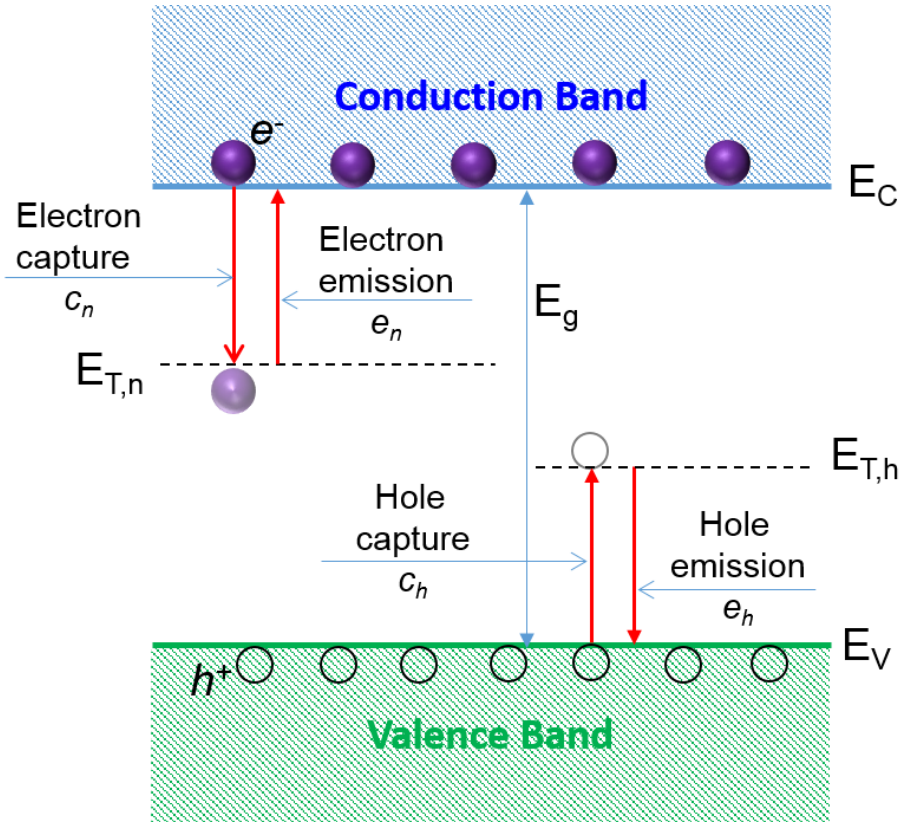

Figure 5.2. Illustration of electron and hole trapping and de-trapping phenomena in a semiconductor material.

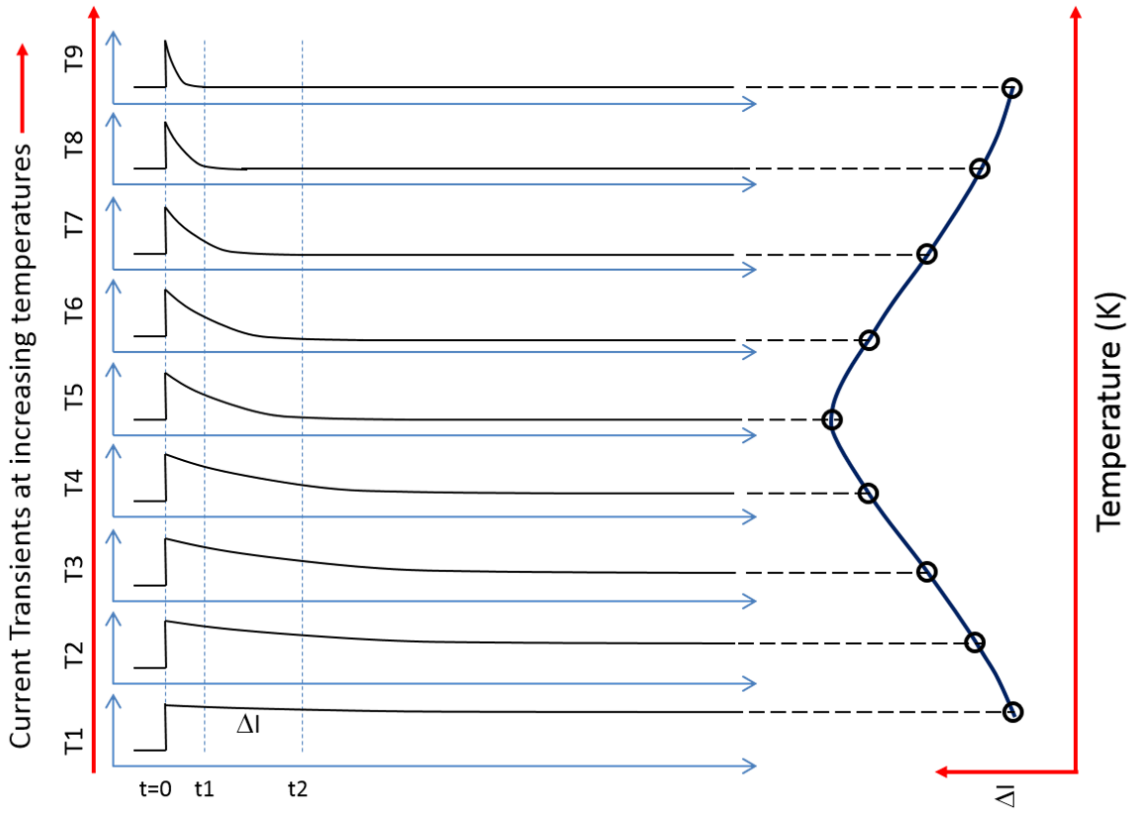

Figure 5.3. The double boxcar method used to generate the I-DLTS signal from a temperature dependent current transient scan.

5.1.3 Experimental Procedure

A SULA DDS-12 DLTS system was operated in current transient spectroscopy (CTS) mode to obtain I-DLTS spectra. Photograph of the system and a schematic of the experimental set-up illustrating various component blocks are presented in Figure 5.4 and Figure 5.5 respectively. The samples were mounted on a JANIS VPF800 cryostat stage controlled by a Lakeshore 335 temperature controller.

The cells were reverse biased at V_R = -0.4 V and a trap filling forward pulse of amplitude V_a = +0.3 V with 10 ms pulse width was applied following which the current transients were recorded. The transient signals were successively processed by the CTS unit and the I-DLTS spectra were generated by choosing a suitable rate window using the

correlator units to calculate the emission rates at different temperatures following the standard double boxcar method. The correlator unit in DDS-12 is capable of assigning multiple rate windows in a single thermal scan.

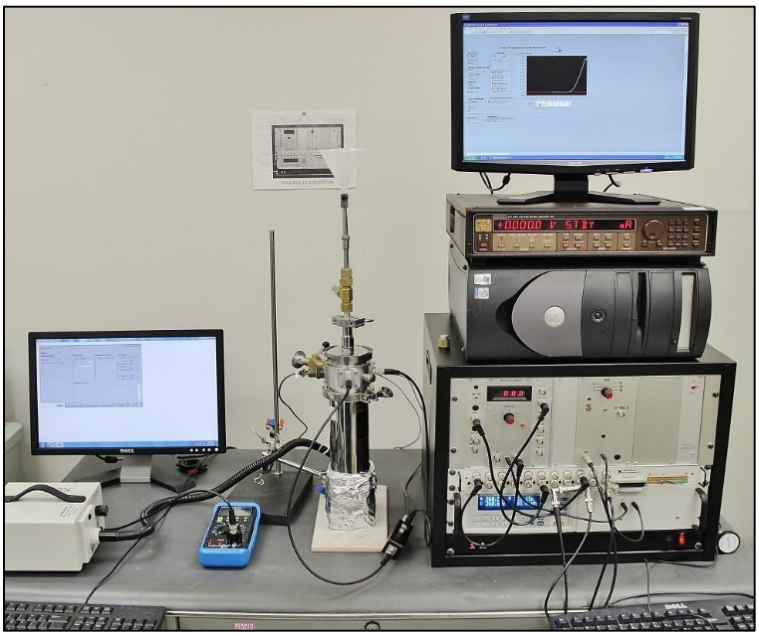

Figure 5.4. Photograph of the SULA DDS-12 DLTS measurement system.

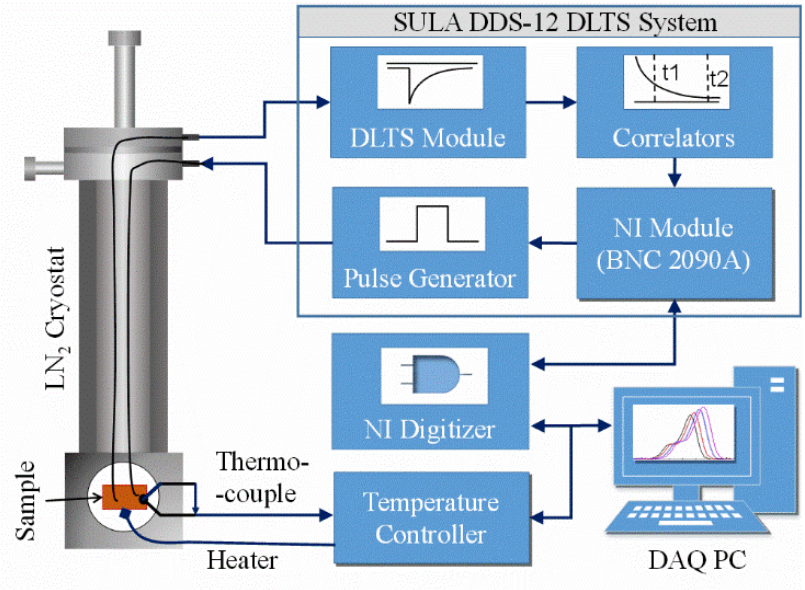

Figure 5.5. Schematic of the SULA DDS-12 DLTS setup showing main component blocks.

From equation 5.1 given below, [121] it can be seen that the expression of the current transient in I-DLTS also contains the steady-state diode leakage current.

$$i(t) = \frac{qWA}{2\tau_{e,h}} N_T(t) + I_L \qquad 5.1$$

where, q is the electronic charge, W is the width of the measurement volume, A is the diode area, $\tau_{e,h}$ is the decay constant for the current transients corresponding to electron or hole emissions, and N_T is the concentration of trapped charge carriers. If the diode leakage current exceeds a certain limit it can obscure the current transients. The correlator unit also removes the background leakage current prior to the measurements to avoid any such issues. The current transient captures were time delayed after the end of each filling pulse by an amount called the *initial delay*. The rate windows τ for the transient capture are dependent on the *initial delays* according to the following relation:

$$\tau = {}^{1}\Big/\big(1.94 \times initial\ delay\ (ms)\big) \qquad 5.2$$

The capture cross-sections and the trap concentration were calculated from the I-DLTS plots. The activation energies (E_T) of the deep centers were extracted from the Arrhenius plots obtained from the emission rates calculated from the current transients.

5.1.4 Results and Discussion

The I-DLTS scans of Cell 1 and Cell 2 in the temperature range of 85-325 K are shown in Figure 5.6. It can be readily observed that the defect characteristics in these two cells are quite different. For Cell 1, two broad peaks were noticed, one close to 190 K (Peak 1), and the other one close to 285 K (Peak 2) for the lowest initial delay of 0.1 ms. Such broad peaks signify a slow emission rate of the defect centers. Interestingly, none of these two peaks were observed in Cell 2, rather a new peak (Peak 3) appeared close to 100 K

(for an initial delay of 0.02 ms) which is much narrower signifying a faster emission of trapped carriers from the associated defect center.

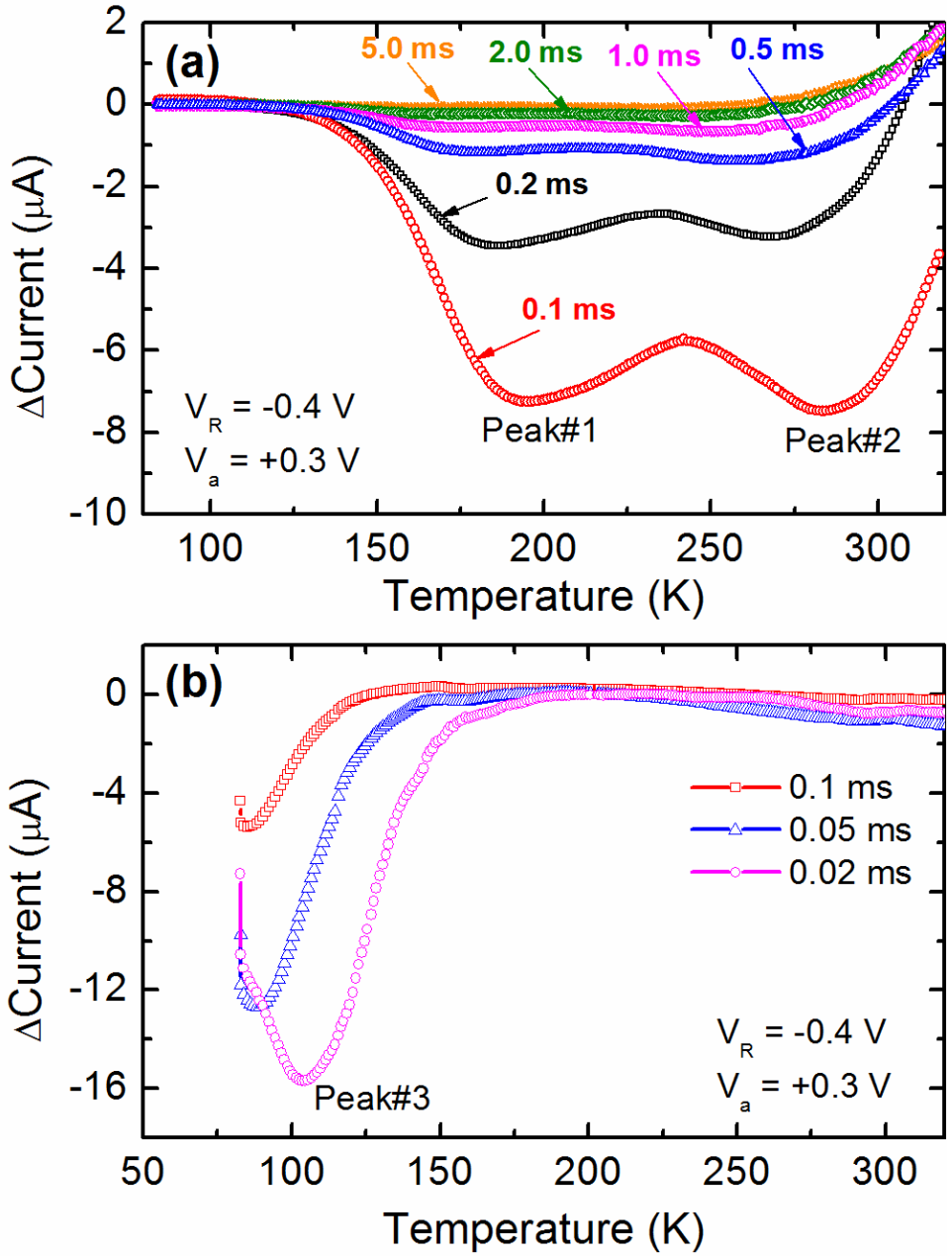

Figure 5.6. I-DLTS signal of (a) Cell 1 and (b) Cell 2.

The Arrhenius plots corresponding to the observed peaks in the I-DLTS scan are shown in Figure 5.7. Activation energies of E_{T1} = 0.12 eV and E_{T2} = 0.32 eV were extracted

corresponding to peaks 1 and 2 respectively. Due to the broad distribution of the emission rates, the uncertainties in the activation energies in Cell 1 were estimated to be ±0.04 for E_{T1} and ±0.06 eV for E_{T2}. An activation energy of E_{T3} = 0.03±0.01 eV was calculated corresponding to the peak 3 in Cell 2.

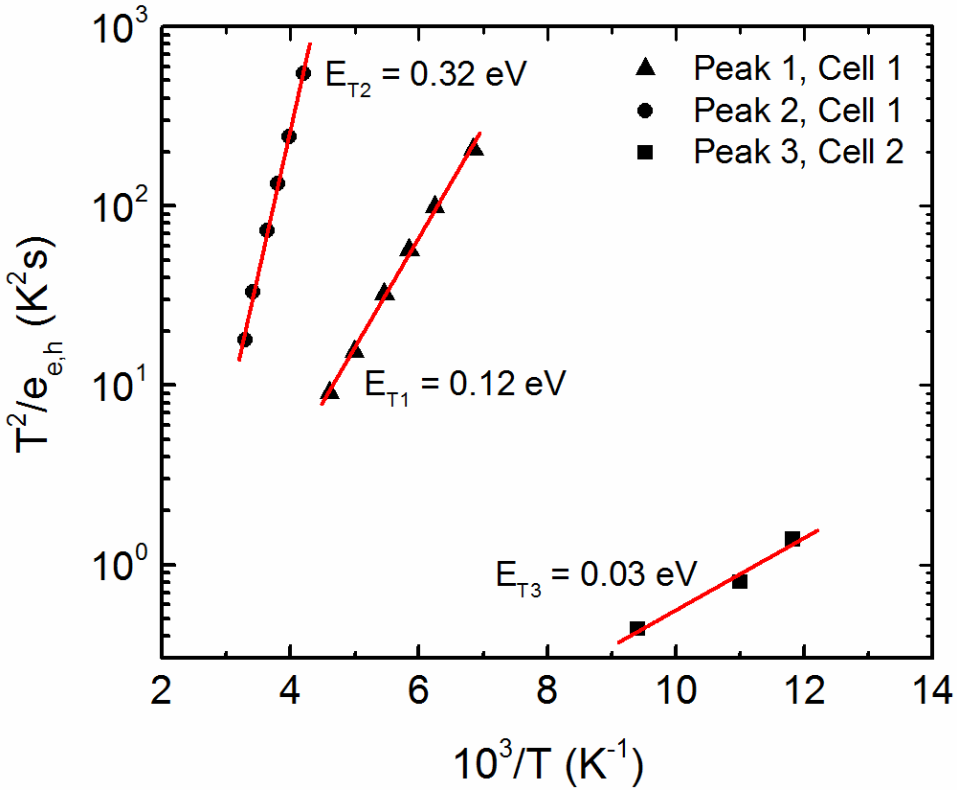

Figure 5.7. Arrhenius plots corresponding to the peaks obtained from I-DLTS spectra. The solid straight lines show the linear fit to the experimental data points.

Recent theoretical analysis of defect models in kesterite CZTS and CZTSe materials [38] [48] [49] [51] [53] [55] [61] have been considered to assign the experimentally observed defect levels in this study. Nagoya et al., [48] Maeda et al., [51] [55] and Chen and co-workers [38] [49] [53] [61] have carried out systematic theoretical studies on the intrinsic point defects in CZTS/CZTSe and calculated the formation energies and corresponding transition (activation) energies for various point defects.

It is predicted that the acceptor defects (Cu_{Zn}, V_{Cu}, Zn_{Sn}, V_{Zn}, Cu_{Sn} etc.) have much lower energy of formation compared to the donor defects in these material systems for Cu-poor composition. The Cu_{Zn} antisite defect has the lowest formation energy which acts as an acceptor level located about 0.10-0.15 eV above the valence band maxima (VBM) [38] [53] [61] and is considered to be responsible for the intrinsic p-type conductivity of these materials. The copper vacancy (V_{Cu}) has comparatively higher energy of formation than Cu_{Zn} antisite and contributes to a much shallower acceptor level at ~0.02 eV above the VBM. [53] It is suggested that V_{Cu} is much preferable than the Cu_{Zn} antisite for high performance solar cells, since Cu_{Zn} produces deeper acceptor level than V_{Cu} and is thus detrimental to the cell performance. Existence of Cu_{Zn} deep level at E_v+0.12 eV has also been experimentally identified by admittance spectroscopy. [122]

The theoretical studies strongly suggest that the observed trap level E_{T1} in Cell 1 with an activation energy of 0.12 eV can be assigned to the Cu_{Zn}(-/0) antisite defect. The second dominant defect level identified in Cell 1 (E_{T2}) corresponds to a much deeper level with an activation energy of 0.32 eV which matches closely to the transition energy theoretically calculated for Cu_{Sn} (2-/-) defect [38] [61]. The larger capture cross-section of E_{T2} compared to that of E_{T1} also suggests that E_{T2} has a more negatively charged state. Therefore, we attribute the deep level at E_v+0.32 eV to the Cu_{Sn} (2-/-) antisite defect.

In Cell 2, the activation energy of trap level E_{T3} = 0.03 eV can be assigned to the copper vacancy (V_{Cu}), as no other shallow level in this range exists in these materials. The experimentally identified value of E_v+0.03 eV is in good agreement with the theoretical predicted value of 0.02 eV. All the experimentally identified defect parameters including

the defect activation energy (E_T), capture cross-section (σ_T), trap concentration (N_T), and the associated point defects are summarized in Table 5.1.

We would like to emphasize that a device having shallow defect levels is expected to exhibit superior performance than a device with deeper defect levels. Our results follow this trend with Cell 2 showing much better photovoltaic performance compared to Cell 1. However, the most interesting observation in this study is the presence of shallow V_{Cu} level in purely Se containing CZTSe sample (Cell 2) which suggests that although Cu_{Zn} has a lower formation energy, it is possible to have V_{Cu} as the predominant lattice defect in kesterites. Our results also indicate that the intrinsic p-type conductivity of high-efficiency CZTSSe absorbers could be due to the formation of copper vacancies (V_{Cu}) similar to chalcopyrites and the formation of detrimental Cu_{Zn} antisites can be avoided.

Table 5.1. Summary of the observed defect levels in the CZTSSe solar cells by I-DLTS.

Cell ID	Peak ID	Approx. Peak Temperature (K)	Activation Energy, E_T (eV)	Capture cross section, σ_T (cm^2)	Trap Conc. N_T (cm^{-3})	Possible defect level
Cell 1	Peak 1	190K	0.12±0.04	1.31×10^{-20}	6.17×10^{14}	Cu_{Zn}
	Peak 2	285K	0.32±0.06	2.04×10^{-18}	6.73×10^{14}	Cu_{Sn}
Cell 2	Peak 3	100K	0.03±0.01	2.52×10^{-20}	6.46×10^{15}	V_{Cu}

5.1.5 Conclusions

In conclusion, we have performed current DLTS measurements on two Cu-poor and Zn-rich CZTSSe solar cells with different chalcogen ratios to probe electrically active intrinsic point defects. The lower efficiency CZTSSe cell (S/Se = 1.4) showed two dominant deep acceptor levels at E_v+0.12 eV and E_v+0.32 eV corresponding to Cu_{Zn} and

Cu_{Sn} antisites, whereas the pure CZTSe (S/Se=0) higher efficiency cell showed only a shallow V_{Cu} level at E_v+0.03 eV. Our investigation leads to a new finding that V_{Cu} could be the predominant lattice defect in high efficiency kesterite cells instead of the detrimental Cu_{Zn} antisites.

CHAPTER 6: BULK CZTSSe GROWTH AND CHARACTERIZATION

6.1 OVERVIEW

Most of the research efforts on CZTSSe have been dedicated on the growth of thin-films and investigations of physical properties of the films. A very few literature reports are available on the bulk crystal growth of CZTS-based compounds [44] [45] [123] [124] [46] [125] [46] [47] [126]. Growth of CZTS(Se) compounds from a melt is highly challenging as the crystallization process passes through a peritectic reaction of solid/liquid ZnS(Se) phases and exhibits a very confined region of stability in the $Cu_2S(Se)$-$ZnS(Se)$-$SnS(Se)_2$ ternary phase diagram [44] [45]. A solution growth or a gradient freeze technique is thus more suitable to grow large volume of single crystals of these materials. CZTS(Se) single crystal growth have been attempted using iodine transport method, travelling heater method, solution fusion method using Sn solvent, and molten KI as the flux material. These methods suffer from low yield, poor reproducibility, and relatively higher cost of production. Vertical gradient freeze (VGF) technique offers a large volume of crystal growth with low defect density, lower cost, and great reproducibility. VGF method has been successfully used for the growth of high quality III-V and II-VI compounds. We have successfully grown large grain, high-quality $Cu_2ZnSn(S_xSe_{1-x})_4$ crystals using a novel Vertical Gradient Freeze (VGF) technique for the first time. Three individual crystal ingots were grown with varying S/Se content: (a) pure S-based Cu_2ZnSnS_4, (b) purely Se containing $Cu_2ZnSnSe_4$, and mixed sulfo-selenide $Cu_2ZnSn(S_xSe_{1-x})_4$ with a sulfur to

selenium molar ratio of 1:1. The structural and compositional properties of the grown crystals were investigated.

6.2 EXPERIMENTAL

6.2.1 Crystal Growth: Vertical Gradient Freeze (VGF) Technique

The $Cu_2ZnSn(S_xSe_{1-x})_4$ crystal growth were carried out using an in-house built custom made vertical Bridgman crystal growth furnace equipped with three independently controllable temperature zones. The furnace setup is shown in Figure 6.1. The three zones of the crystal growth furnace consisted of three ring heaters positioned at ~23 cm apart from each other rated up to a maximum of 2.0 KW of power with a peak continuous operating temperature of 1150°C.

Stoichiometric amounts of high purity (6N) Cu, Zn, Sn, sulfur (S), and/or in-house zone refined (>7N) selenium (Se) were loaded in a quartz ampoule. For mixed $Cu_2ZnSn(S_xSe_{1-x})_4$ crystal growth, equimolar amounts of S and Se corresponding to a S/(S+Se) molar ratio of x = 0.5 was used. Quartz ampoules of different dimensions were used for the three growths. A CAD design of the ampoule used for $Cu_2ZnSn(S_xSe_{1-x})_4$ (x=0.5) crystal growth can be found in APPENDIX C –. The total weight of the charge for each growth was varied and the details of the loaded precursor amounts are listed in Table 6.1. The precursors were loaded into the ampoule inside a glove box filled with ultra-high pure Ar in order to avoid contact with oxygen and moisture from the ambient.

The loaded ampoules were taken out of the glove box and quickly installed in an in-house built ‘ampoule sealing station’. The sealing station is equipped with an oil-free mechanical pump and a turbo-molecular pump. Photograph of the sealing station setup is included in APPENDIX C –. The ampoules were then evacuated to 2×10^{-6} torr and sealed

by fusing a quartz plug using a hydrogen-oxygen torch under continuous evacuation. The bottom part of the ampoule was submerged into a liquid nitrogen (LN_2) filled dewar flask to avoid evaporation of volatile sulfur or selenium during the sealing process.

Figure 6.1. The vertical Bridgman furnace used for the CZTSSe bulk crystal growth by Vertical Gradient Freeze (VGF) technique.

Table 6.1. Summary of the amounts of elemental precursors used for $Cu_2ZnSn(S_xSe_{1-x})_4$ crystal growth.

Grown crystal	Amounts of precursor elements loaded in ampoule					
	Cu (gm)	Zn (gm)	Sn (gm)	S (gm)	Se (gm)	Total charge (gm)
CZTS	1.525	0.785	1.425	1.539	-	5.274
CZTSe	1.296	0.667	1.210	-	3.220	6.393
CZTSSe	2.410	1.240	2.251	1.235	2.994	10.13

The furnace profile was programmed to use zone 1 (top) as the hot zone and zone 2/zone 3 (middle and bottom) together as the cold zone for best temperature stability within ±1°C. The ampoules were suspended using a quartz rod and the ampoule tip were leveled at the center of zone 2 heating element. The growth process was similar for all three crystals with a minor variation in the temperature profiles.

During the growth process, the hot zone (zone 1) and the cold zone (zone 2 + zone 3) were ramped up to its peak temperatures of 1100°C and 1000°C respectively in two ramp up stages. The hot zone was programmed to ramp up at the rate of 100°C/h from room temperature to 700°C during the first stage followed by a ramp rate of 10°C/h from 700°C to 1100°C during the second stage. Correspondingly, the cold zone was programmed to attain 600°C in its first stage ramping up at a rate of ~85°C/h and from 600°C to 1000°C at a rate of 10°C/h respectively. A temperature difference of 100°C was achieved resulting in a thermal gradient between the hot and cold zones. Both zones were dwelled at their peak temperatures for 48 h under accelerated ampoule rotation accomplished by switching direction of rotation every 5 minutes (1 rpm max.) to ensure homogeneous melt formation. After 48 hours, both zones were ramped down at -3.2°C/h until the top zone reached to 700°C and the bottom zone reached to 600°C and then power was switched off to allow natural cooling to room temperature in ~8 h. The programmed ramp cycle for the entire growth process in presented in Figure 6.2.

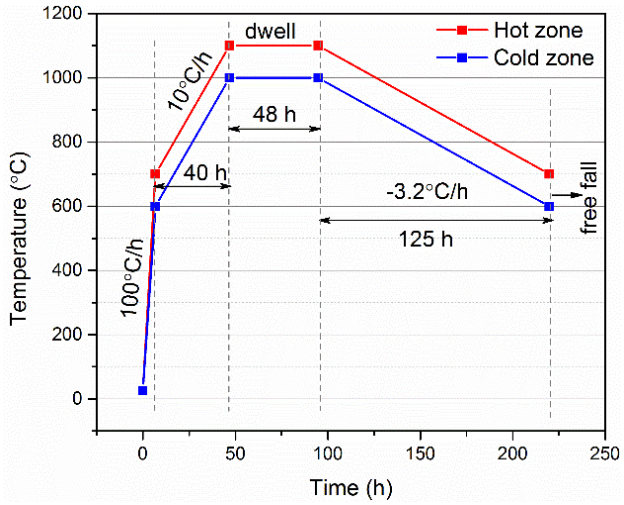

Figure 6.2. Programmed ramp profile of the hot and cold zones of the furnace used for the VGF growth of $Cu_2ZnSn(S_xSe_{1-x})_4$ crystals.

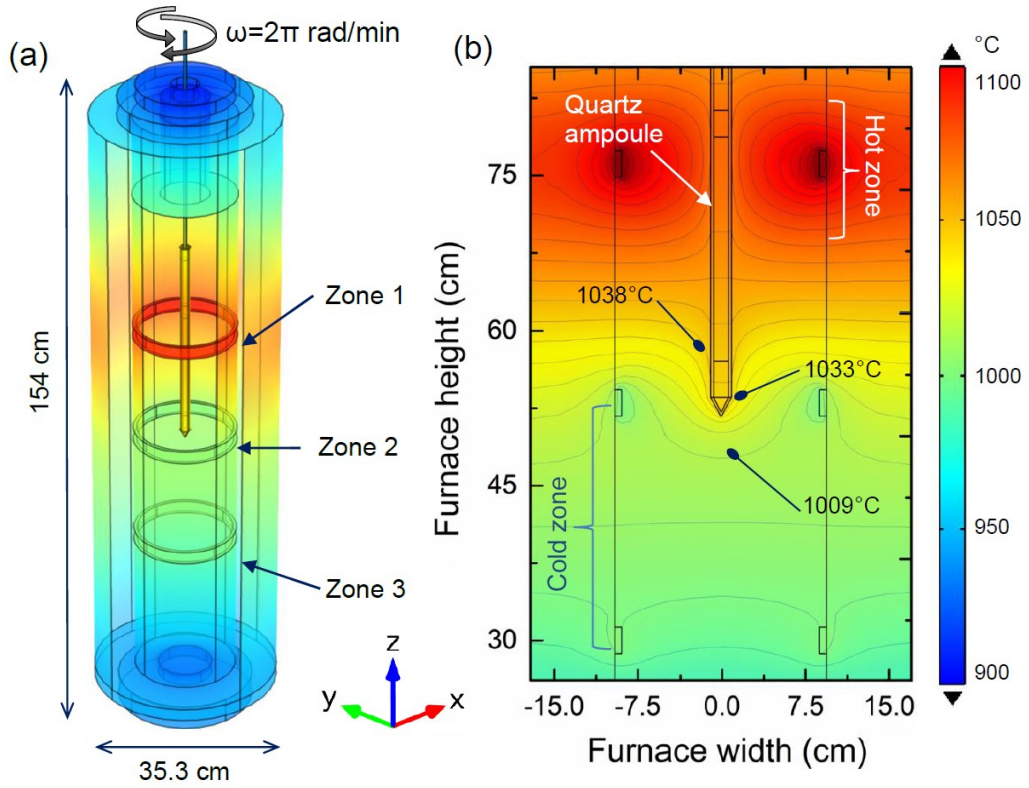

Figure 6.3. (a) 3D schematic of the three-zone furnace used for VGF growth of CZTSSe showing simulated temperature profile under steady state at peak temperatures of (1100/1000/1000°C) for (zone 1/zone 2 /zone 3), and (b) cross-sectional view of the growth furnace showing detailed thermal gradient between the two zones and the temperatures probed near the ampoule tip. (Temperature scale is in °C).

6.3 Bulk Crystal Characterization

The as-grown CZTS, CZTSe, and CZTSSe crystals are shown in Figure 6.4, Figure 6.5, and Figure 6.6 respectively.

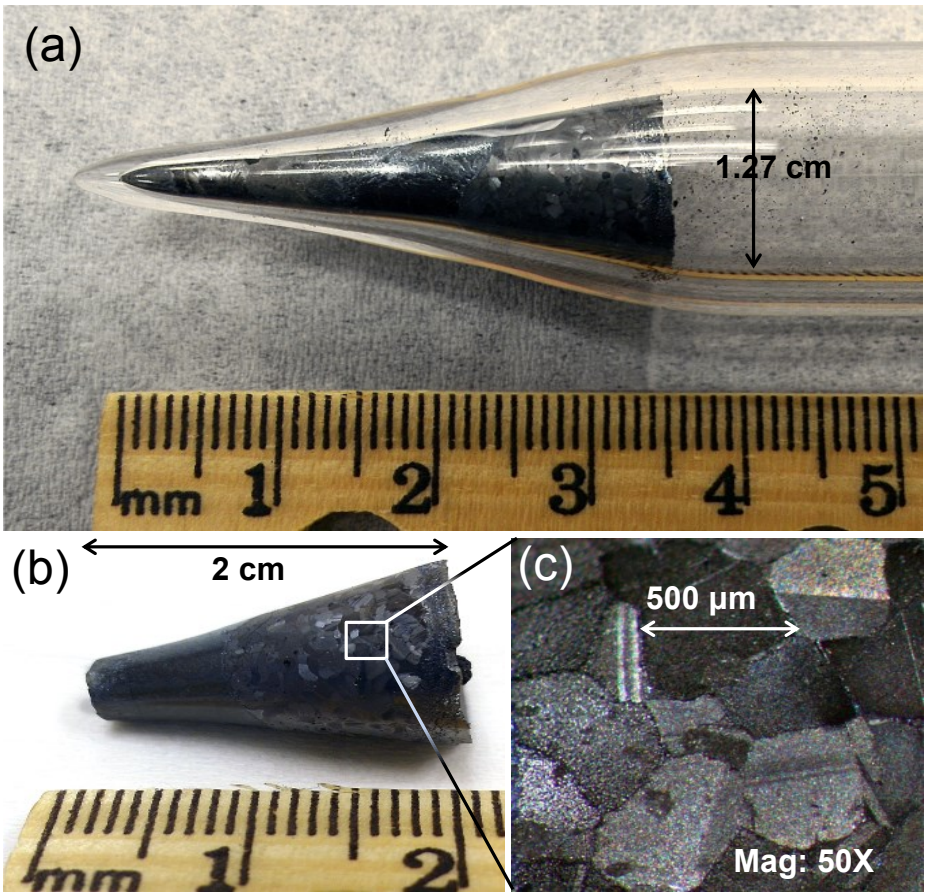

Figure 6.4. Optical photograph of (a,b) as-grown Cu_2ZnSnS_4 ingot (c) optical microscope image of large polycrystals on the surface of the ingot.

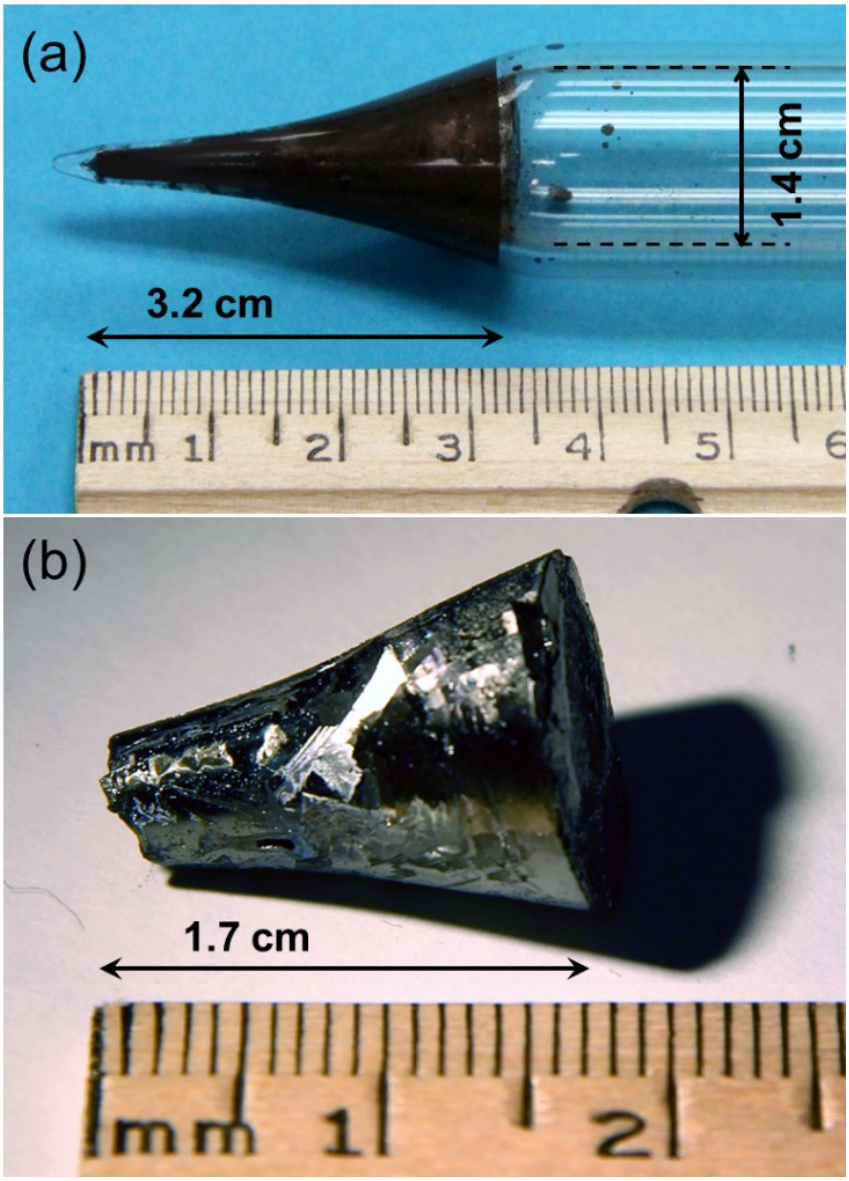

Figure 6.5. Optical photographs of as-grown $Cu_2ZnSnSe_4$ ingot: (a) inside the sealed quartz ampoule, (b) ingot taken out of the ampoule for characterization.

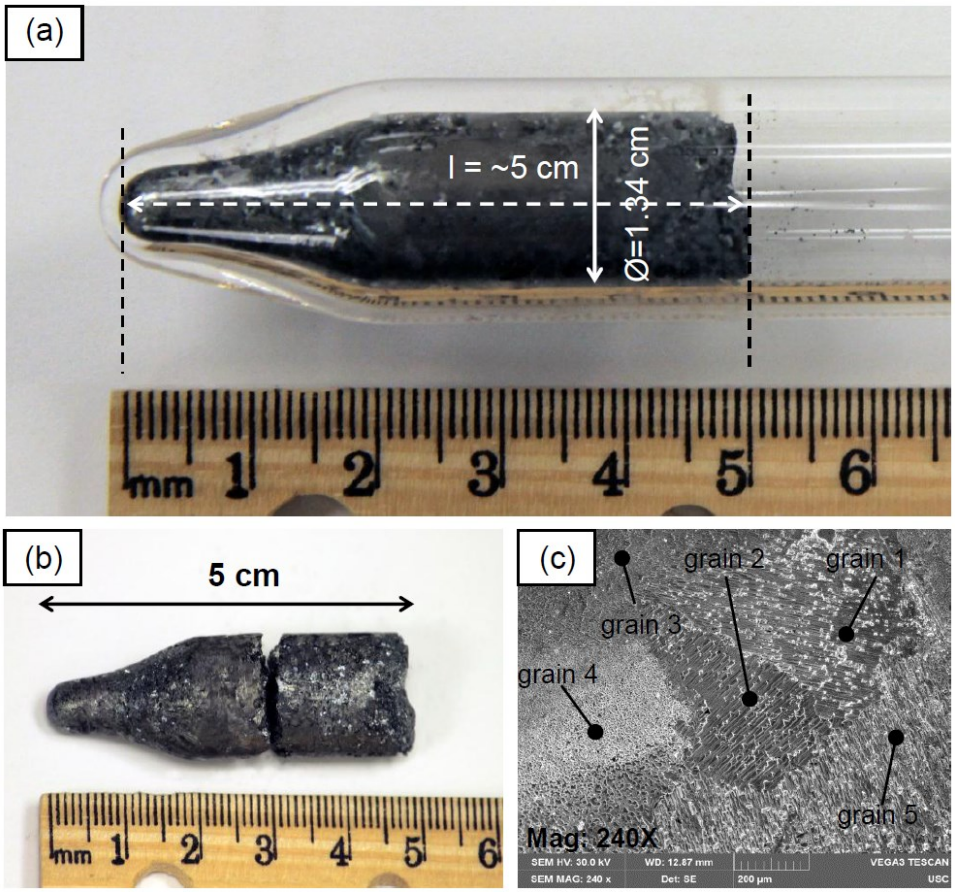

Figure 6.6. Optical photographs of (a, b) as-grown CZTSSe ingot, and (c) SEM image of polycrystalline grains observed on a CZTSSe wafer cut from the as-grown ingot.

The structural characterization of the grown crystals were performed by X-ray powder diffraction method. Powder X-ray patterns were collected on a Rigaku D/Max-2100 powder diffractometer using Cu Kα radiation (λ=1.5418 Å). The XRD scans were carried out in the range of 2θ = 20˚- 90˚ at a scan rate of 1.3˚/min. The phase purity of the grown crystals were further verified by Raman Spectroscopy and the instrument details are noted in section 2.3.1. The composition of the ingots were analyzed by energy dispersive X-ray spectroscopy (EDS) and X-ray photoelectron spectroscopy (XPS). EDS data were collected using a high resolution Tescan Vega 3 scanning electron microscope equipped

with EDS microanalysis and operated at 30 kV acceleration voltage. XPS measurements conditions are detailed in section 2.3.4.

The crystal structures and the lattice constants of the grown crystals were determined by powder X-ray diffraction (PXRD). Figure 6.7 shows the powder XRD pattern for all three $Cu_2ZnSn(S_xSe_{1-x})_4$ crystals. The standard reference peaks for CZTS (JCPDS card no 00-026-0575) and CZTSe (JCPDS card no 00-052-0868) are shown in Figure 6.7.

For CZTS, XRD pattern exhibited strong diffraction peaks at $2\theta = 28.50°$, 47.32° and 56.18° corresponding to (112), (220), and (312) planes of kesterite CZTS structure. Other minor reflections from (200), (224), (008) and (332) planes were also observed. The peak positions found to be in good agreement with the reference diffraction pattern (JCPDS card: 00-026-0575). Sharp diffraction peaks indicated highly crystalline structure and large grains in the grown ingot. The strongest peak (112) located at $2\theta = 28.50°$ was fitted with a Gaussian and the full-width at half-maximum (FWHM) was estimated to be ~0.163°. Such narrow FWHM suggests high quality single crystalline nature of the grown material. The lattice constants calculated from XRD data were a = 5.429 Å and c = 10.847 Å, which are in well agreement with the standard values of a = 5.427 Å and c = 10.848 Å (JCPDS card 26-0575).

No evidence of secondary impurity phases, such as CuS (JCPDS # 06-0464) Cu_2S (JCPDS # 01-072-2276), SnS (JCPDS # 39-0354), SnS_2 (JCPDS # 23-0677) or Sn_2S_3 (JCPDS # 30-1379) were observed in the XRD spectra within the measurement accuracy of the instrument.

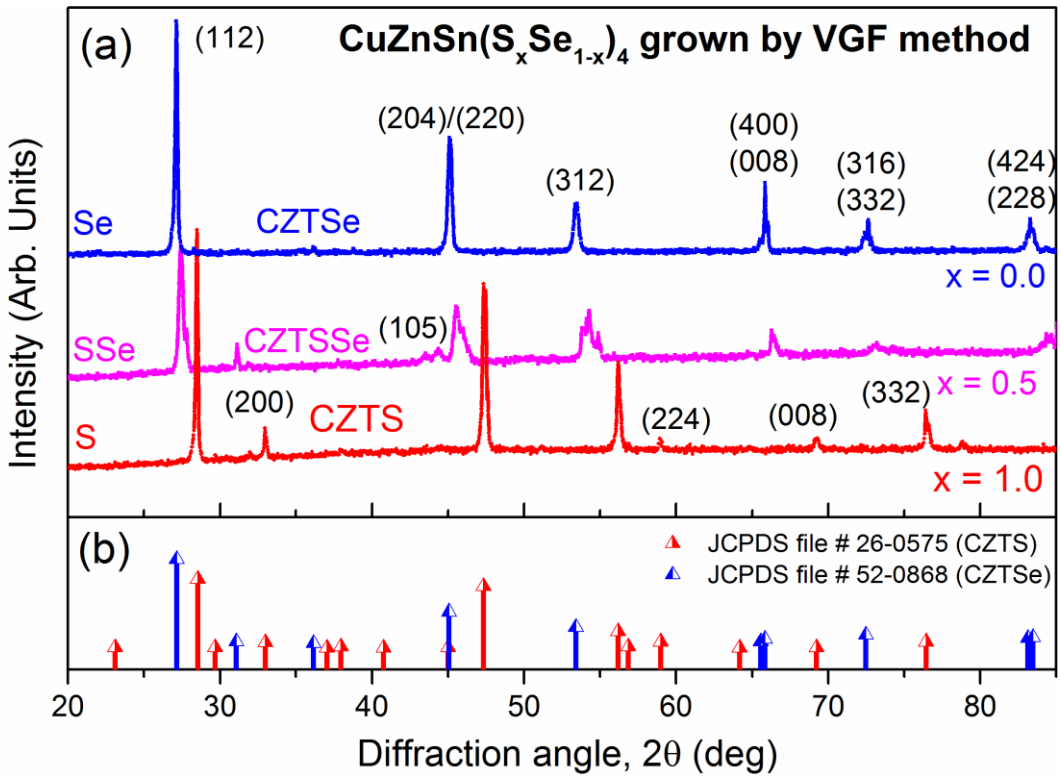

Figure 6.7. (a) Powder X-ray diffraction pattern of VGF grown $Cu_2ZnSn(S_xSe_{1-x})_4$ crystals and (b) reference kesterite CZTS and CZTSe peaks (JCPDS # 00-026-0575, 00-052-0868).

For CZTSe crystal, strong diffraction peaks at 2θ = 27.16°, 45.10°, 53.41°, 65.57°, 72.49°, and 83.28° corresponding to reflections from (112), (204), (312), (400/008), (316), and (424/228) planes of kesterite CZTSe structure (JCPDS # 00-052-0868) were observed. The strongest diffraction peak corresponding to (112) plane located at 2θ = 27.16° was fitted with a Gaussian and a narrow FWHM of ~0.146° was estimated suggesting high quality single crystalline nature of the grown material. The lattice constants for CZTSe were calculated to be a = 5.696 Å and c = 11.338 Å, which are in good agreement with the standard values of a = 5.693 Å and c = 11.333 Å reported in the literature.

The as-grown CZTSSe crystals showed X-ray diffraction peaks centered at 2θ = 27.48°, 45.52°, 54.28° and 85.08° corresponding to (112), (204/220), (312), and (424/228)

crystal planes of kesterite CZTSSe. Lattice constants of a = 5.563 Å and c = 11.09 Å were calculated from XRD analysis. The c/2a ratio is 0.997, slightly less than 1 which is consistent with literature reports. The lattice constants of the three crystals are summarized in Table 6.2.

Table 6.2. Summary of the lattice parameters calculated from PXRD data for grown $Cu_2ZnSn(S_xSe_{1-x})_4$ crystals.

Grown Crystal	Lattice parameters			
	a	c	c/2a	(112) peak position (2θ)
CZTS	5.429	10.847	0.999	28.50°
CZTSe	5.696	11.338	0.995	27.16°
CZTSSe	5.563	11.09	0.997	27.48°

It is difficult to conclude about the phase purity of kesterites based on XRD only, due to close proximity and overlapping of the secondary phase peaks. Therefore, Raman spectroscopy was performed to further investigate the presence of any undesired binary or ternary phases in the grown crystals. The Raman spectra of the CZTS and CZTSe crystals are shown in Figure 6.8. The CZTS crystal showed three Raman peaks at 287 cm^{-1}, 338 cm^{-1} and 368 cm^{-1} which are the characteristic peaks for kesterite CZTS and are in well agreement with the literature. The strongest peak observed at 338 cm^{-1} is due to the A1 symmetry in CZTS arising from S atom vibrations. No additional peaks corresponding to other impurity phases; such as β-ZnS (355 cm^{-1}), $Cu_{2-x}S$ (475 cm^{-1}), SnS (192/218 cm^{-1}), SnS_2 (317 cm^{-1}) or Cu_2SnS_3 (318 cm^{-1}) were observed, which confirmed the formation of high quality single phase kesterite CZTS.

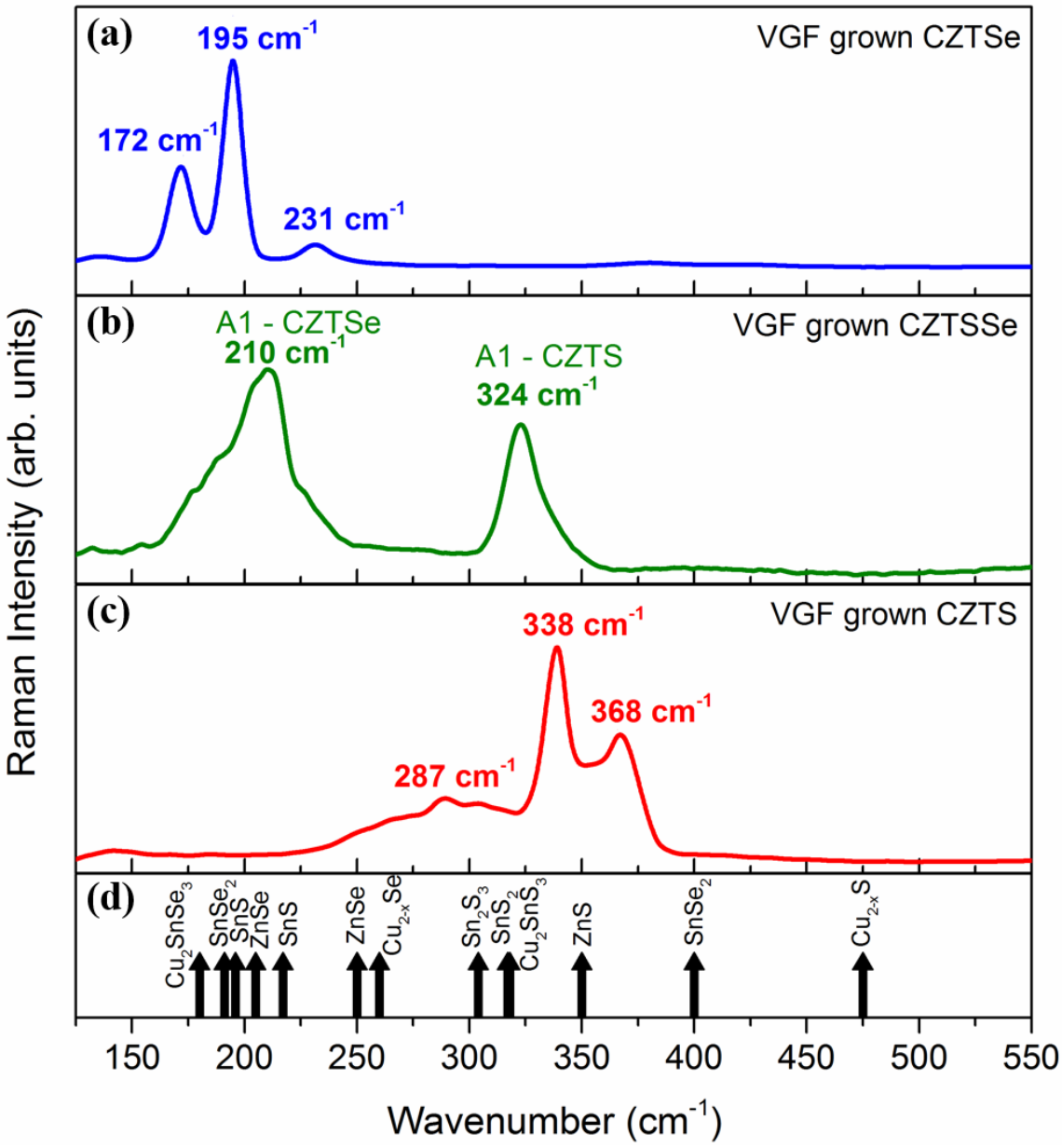

Figure 6.8. Raman spectra of the VGF grown (a) CZTSe, (b) CZTSSe, (c) CZTS bulk crystals, and (d) reference Raman peak positions for different possible secondary phases.

The Raman spectra of the CZTSe crystals exhibited three peaks at 171.5 cm^{-1}, 194.6 cm^{-1}, and 231.1 cm^{-1} corresponding to kesterite CZTSe and are found to be in well agreement with the literature. The strongest peak observed at 194.6 cm^{-1} is attributed to the

A1 mode vibration of Se atoms in CZTSe. No peaks corresponding to other binary or ternary phases; such as $Cu_{2-x}Se$ (260 cm^{-1}), ZnSe (205/251 cm^{-1}), $SnSe_2$ (191/400 cm^{-1}), or Cu_2SnSe_3 (180 cm^{-1}) were observed confirming the phase purity of the grown crystal.

X-ray photoelectron spectroscopy (XPS) measurements were performed on powdered $Cu_2ZnSn(S_xSe_{1-x})_4$ samples to analyze the electronic states of the grown crystals. The XPS survey spectrum of the crystals are shown in Figure 6.9. Strong photoelectron lines from Cu, Zn, Sn, Se, and S core levels along with carbon (C) and oxygen (O) lines are detected. The photoelectron peaks of interest and the pronounced auger peaks are identified and indexed in Figure 6.9.

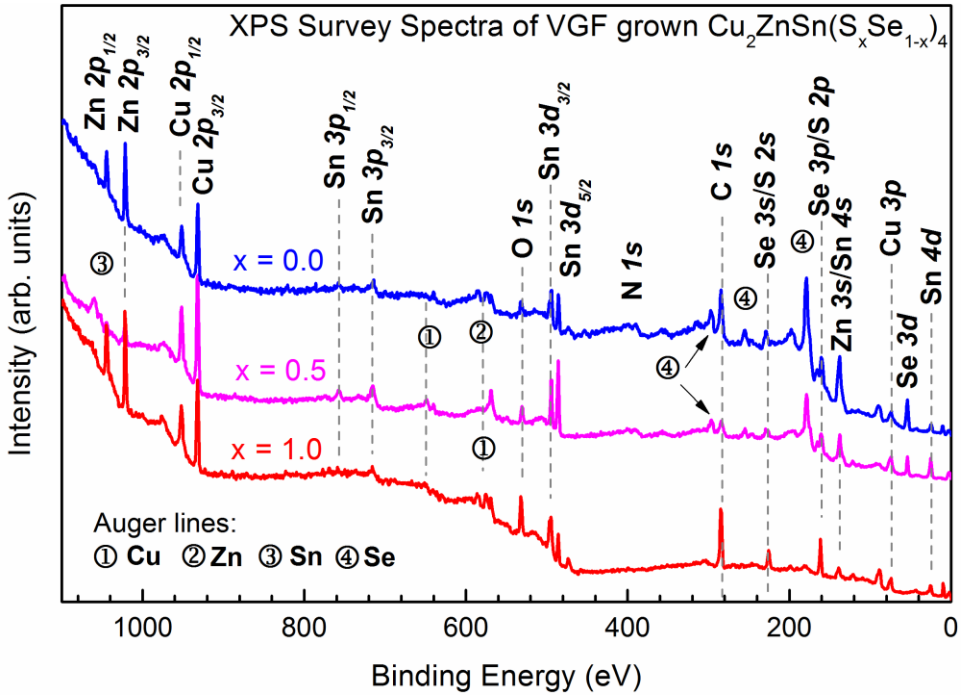

Figure 6.9. XPS survey spectrum of the VGF grown $Cu_2ZnSn(S_xSe_{1-x})_4$ crystals showing the major photoelectron lines and auger lines.

High resolution spectra of Cu 2p, Zn 2p, Sn 3d, Se 3d, and S 2p core levels were acquired to determine the electronic states of the elements. Since the XPS observations for

all three crystals were similar, only the results of CZTSSe crystal is discussed in this section. The high resolution XPS spectra for CZTSSe crystal are shown in Figure 6.10. Cu 2p, Zn 2p, and Sn 3d core levels were found to be split into two spin orbitals— $2p_{1/2}$, $2p_{3/2}$, and $3d_{1/2}$, $3d_{3/2}$, respectively. S 2p and Se 3p peaks were merged together and Se $3d_{3/2}$ and $3d_{5}/2$ spin orbitals were overlapped. The superimposed peaks were de-convoluted using XPS peak fitting program to locate precise peak positions. A Shirley background subtraction was applied for all Gaussian peak fittings.

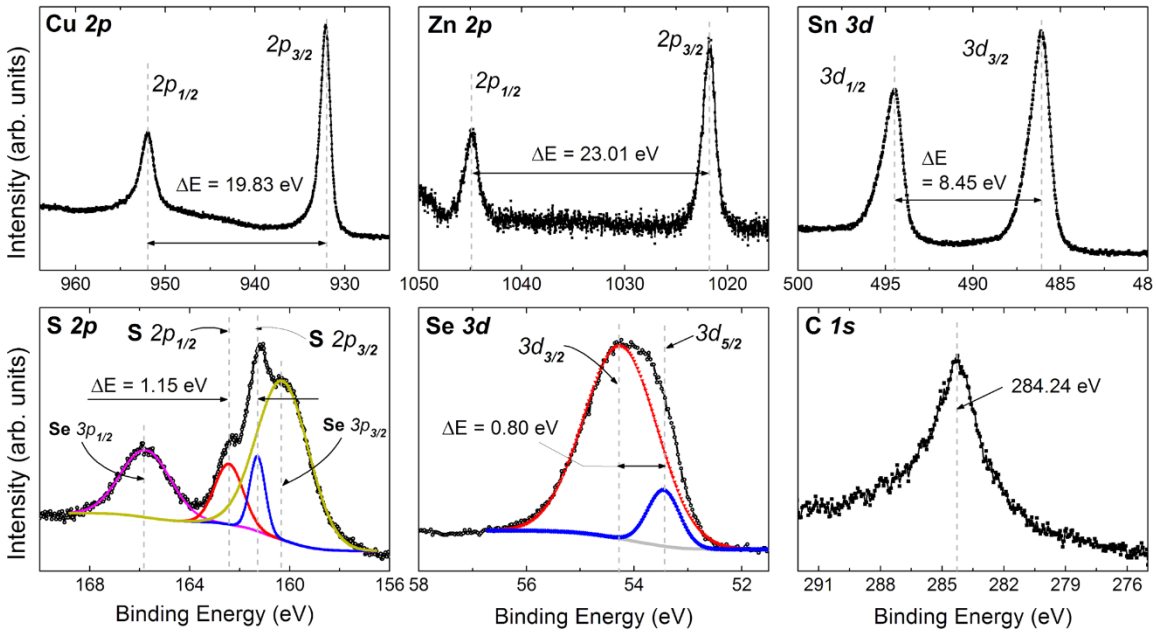

Figure 6.10. High resolution XPS spectra of Cu *2p*, Zn *2p*, Sn *3d*, S *2p*, Se *3d*, and C *1s* core levels for CZTSSe crystal.

The two spin orbits of Cu 2p core levels were split into a doublet separated by ΔE=19.83 eV ($2p_{1/2}$ at 951.94 eV and $2p_{3/2}$ at 932.11 eV), which is indicative of Cu (I). The Zn 2p core level orbitals at 1044.82 eV and 1021.81 eV corresponding to $2p_{1/2}$ and $2p_{3/2}$ with a peak separation of ΔE=23.01 eV suggests the presence of Zn (II) state. Sn 3d spin orbitals, ($3d_{3/2}$ located at 494.51 eV and $3d_{5/2}$ located at 486.06 eV) can be attributed

to the existence of Sn (IV) electronic state. The S 2p doublet separated by an energy gap of 1.15 eV ($2p_{1/2}$ at 162.43 eV and $2p_{3/2}$ at 161.28 eV) and Se 3d doublet separation of 0.80 eV ($3d_{3/2}$ at 54.25 eV and $3d_{5/2}$ at 53.45 eV) can be assigned to the formation of metal sulfo-selenides, which are consistent with the standard reference values. The peak positions, FWHM, and energy separation between the split orbitals (ΔE) for all elements are summarized in Table 6.3.

Table 6.3. Summary of XPS core level peak parameters (CZTSSe).

Core level	Binding energy (eV)	FWHM	Peak separation, ΔE (eV)
Cu $2p_{1/2}$	951.94	1.92	19.83
Cu $2p_{3/2}$	932.11	1.43	
Zn $2p_{1/2}$	1044.82	1.60	23.01
Zn $2p_{3/2}$	1021.81	1.54	
Sn $3d_{3/2}$	494.51	1.28	8.45
Sn $3d_{5/2}$	486.06	1.33	
Se $3d_{3/2}$	54.25	1.61	0.80
Se $3d_{5/2}$	53.45	0.70	
S $2p_{1/2}$	162.43	1.33	1.15
S $2p_{3/2}$	161.28	0.73	
C 1s	284.24	2.41	-
O 1s	530.78	2.37	-

EDS measurements were performed on the crystals to investigate the compositional uniformity and stoichiometry. EDS measurements at different spots along the ingot growth direction showed a uniform and nearly stoichiometric composition for all crystal ingots.

For CZTS, a Cu-poor, Zn-rich and S-rich composition was observed, which is consistent with the literature report on CZTS single crystal growth. The average atomic concentration was nearly stoichiometric (Cu:Zn:Sn:S = 24.3:12.8:12.4:50.5) with a Zn/Sn ratio of 1.03 and Cu/(Zn+Sn) ratio of 0.964. For CZTSe, the average atomic concentration was measured to be Cu:Zn:Sn:Se = 24.9:12.4:12.6:50.1 with a Zn/Sn ratio of 0.98 and Cu/(Zn+Sn) ratio of 0.996. CZTSSe crystal showed a slightly Cu-poor, Zn-rich, and Sn-rich stoichiometry with calculated average elemental ratios of Cu/(Zn+Sn) = 0.941, Zn/Sn = 0.980, and S/Se ratio of 1.02 (x=0.505) corresponding to a compound composition of $Cu_2Zn_{1.05}Sn_{1.07}(S_{0.523}Se_{0.512})_4$. The compositional data is summarized in Table 6.4.

Table 6.4. Summary of elemental composition in the grown $Cu_2ZnSn(S_xSe_{1-x})_4$ crystals measured by EDS.

Composition of $Cu_2ZnSn(S_xSe_{1-x})_4$ bulk crystals						Elemental ratios	
Crystal	Cu (at%)	Zn (at%)	Sn (at%)	S (at%)	Se (at%)	$\frac{Cu}{(Zn+Sn)}$	$\frac{Zn}{Sn}$
CZTS	24.3	12.8	12.4	50.5	-	0.964	1.03
CZTSe	24.9	12.4	12.6	-	50.1	0.996	0.98
CZTSSe	24.7	13.0	13.3	24.7	24.3	0.941	0.98

6.4 CONCLUSIONS

Large grain polycrystalline $Cu_2ZnSn(S_x,Se_{1-x})_4$ bulk material was grown via vertical gradient freeze (VGF) technique employing a directional cooling and accelerated

rotation. Structural and compositional investigation of the grown ingots revealed highly crystalline tetragonal structure corresponding to kesterite $Cu_2ZnSn(S_x,Se_{1-x})_4$. Our results show that large volume of PV-grade CZTSSe compound can be grown at low-cost via vertical gradient freeze method.

CHAPTER 7: CONCLUSION AND FUTURE WORK

7.1 DISSERTATION CONCLUSION

In this dissertation, a comprehensive investigation has been undertaken on the $Cu_2ZnSn(S_xSe_{1-x})_4$ absorber material growth, thin-film solar cell fabrication, solar cell characterization, and identification of the performance limiting factors that may lead to further improvement of CZTSSe-based photovoltaic devices.

CZTSSe photovoltaic absorber was grown by a two-step process and after composition optimization, a 4.06% efficient solar cell was obtained. Structural, compositional, and morphological properties of the absorber films were studied. Electrical characterization of the solar cells were performed and were compared with a high efficiency CZTSe cell prepared at NREL by a single-step co-evaporation process. CZTSSe cell performance was hindered by a high series resistance. From the SEM study of the device microstructure, origination of the high series resistance was attributed to the formation of micro air voids near the back contact that reduces the effective contact area significantly impeding charge collection, formation of smaller grains, and a $Mo(SSe)_x$ interfacial layer. A dominant recombination mechanism phenomena at the heterojunction interface was detected and impedance analysis showed the presence of a frequency dependent constant phase element in the device, most likely the dominant recombination process. Electrically active defect levels in the solar cells were probed by I-DLTS. Two deep levels, Cu_{Zn} and Cu_{Sn} antisites were identified in the low performance cells suggesting the detrimental effect of these defects in CZTSSe solar cells.

Also, bulk CZTSSe crystals were successfully grown by a novel vertical gradient freeze technique and were found to be a potential method to grow large volume of high quality, single phase PV grade CZTSSe production.

7.2 FUTURE WORK

The research work presented in this dissertation is expected to significantly contribute to the ongoing development of CZTSSe-based solar cells. Several important future work are suggested based on the findings of this research as summarized below:

- Improvement of the cell efficiency can be achieved by further optimization of the composition and process parameters. Such study will narrow down the range of composition and will ensure reproducibility to fabricate a high efficiency solar cell.
- In this dissertation, CZTSSe solar cells were fabricated by a two-step process and the cell characteristics were compared with a high-efficiency CZTSe cell prepared by a single-step co-evaporation process. For a more detailed comparison, cells with CZTSe absorber films should be prepared by the two-step process. This will allow a direct comparison of the cell performance with the absorber layer composition and absorber film fabrication method. Also, this study can be extended for purely sulfur based CZTS devices in future.
- The DLTS measurements were carried out in current-mode. More sensitive capacitance-mode DLTS (C-DLTS) measurement could reveal other defect levels that possibly could not be identified by I-DLTS. Thus, defect study using other techniques are suggested.

- Impedance spectroscopy (IS) was performed at room temperature under dark condition. A temperature dependent IS study is suggested in future that can reveal many other information of the device including defect levels.
- Defect level characterization of the bulk crystals are necessary to correlate with the results obtained for thin-film CZTSSe absorber. Schottky diodes may be fabricated on the bulk CZTSSe crystals to carry out DLTS measurements. This investigation may also lead to a deeper understanding of CZTSSe film growth mechanism.

REFERENCES

[1] [Online]. Available: https://www.iea.org/publications/freepublications/publication/pv_roadmap.pdf.

[2] M. A. Green, K. Emery, Y. Hishikawa, W. Warta and E. Dunlop, "Solar cell efficiency tables (version 42)," *Progress in Photovoltaics: Research and Applications,* vol. 21, pp. 827-837, 2013.

[3] M. A. Green, "Estimates of Te and In prices from direct mining of known ores," *Progress in Photovoltaics: Research and Applications,* vol. 17, pp. 347-359, 2009.

[4] C. S. Tao, J. Jiang and M. Tao, "Natural resource limitations to terawatt-scale solar cells," *Solar Energy Materials and Solar Cells,* vol. 95, pp. 3176-3180, 2011.

[5] A. Feltrin and A. Freundlich, "Material considerations for terawatt level deployment of photovoltaics," *Renewable Energy,* vol. 33, pp. 180-185, 2008.

[6] A. Zuser and H. Rechberger, "Considerations of resource availability in technology development strategies: The case study of photovoltaics," *Resources, Conservation and Recycling,* vol. 56, pp. 56-65, 2011.

[7] V. Fthenakis, "Sustainability of photovoltaics: The case for thin-film solar cells," *Renewable and Sustainable Energy Reviews,* vol. 13, pp. 2746-2750, 2009.

[8] C. Wadia, A. P. Alivisatos and D. M. Kammen, "Materials Availability Expands the Opportunity for Large-Scale Photovoltaics Deployment," *Environmental Science & Technology,* Vols. 2072-2077, p. 43, 2009.

[9] C. Candelisea, J. F. Speirsa and R. J. K. Grossa, "Materials availability for thin film (TF) PV technologies development: A real concern?," *Renewable and Sustainable Energy Reviews,* vol. 15, pp. 4972-4981, 2012.

[10] M. A. Green, "Consolidation of thin-film photovoltaic technology: the coming decade of opportunity," *Progress in Photovoltaics: Research and Applications,* vol. 14, pp. 383-392, 2006.

[11] U. S. Department of Energy, "Critical Materials Strategy," 2010.

[12] European Commission, "Critical Raw Materials for the EU," 2010.

[13] B. O'Neill, "Indium market forces, a commercial perspective," in *Photovoltaic Specialists Conference (PVSC), 35th IEEE*, Hawaii, 2010.

[14] V. M. Fthenakis and P. D. Moskowitz, "Thin-film Photovoltaic Cells: Health and Environmental Issues in their Manufacture Use and Disposal," *Progress in Photovoltaics: Research and Applications,* vol. 3, pp. 295-306, 1995.

[15] I. Repins, C. Beall, N. Vora, C. DeHart, D. Kuciauskas, P. Dippo, B. To, J. Mann, W.-C. Hsu, A. Goodrich and R. Noufi, "Co-evaporated $Cu_2ZnSnSe_4$ films and devices," *Solar Energy Materials and Solar Cells,* vol. 101, pp. 154-159, 2012.

[16] S. Bag, O. Gunawan, T. Gokmen, Y. Zhu, T. K. Todorov and D. B. Mitzi, "Low band gap liquid-processed CZTSe solar cell with 10.1% efficiency," *Energy and Environmental Science,* vol. 5, pp. 7060-7065, 2012.

[17] I. D. Olekseyuk, L. D. Gulay, I. V. Dydchak, L. V. Piskach, O. V. Parasyuk and O. V. Marchuk, "Single crystal preparation and crystal structure of the $Cu_2Zn/Cd,Hg/SnSe_4$ compounds," *Journal of Alloys and Compounds,* vol. 340, pp. 141-145, 2002.

[18] K. Wang, O. Gunawan, T. Todorov, B. Shin, S. J. Chey, N. A. Bojarczuk, D. Mitzi and S. Guha, "Thermally evaporated Cu_2ZnSnS_4 solar cells," *Applied Physics Letters,* vol. 97, p. 143508, 2010.

[19] Q. Guo, G. M. Ford, W.-C. Yang, B. C. Walker, E. A. Stach, H. W. Hillhouse and R. Agrawal, "Fabrication of 7.2% Efficient CZTSSe Solar Cells Using CZTS Nanocrystals," *Journal of the American Chemical Society,* vol. 132, pp. 17384-17386, 2010.

[20] A. Willoughby, "Solar Cell Materials: Developing Technologies," in *Wiley Series in Materials for Electronic & Optoelectronic Applications*, John Wiley & Sons, 2014, p. 186.

[21] [Online]. Available: http://www.webelements.com/.

[22] "U.S. geological survey," [Online]. Available: http://minerals.usgs.gov/minerals/pubs/commodity/.

[23] [Online]. Available: http://www.metalprices.com/.

[24] W. Shockley and H. J. Queisser, "Detailed Balance Limit of Efficiency of p-n Junction Solar Cells," *Journal of Applied Physics,* vol. 32, p. 510, 1961.

[25] G. P. Bernardini, D. Borrini, A. Caneschi, F. D. Benedetto, D. Gatteschi, D. Ristori and M. Romanelli, "EPR and SQUID magnetometry study of Cu2FeSnS4 (stannite) and Cu_2ZnSnS_4 (kesterite)," *Physics and Chemistry of Minerals,* vol. 27, pp. 453-461, 2000.

[26] S. R. Hall, J. T. Szymanski and J. M. Stewart, "Kesterite, $Cu_2(Zn,Fe)SnS_4$, and stannite, $Cu_2(Fe,Zn)SnS_4$, structurally similar but distinct minerals," *The Canadian Mineralogist,* vol. 16, pp. 131-137, 1978.

[27] L. O. Brockway, "The crystal structure of stannite Cu_2FeSnS_4," *Zeitschrift für Kristallographie – Crystalline Materials,* vol. 89, pp. 434-441, 1934.

[28] P. Bonazzi, L. Bindi, G. P. Bernardini and S. Menchetti, "A model for the mechanism of incorporation of Cu, Fe and Zn in the stannite – kesterite series, $Cu_2FeSnS_4 – Cu_2ZnSnS_4$," *The Canadian Mineralogist,* vol. 41, pp. 639-647, 2003.

[29] S. Schorr, "Structural aspects of adamantine like multinary chalcogenides," *Thin Solid Films,* vol. 515, pp. 5985-5991, 2007.

[30] D. B. Mitzi, O. Gunawan, T. K. Todorov, K. Wang and S. Guha, "The path towards a high-performance solution-processed kesterite solar cell," *Solar Energy Materials and Solar Cells,* vol. 95, pp. 1421-1436, 2011.

[31] S. Schorr, "The crystal structure of kesterite type compounds: A neutron and X-ray diffraction study," *Solar Energy Materials and Solar Cells,* vol. 95, pp. 1482-1488, 2011.

[32] C. R. A. Catlow, Z. X. Guo, M. Miskufova, S. A. Shevlin, A. G. H. Smith, A. A. Sokol, A. Walsh, D. J. Wilson and S. M. Woodley, "Advances in computational studies of energy materials," *Philosophical Transactions of the Royal Society A,* vol. 368, pp. 3379-3456, 2010.

[33] C. Persson, "Electronic and optical properties of Cu_2ZnSnS_4 and $Cu_2ZnSnSe_4$," *Journal of Applied Physics,* vol. 107, p. 053710, 2010.

[34] S. Chen, X. G. Gong, A. Walsh and S.-H. Wei, "Crystal and electronic band structure of Cu_2ZnSnX_4 (X=S and Se) photovoltaic absorbers: First-principles insights," *Applied Physics Letters,* vol. 94, p. 041903, 2009.

[35] J. Paier, R. Asahi, A. Nagoya and G. Kresse, "Cu_2ZnSnS_4 as a potential photovoltaic material: A hybrid Hartree-Fock density functional theory study," *Physical Review B,* vol. 79, p. 115126, 2009.

[36] A. Walsh, S. Chen, X. G. Gong and S. Wei, "Crystal structure and defect reactions in the kesterite solar cell absorber Cu_2ZnSnS_4 (CZTS): Theoretical insights," in *AIP Conference Proceedings*, 2011.

[37] A. Walsh, S. H. Wei, S. Y. Chen and X. G. Gong, "Design of quaternary chalcogenide photovoltaic absorbers through cation mutation," in *Photovoltaic Specialists Conference, 34th IEEE*, Philadelphia, 2009.

[38] A. Walsh, S. Chen, S. Wei and X. Gong, "Kesterite Thin-Film Solar Cells: Advances in Materials Modelling of Cu_2ZnSnS_4," *Advanced Energy Materials,* vol. 2, pp. 400-409, 2012.

[39] Y. Zhang, X. Sun, P. Zhang, X. Yuan, F. Huang and W. Zhang, "Structural properties and quasiparticle band structures of Cu-based quaternary semiconductors for photovoltaic applications," *Journal of Applied Physics,* vol. 111, p. 063709, 2012.

[40] J. M. Raulot, C. Domain and J. F. Guillemoles, "Ab initio investigation of potential indium and gallium free chalcopyrite compounds for photovoltaic application," *Journal of Physics and Chemistry of Solids,* vol. 66, pp. 2019-2023, 2005.

[41] H. Nozaki, T. Fukano, S. Ohta, Y. Seno, H. Katagiri and K. Jimbo, "Crystal structure determination of solar cell materials: Cu_2ZnSnS_4 thin films using X-ray anomalous dispersion," *Journal of Alloys and Compounds,* vol. 524, pp. 22-25, 2012.

[42] S. Siebentritt and S. Schorr, "Kesterites—a challenging material for solar cells," *Progress in Photovoltaics: Research and Applications,* vol. 20, pp. 512-519, 2012.

[43] S. Chen, X. G. Gong, A. Walsh and S. H. Wei, "Electronic structure and stability of quaternary chalcogenide semiconductors derived from cation cross-substitution of II-VI and I-III-VI_2 compounds," *Physical Review B,* vol. 79, p. 165211, 2009.

[44] I. D. Oleksyuk, I. V. Dudchar and L. V. Piskach, "Phase equilibria in the Cu_2S–ZnS–SnS_2 system," *Journal of Alloys and Compounds,* vol. 368, pp. 135-143, 2004.

[45] I. V. Dudchak and L. V. Piskach, "Phase equilibria in the Cu_2SnSe_3–$SnSe_2$–ZnSe system," *Journal of Alloys and Compounds,* vol. 351, pp. 145-150, 2003.

[46] S. Das, R. M. Krishna, S. Ma and K. C. Mandal, "Single phase polycrystalline Cu_2ZnSnS_4 grown by vertical gradient freeze technique," *Journal of Crystal Growth,* vol. 381, pp. 148-152, 2013.

[47] S. Das and K. C. Mandal, "$Cu_2ZnSnSe_4$ Photovoltaic Absorber Grown by Vertical Gradient Freeze Technique," *Japanese Journal of Applied Physics,* vol. 52, p. 125502, 2013.

[48] A. Nagoya, R. Asahi, R. Wahl and G. Kresse, "Defect formation and phase stability of Cu_2ZnSnS_4 photovoltaic material," *Physical Review B,* vol. 81, p. 113202, 2010.

[49] S. Y. Chen, X. G. Gong, A. Walsh and S. H. Wei, "Defect physics of the kesterite thin-film solar cell absorber Cu_2ZnSnS_4," *Applied Physics Letters,* vol. 96, p. 021902, 2010.

[50] P. J. Dale, K. Hoenes, J. Scragg and S. Siebentritt, "A review of the challenges facing kesterite based thin film solar cells," in *Photovoltaic Specialists Conference (PVSC), 34th IEEE*, Philadelphia, 2009.

[51] T. Maeda, S. Nakamura and T. Wada, "First-principles calculations of vacancy formation in In-free photovoltaic semiconductor $Cu_2ZnSnSe_4$," *Thin Solid Films,* vol. 519, pp. 7513-7516, 2011.

[52] T. Gödecke, T. Haalboom and F. Ernst, "Phase equilbiria of Cu-In-Se. I. Stable states and non-equilibrium states of the In_2Se_3-Cu_2Se subsystem," *Zeitschrift für Metallkunde,* vol. 91, pp. 622-634, 2000.

[53] S. Chen, J.-H. Yang, X. G. Gong, A. Walsh and S.-H. Wei, "Intrinsic point defects and complexes in the quaternary kesterite semiconductor Cu_2ZnSnS_4," *Physical Review B,* vol. 81, p. 245204, 2010.

[54] C. Persson, S. Lany, Y.-J. Zhao and A. Zunger, "n-type doping of $CuInSe_2$ and $CuGaSe_2$," *Physical Review B,* vol. 72, p. 035211, 2005.

[55] T. Maeda, S. Nakamura and T. Wada, "First Principles Calculations of Defect Formation in In-Free Photovoltaic Semiconductors Cu_2ZnSnS_4 and $Cu_2ZnSnSe_4$," *Japanese Journal of Applied Physics,* vol. 50, p. 04DP07, 2011.

[56] A. Redinger, D. M. Berg, P. J. Dale, R. Djemour, L. Gu¨tay, T. Eisenbarth, N. Valle and S. Siebentritt, "Route Toward High-Efficiency Single-Phase $Cu_2ZnSn(S,Se)_4$ Thin-Film Solar Cells: Model Experiments and Literature Review," *IEEE Journal of Photovoltaics,* vol. 1, pp. 200-206, 2011.

[57] A. Redinger, K. Ho¨nes, X. Fontane´, V. Izquierdo-Roca, E. Saucedo, N. Valle, A. Pe´rez-Rodrı´guez and S. Siebentritt, "Detection of a ZnSe secondary phase in coevaporated $Cu_2ZnSnSe_4$ thin films," *Applied Physics Letters,* vol. 98, p. 101907, 2011.

[58] K. Biswas, S. Lany and A. Zunger, "The electronic consequences of multivalent elements in inorganic solar absorbers: Multivalency of Sn in Cu_2ZnSnS_4," *Applied Physics Letters,* vol. 96, p. 201902, 2010.

[59] S. Siebentritt, M. Igalson, C. Persson and S. Lany, "The electronic structure of chalcopyrites—bands, point defects and grain boundaries," *Progress in Photovoltaics: Research and Applications,* vol. 18, pp. 390-410, 2010.

[60] A. Nagoya, R. Asahi and G. Kresse, "First-principles study of Cu_2ZnSnS_4 and the related band offsets for photovoltaic applications," *Journal of Physics: Condensed Matter,* vol. 23, p. 404203, 2011.

[61] S. Chen, A. Walsh, X.-G. Gong and S.-H. Wei, "Classification of Lattice Defects in the Kesterite Cu_2ZnSnS_4 and $Cu_2ZnSnSe_4$ Earth-Abundant Solar Cell Absorbers," *Advanced Materials,* vol. 25, pp. 1522-1539, 2013.

[62] Y.-T. Zhai, S. Chen, J.-H. Yang, H.-J. Xiang, X.-G. Gong, A. Walsh, J. Kang and S.-H. Wei, "Structural diversity and electronic properties of Cu_2SnX_3 (X=S, Se): A first-principles investigation," *Physical Review B,* vol. 84, p. 075213, 2011.

[63] T. M. Friedlmeier, N. Wieser, T. Walter, H. Dittrich and H. Schock, in *14th European Photovoltaic Solar Energy Conference*, 1997.

[64] T. Tanaka, T. Nagatomo, D. Kawasaki, M. Nishio, Q. X. Guo, A. Wakahara, A. Yoshida and H. Ogawa, "Preparation of Cu2ZnSnS4 thin films by hybrid sputtering," *Journal of Physics and Chemistry of Solids,* vol. 66, pp. 1978-1981, 2005.

[65] J. Zhang, L. X. Shao, Y. J. Fu and E. Q. Xie, "Cu_2ZnSnS_4 thin films prepared by sulfurization of ion beam sputtered precursor and their electrical and optical properties," *Rare Metals,* vol. 25, pp. 315-319, 2006.

[66] J. P. Leitao, N. M. Santos, P. A. Fernandes, P. M. P. Salome, A. F. d. Cunha, J. Gonzalez, G. M. Ribeiro and F. M. Matinaga, "Photoluminescence and electrical study of fluctuating potentials in Cu_2ZnSnS_4-based thin films," *Physical Review B,* vol. 84, p. 024120, 2011.

[67] K. Ito and T. Nakazawa, "Electrical and Optical Properties of Stannite-Type Quaternary Semiconductor Thin Films," *Japanese Journal of Applied Physics,* vol. 27, pp. 2094-2097, 1988.

[68] N. Nakayama and K. Ito, "Sprayed films of stannite Cu_2ZnSnS_4," *Applied Surface Science,* vol. 92, pp. 171-175, 1996.

[69] H. Katagiri, N. Sasaguchi, S. Hando, S. Hoshino, J. Ohashi and T. Yokota, "Preparation and evaluation of Cu_2ZnSnS_4 thin films by sulfurization of E-B evaporated precursors," *Solar Energy Materials and Solar Cells,* vol. 49, pp. 407-414, 1997.

[70] H. Katagiri, K. Saitoh, T. Washio, H. Shinohara, T. Kurumadani and S. Miyajima, "Development of thin film solar cell based on Cu_2ZnSnS_4 thin films," *Solar Energy Materials and Solar Cells,* vol. 65, pp. 141-148, 2001.

[71] H. Katagiri, N. Ishigaki, T. Ishida and K. Saito, "Characterization of Cu_2ZnSnS_4 Thin Films Prepared by Vapor Phase Sulfurization," *Japanese Journal of Applied Physics,* vol. 40, pp. 500-504, 2001.

[72] H. Matsushita, T. Maeda, A. Katsui and T. Takizawa, "Thermal analysis and synthesis from the melts of Cu-based quaternary compounds Cu–III–IV–VI_4 and Cu_2–II–IV–VI_4 (II=Zn, Cd; III=Ga, In; IV=Ge, Sn; VI=Se)," *Journal of Crystal Growth,* vol. 208, pp. 416-422, 2000.

[73] R. A. Wibowo, W. S. Kim, E. S. Lee, B. Munir and K. H. Kim, "Single step preparation of quaternary $Cu_2ZnSnSe_4$ thin films by RF magnetron sputtering from binary chalcogenide targets," *Journal of Physics and Chemistry of Solids,* vol. 68, pp. 1908-1913, 2007.

[74] R. A. Wibowo, E. S. Lee, B. Munir and K. H. Kim, "Pulsed laser deposition of quaternary $Cu_2ZnSnSe_4$ thin films," *Physica Status Solidi A,* vol. 204, pp. 3373-3379, 2007.

[75] T. M. Friedlmeier, H. Dittrich and H. W. Schock, in *11th International Conference on Ternary and Multinary Compounds. ICTMC-11*, Salford, UK, 1998.

[76] S. Schorr, H. J. Hoebler and M. Tovar, "A neutron diffraction study of the stannite-kesterite solid solution series," *European Journal of Mineralogy,* vol. 19, pp. 65-73, 2007.

[77] T. Washio, H. Nozaki, T. Fukano, T. Motohiro, K. Jimbo and H. Katagiri, "Analysis of lattice site occupancy in kesterite structure of Cu_2ZnSnS_4 films using synchrotron radiation x-ray diffraction," *Journal of Applied Physics,* vol. 110, p. 074511, 2011.

[78] [Online]. Available: http://rredc.nrel.gov/solar/spectra/am1.5/ASTMG173/ASTMG173.html.

[79] H. Katagiri, K. Saitoh, T. Washio, H. Shinohara, T. Kurumadani and S. Miyajima, "Development of thin film solar cell based on Cu_2ZnSnS_4 thin films," *Solar Energy Materials and Solar Cells,* vol. 65, pp. 141-148, 2001.

[80] B.-A. Schubert, B. Marsen, S. Cinque, T. Unold, R. Klenk, S. Schorr and H.-W. Schock, "Cu_2ZnSnS_4 thin film solar cells by fast coevaporation," *Progress in Photovoltaics: Research and Applications,* vol. 19, pp. 93-96, 2011.

[81] S. Das and K. Mandal, "Comparison of Cu_2ZnSnS_4 thin film properties prepared by thermal evaporation of elemental metals and binary sulfide sources," in *Photovoltaic Specialists Conference (PVSC), 38th IEEE*, Austin, Texas, 2012.

[82] B. Shin, O. Gunawan, Y. Z. Nestor, A. Bojarczuk, S. J. Chey and S. Guha, "Thin film solar cell with 8.4% power conversion efficiency using an earth-abundant Cu_2ZnSnS_4 absorber," *Progress in Photovoltaics: Research and Applications,* vol. 21, pp. 72-76, 2013.

[83] T. Kobayashi, K. Jimbo, K. Tsuchida, S. Shinoda, T. Oyanagi and H. Katagiri, "Investigation of Cu_2ZnSnS_4-Based Thin Film Solar Cells Using Abundant Materials," *Japanese Journal of Applied Physics,* vol. 44, pp. 783-787, 2005.

[84] A. Weber, H. Krauth, S. Perlt, B. Schubert, I. Kotschau, S. Schorr and H. W. Schock, "Multi-stage evaporation of Cu_2ZnSnS_4 thin films," *Thin Solid Films,* vol. 517, pp. 2524-2526, 2009.

[85] H. Katagiri, "Cu_2ZnSnS_4 thin film solar cells," *Thin Solid Films,* Vols. 480-481, pp. 426-432, 2005.

[86] A. Redinger, D. M. Berg, P. J. Dale and S. Siebentritt, "The Consequences of Kesterite Equilibria for Efficient Solar Cells," *Journal of the American Chemical Society,* vol. 133, pp. 3320-3323, 2011.

[87] H. Araki, A. Mikaduki, Y. Kubo, T. Sato, K. Jimbo, W. S. Maw, H. Katagiri, M. Yamazaki, K. Oishi and A. Takeuchi, "Preparation of Cu_2ZnSnS_4 thin films by sulfurization of stacked metallic layers," *Thin Solid Films,* vol. 517, pp. 1457-1460, 2008.

[88] B. Shin, K. Wang, O. Gunawan, K. B. Reuter, S. J. Chey, N. A. Bojarczuk, T. Todorov, D. B. Mitzi and S. Guha, in *Photovoltaic Specialists Conference (PVSC), 37th IEEE*, Seattle, 2011.

[89] H. Katagiri, K. Jimbo, S. Yamada, T. Kamimura, W. S. Maw, T. Fukano, T. Ito and T. Motohiro, "Enhanced Conversion Efficiencies of Cu_2ZnSnS_4-Based Thin Film Solar Cells by Using Preferential Etching Technique," *Applied Physics Express,* vol. 1, p. 041201, 2008.

[90] G. Zoppi, I. Forbes, R. W. Miles, P. J. Dale, J. J. Scragg and L. M. Peter, "$Cu_2ZnSnSe_4$ thin film solar cells produced by selenisation of magnetron sputtered precursors," *Progress in Photovoltaics: Research and Applications,* vol. 17, pp. 315-319, 2009.

[91] R. B. V. Chalapathy, G. S. Jung and B. T. Ahn, "Fabrication of Cu_2ZnSnS_4 films by sulfurization of Cu/ZnSn/Cu precursor layers in sulfur atmosphere for solar cells," *Solar Energy Materials and Solar Cells,* vol. 95, pp. 3216-3221, 2011.

[92] N. Momose, M. T. Htay, T. Yudasaka, S. Igarashi, T. Seki, S. Iwano, Y. Hashimoto and K. Ito, "Cu_2ZnSnS_4 Thin Film Solar Cells Utilizing Sulfurization of Metallic Precursor Prepared by Simultaneous Sputtering of Metal Targets," *Japanese Journal of Applied Physics,* vol. 50, p. 01BG09, 2011.

[93] P. A. Fernandes, P. M. P. Salomé, A. F. d. Cunha and B. Schubert, "Cu_2ZnSnS_4 solar cells prepared with sulphurized dc-sputtered stacked metallic precursors," *Thin Solid Films,* vol. 519, pp. 7382-7385, 2011.

[94] K. Jimbo, R. Kimura, T. Kamimura, S. Yamada, W. Maw, H. Araki, K. Oishi and H. Katagiri, "Cu_2ZnSnS_4-type thin film solar cells using abundant materials," *Thin Solid Films,* vol. 515, pp. 5997-5999, 2007.

[95] C. Platzer-Bj¨orkman, J. Scragg, H. Flammersberger, T. Kubart and M. Edoff, "Influence of precursor sulfur content on film formation and compositional changes in Cu_2ZnSnS_4 films and solar cells," *Solar Energy Materials and Solar Cells,* vol. 98, pp. 110-117, 2012.

[96] T. Ericson, J. J. Scragg, T. Kubart, T. Törndahl and C. Platzer-Björkman, "Annealing behavior of reactively sputtered precursor films for Cu_2ZnSnS_4 solar cells," *Thin Solid Films,* vol. 535, pp. 22-26, 2013.

[97] R. Lechner, S. Jost, J. Palm, M. Gowtham, F. Sorin, B. Louis, H. Yoo, R. A. Wibowo and R. Hock, "$Cu_2ZnSn(S,Se)_4$ solar cells processed by rapid thermal processing of stacked elemental layer precursors," *Thin Solid Films,* vol. 535, pp. 5-9, 2013.

[98] C. Steinhagen, M. G. Panthani, V. Akhavan, B. Goodfellow, B. Koo and B. A. Korgel, "Synthesis of Cu_2ZnSnS_4 Nanocrystals for Use in Low-Cost Photovoltaics," *Journal of the American Chemical Society,* vol. 131, pp. 12554-12555, 2009.

[99] Y. Cao, M. S. D. Jr., J. V. Caspar, W. E. Farneth, Q. Guo, A. S. Ionkin, L. K. Johnson, M. Lu, I. Malajovich, D. Radu, H. D. Rosenfeld, K. R. Choudhury and W. Wu, "High-Efficiency Solution-Processed $Cu_2ZnSn(S,Se)_4$ Thin-Film Solar Cells Prepared from Binary and Ternary Nanoparticles," *Journal of the American Chemical Society,* vol. 134, pp. 15644-15647, 2012.

[100] G. M. Ford, Q. Guo, R. Agrawal and H. W. Hillhouse, "Earth Abundant Element $Cu_2Zn(Sn_{1-x}Ge_x)S4$ Nanocrystals for Tunable Band Gap Solar Cells: 6.8% Efficient Device Fabrication," *Chemistry of Materials,* vol. 23, pp. 2626-2629, 2011.

[101] T. K. Todorov, J. Tang, S. Bag, O. Gunawan, T. Gokmen, Y. Zhu and D. B. Mitzi, "Beyond 11% Efficiency: Characteristics of State-of-the-Art $Cu_2ZnSn(S,Se)_4$ Solar Cells," *Advanced Energy Materials,* vol. 3, pp. 34-38, 2013.

[102] T. K. Todorov, K. B. Reuter and D. B. Mitzi, "High-Efficiency Solar Cell with Earth-Abundant Liquid-Processed Absorber," *Advanced Materials,* vol. 22, pp. E156-E159, 2010.

[103] D. A. R. Barkhouse, O. Gunawan, T. Gokmen, T. K. Todorov and D. B. Mitzi, "Device characteristics of a 10.1% hydrazine-processed $Cu_2ZnSn(Se,S)_4$ solar cell," *Progress in Photovoltaics: Research and Applications,* vol. 20, pp. 6-11, 2012.

[104] W. Wang, M. T. Winkler, O. Gunawan, T. Gokmen, T. K. Todorov, Y. Zhu and D. B. Mitzi, "Device Characteristics of CZTSSe Thin-Film Solar Cells with 12.6% Efficiency," *Advanced Energy Materials,* vol. 4, p. 1301465, 2014.

[105] S. Ahmed, K. B. Reuter, O. Gunawan, L. Guo, L. T. Romankiw and H. Deligianni, "A High Efficiency Electrodeposited Cu_2ZnSnS_4 Solar Cell," *Advanced Energy Materials,* vol. 2, pp. 253-259, 2012.

[106] R. N. Bhattacharya, "3.6%-CZTSS Device fabricated from ionic liquid electrodeposited Sn layer," *The Open Surface Science Journal,* vol. 5, pp. 21-24, 2013.

[107] A. Ennaoui, M. L. Steiner, A. weber, D. A. Ras, I. Kotschau, H. W. Schock, R. Schurr, A. Holzing, S. Jost, R. Hock, T. Vob, J. Schulze and A. Kirbs, "Cu_2ZnSnS_4 thin film solar cells from electroplated precursors: Novel low-cost perspective," *Thin Solid Films,* vol. 517, pp. 2511-2514, 2009.

[108] H. Araki, Y. Kubo, K. Jimbo, W. S. Maw, H. Katagiri, M. Yamazaki, K. Oishi and A. Takeuchi, "Preparation of Cu_2ZnSnS_4 thin films by sulfurization of co-electroplated Cu-Zn-Sn precursors," *physica status solidi C,* vol. 6, pp. 1266-1268, 2009.

[109] X. Zeng, K. F. Tai, T. Zhang, C. W. J. Ho, X. Chen, A. Huan, T. C. Sum and L. H. Wong, "$Cu_2ZnSn(S,Se)_4$ kesterite solar cell with 5.1% efficiency using spray pyrolysis of aqueous precursor solution followed by selenization," *Solar Energy Materials and Solar Cells,* vol. 124, pp. 55-60, 2014.

[110] S. Das, C. Frye, P. G. Muzykov and K. C. Mandal, "Deposition and characterization of low-cost spray pyrolyzed Cu_2ZnSnS_4 (CZTS) thin-films for large-area high- efficiency heterojunction solar cells," *ECS Transactions,* vol. 45, p. 153, 2012.

[111] T. Prabhakar and J. Nagaraju, "Device parameters of Cu_2ZnSnS_4 thin film solar cell," in *Photovoltaic Specialists Conference (PVSC), 37th IEEE*, Seattle, USA, 2011.

[112] M. Patel, I. Mukhopadhyay and A. Ray, "Structural, optical and electrical properties of spray-deposited CZTS thin films under a non-equilibrium growth condition," *Journal of Physics D: Applied Physics,* vol. 45, p. 445103, 2012.

[113] T. Washio, T. Shinji, S. Tajima, T. Fukano, T. Motohiro, K. Jimbo and H. Katagiri, "6% Efficiency Cu_2ZnSnS_4-based thin film solar cells using oxide precursors by open atmosphere type CVD," *Journal of Materials Chemistry,* vol. 22, pp. 4021-4024, 2012.

[114] A. Weber, R. Mainz and H. W. Schock, "On the Sn loss from thin films of the material system Cu–Zn–Sn–S in high vacuum," *Journal of Applied Physics,* vol. 107, p. 013516, 2010.

[115] P. A. Fernandes, P. M. P. Salomé and A. F. d. Cunha, "Precursors' order effect on the properties of sulfurized Cu_2ZnSnS_4 thin films," *Semiconductor Science and Technology,* vol. 24, p. 105013, 2009.

[116] M. Grossberg, J. Krustok, J. Raudoja, K. Timmo, M. Altosaar and T. Raadik, "Photoluminescence and Raman study of $Cu_2ZnSn(Se_xS_{1-x})_4$ monograins for photovoltaic applications," *Thin Solid Films,* vol. 519, pp. 7403-7406, 2011.

[117] S. Das and K. C. Mandal, "Growth and characterization of kesterite $Cu_2ZnSn(S_xSe_{1-x})_4$ crystals," *Materials Research Bulletin,* vol. 57, pp. 135-139, 2014.

[118] D. V. Lang, "Deep-level transient spectroscopy: A new method to characterize traps in semiconductors," *Journal of Applied Physics,* vol. 45, p. 3023, 1974.

[119] L. L. Kerr, S. S. Li, S. W. Johnston, T. J. Anderson, O. D. Crisalle, W. K. Kim, J. Abushama and R. N. Noufi, *Solid-State Electronics,* vol. 48, p. 1579, 2004.

[120] M. A. Lourenço, Y. K. Yew, K. P. Homewood, K. Durose and D. B. H. Richter, *Journal of Applied Physics,* vol. 82, p. 1423, 1997.

[121] J. A. Borsuk and R. M. Swanson, *IEEE Transactions on Electron Devices,* vol. ED 27, p. 2217, 1980.

[122] E. Kask, T. Raadik, M. Grossberg, R. Josepson and J. Krustok, "Deep defects in Cu_2ZnSnS_4 monograin solar cells," *Energy Procedia,* vol. 10, pp. 261-265, 2011.

[123] D. Colombara, S. Delsante, G. Borzone, J. M. Mitchels, K. C. Molloy, L. H. Thomas, B. G. Mendis, C. Y. Cummings, F. Marken and L. M. Peter, "Crystal growth of Cu_2ZnSnS_4 solar cell absorber by chemical vapor transport with I_2," *Journal of Crystal Growth,* vol. 364, pp. 101-110, 2013.

[124] T. Tanaka, D. Kawasaki, M. Nishio, Q. Guo and H. Ogawa, "Fabrication of Cu_2ZnSnS_4 thin films by co-evaporation," *physica status solidi C,* vol. 3, pp. 2844-2847, 2006.

[125] A. Nagaoka, K. Yoshinoa, H. Taniguchi, T. Taniyama and H. Miyake, "Preparation of Cu_2ZnSnS_4 single crystals from Sn solutions," *Journal of Crystal Growth,* vol. 341, pp. 38-41, 2012.

[126] K. Timmo, M. Altosaar, J. Raudoja, K. Muska, M. Pilvet, M. Kauk, T. Varema, M. Danilson, O. Volobujeva and E. Mellikov, "Sulfur-containing $Cu_2ZnSnSe_4$ monograin powders for solar cells," *Solar Energy Materials and Solar Cells,* vol. 94, pp. 1889-1892, 2010.

APPENDIX A – CZTSSe PRECURSOR THICKNESS CALCULATION AND J-V CHARACTERISTICS OF CZTSSe ARRAY

The thickness calculation of each layer in the stacked precursor film corresponding to a specific elemental ratio is described below. As an example, the calculations are shown here for precursor stack 3c in which the elemental atomic ratios of $\frac{Cu}{(Zn+Sn)}$ and $\frac{Zn}{Sn}$ were kept at 0.7 and 0.9 respectively. For simplicity, the ZnS layer thickness (t_{ZnS}) was kept constant at 300 nm for all films and the thickness of Cu and Sn layers were varied to achieve different elemental ratios in the precursors. Therefore, the objective is to calculate the thickness of Cu layer (t_{Cu}) and Sn layer (t_{Sn}) respectively.

Mass of ZnS layer (m_{ZnS}) = $\rho_{ZnS} \times (A \times t_{ZnS})$

Mass of Cu layer (m_{Cu}) = $\rho_{Cu} \times (A \times t_{Cu})$

Mass of Sn layer (m_{Sn}) = $\rho_{Sn} \times (A \times t_{Sn})$

No of Zn atoms in the precursor $(N_{Zn}) = \frac{L \times m_{ZnS}}{M_{ZnS}} = \frac{L \times \rho_{ZnS} \times (A \times t_{ZnS})}{M_{ZnS}}$

No of Cu atoms in the precursor $(N_{Cu}) = \frac{L \times m_{Cu}}{M_{Cu}} = \frac{L \times \rho_{Cu} \times (A \times t_{Cu})}{M_{Cu}}$

No of Sn atoms in the precursor $(N_{Sn}) = \frac{L \times m_{Sn}}{M_{Sn}} = \frac{L \times \rho_{Sn} \times (A \times t_{Sn})}{M_{Sn}}$

Where, ρ_{ZnS} = density of ZnS = 4.09 gm/cm^3, ρ_{Cu} = density of Cu = 8.93 gm/cm^3, and ρ_{Sn} = density of Sn = 7.30 gm/cm^3. M_{ZnS} = molecular weight of ZnS = 97.474 gm/mol, M_{Cu} = molecular weight of Cu = 63.546 gm/mol, and M_{Sn} = molecular weight of Sn = 118.71 gm/mol. L is the Avogadro constant.

$$\frac{Zn}{Sn} = \frac{(N_{Zn})}{(N_{Sn})} = \frac{\frac{L \times \rho_{ZnS} \times (A \times t_{ZnS})}{M_{ZnS}}}{\frac{L \times \rho_{Sn} \times (A \times t_{Sn})}{M_{Sn}}} = \frac{\rho_{ZnS} \times t_{ZnS} \times M_{Sn}}{\rho_{Sn} \times t_{Sn} \times M_{ZnS}}$$

$$\Rightarrow 0.9 = \frac{\rho_{ZnS} \times t_{ZnS} \times M_{Sn}}{\rho_{Sn} \times t_{Sn} \times M_{ZnS}}$$

$$\Rightarrow t_{Sn} = \frac{\rho_{ZnS} \times t_{ZnS} \times M_{Sn}}{0.9 \times \rho_{Sn} \times M_{ZnS}}$$

$$\Rightarrow t_{Sn}(nm) = \frac{4.09 \times 300 \times 118.71}{0.9 \times 7.30 \times 97.474}$$

$$\Rightarrow t_{Sn} = 227.45\ nm$$

Similarly,

$$\frac{Cu}{Zn + Sn} = \frac{(N_{Cu})}{(N_{Zn}) + (N_{Sn})} = \frac{\frac{L \times \rho_{Cu} \times (A \times t_{Cu})}{M_{Cu}}}{\frac{L \times \rho_{ZnS} \times (A \times t_{ZnS})}{M_{ZnS}} + \frac{L \times \rho_{Sn} \times (A \times t_{Sn})}{M_{Sn}}}$$

$$\Rightarrow 0.7 = \frac{\frac{\rho_{Cu} \times t_{Cu}}{M_{Cu}}}{\frac{\rho_{ZnS} \times t_{ZnS}}{M_{ZnS}} + \frac{\rho_{Sn} \times t_{Sn}}{M_{Sn}}}$$

$$\Rightarrow t_{Cu} = \frac{0.7 \times \left(\frac{\rho_{ZnS} \times t_{ZnS}}{M_{ZnS}} + \frac{\rho_{Sn} \times t_{Sn}}{M_{Sn}}\right) \times M_{Cu}}{\rho_{Cu}}$$

$$\Rightarrow t_{Cu}(nm) = \frac{0.7 \times \left(\frac{4.09 \times 300}{97.474} + \frac{7.30 \times 227.45}{118.71}\right) \times 63.546}{8.93}$$

$$\Rightarrow t_{Cu} = 132.38\ nm$$

J-V Characteristics under dark and under AM1.5 illumination for the cells 1, 2, 3, 5, 6, 7 of the CZTSSe array are shown below.

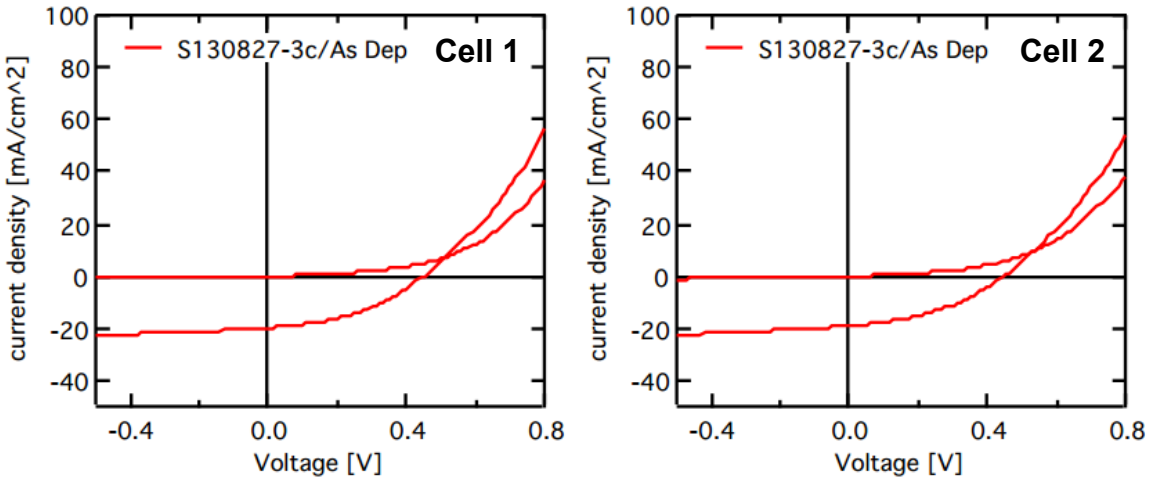

Figure A.1 J-V characteristics of cell 1 and cell 2 under dark and AM1.5 illumination.

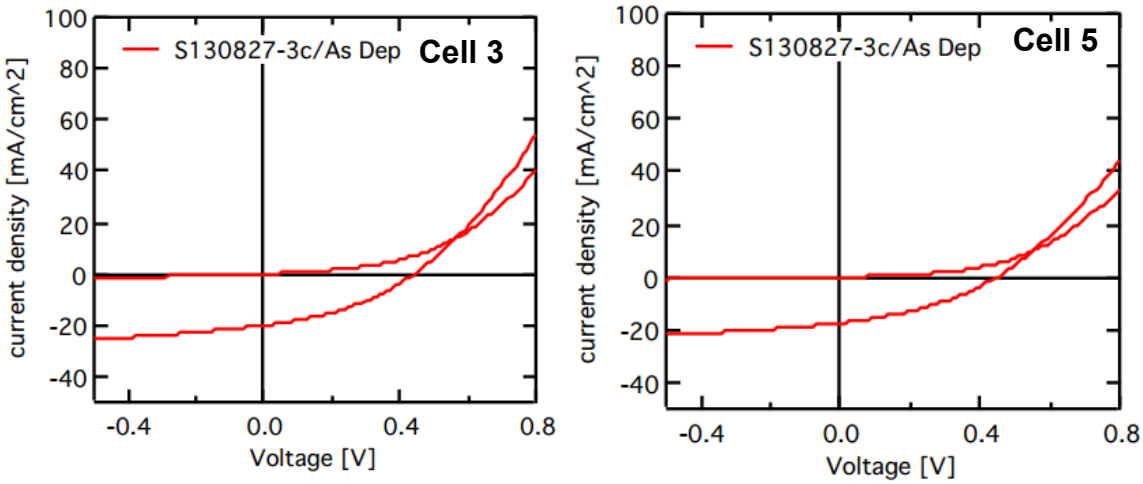

Figure A.2 J-V characteristics of cell 3 and cell 5 under dark and AM1.5 illumination.

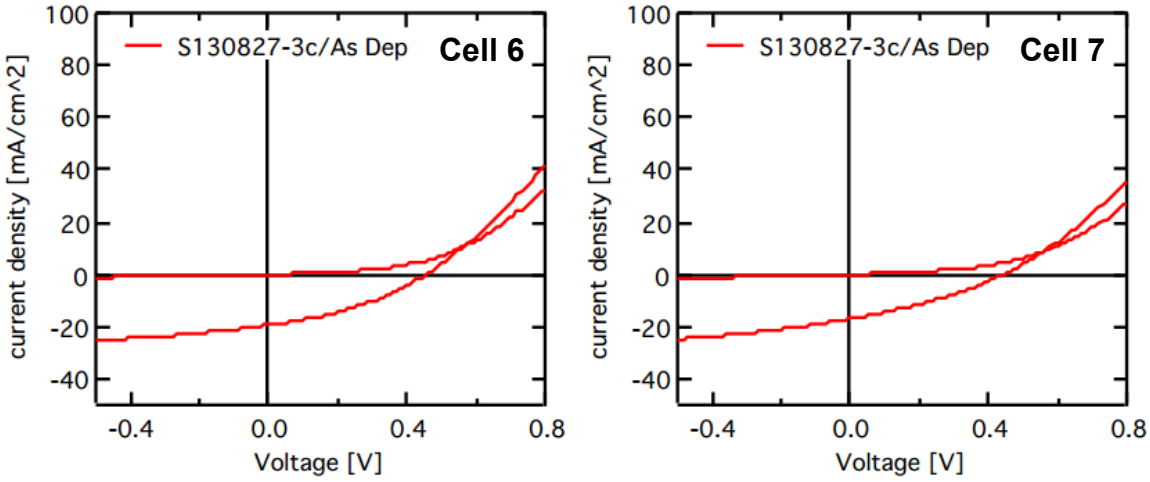

Figure A.3 J-V characteristics of cell 6 and cell 7 under dark and AM1.5 illumination.

APPENDIX B – AFM TIP DETAILS

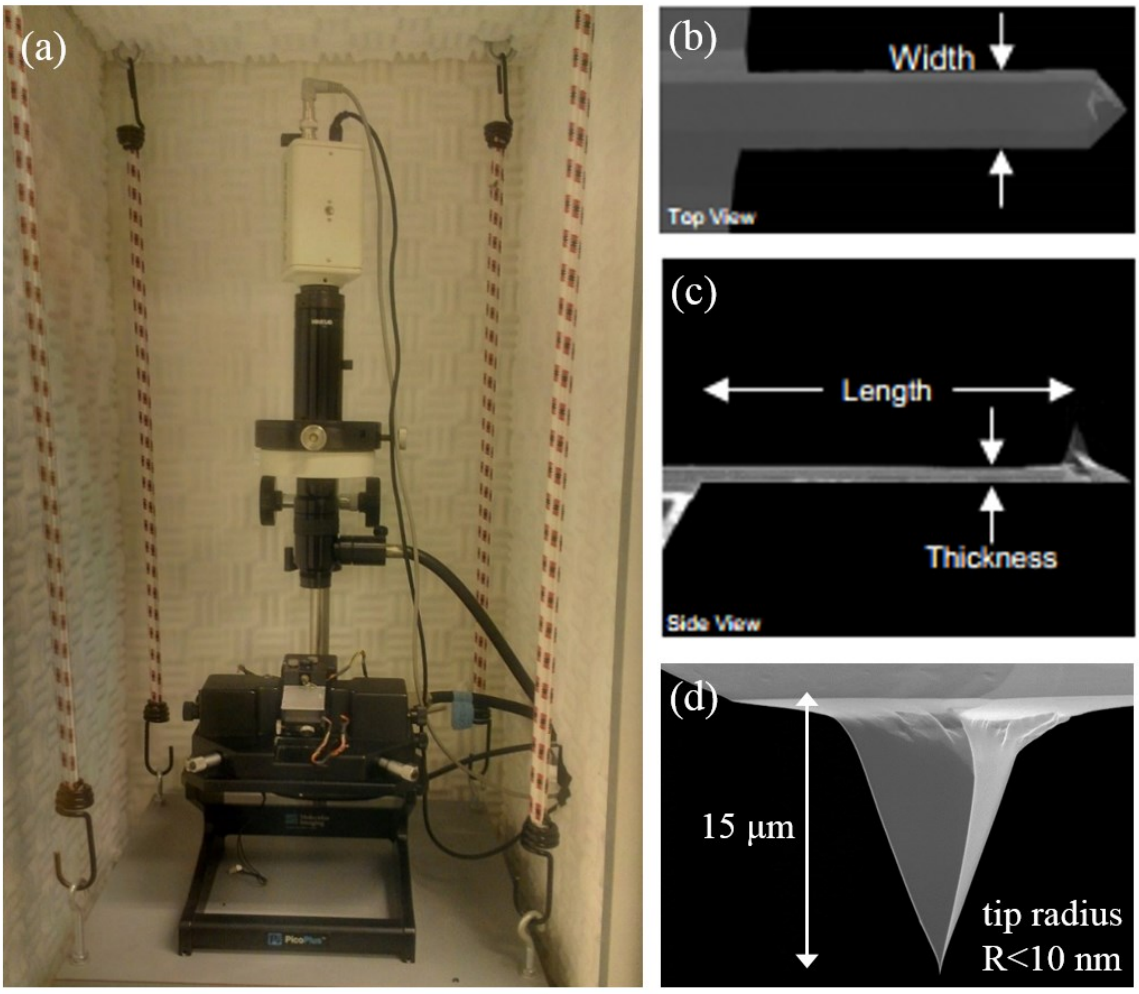

Figure B.1 (a) The Picoplus AFM setup, (b-d) SEM images showing the shape and dimensions of the Si cantilever and the tip.

Photograph of the AFM instrument (Picoplus) and SEM images of the Si cantilever/tip (AppNano A-50) are shown in Figure B.1. Tip specification from the manufacturer are summarized in Table B.1.

Table B.1 Dimensions, spring constant, and operating frequency of the Si cantilever/tip used for AFM measurements.

Parameter	Value		
	Nominal	Minimum	Maximum
Length (μm)	225	215	235
Width (μm)	27	22	32
Thickness (μm)	2.7	2.2	3.2
Spring constant (N/m)	1.6	0.6	3.7
Frequency (KHz)	61	43	81

APPENDIX C – QUARTZ AMPOULE SEALING

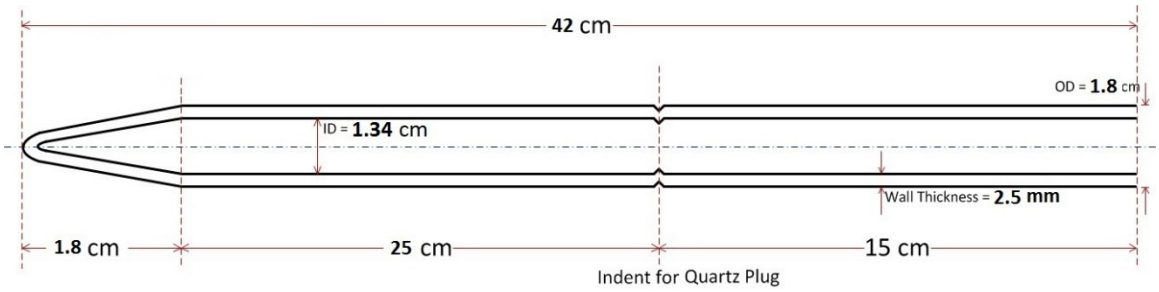

Figure C.1 CAD design of the quartz ampoule used for the CZTSSe (S/(S+Se)=0.5) bulk crystal growth by vertical gradient freeze technique.

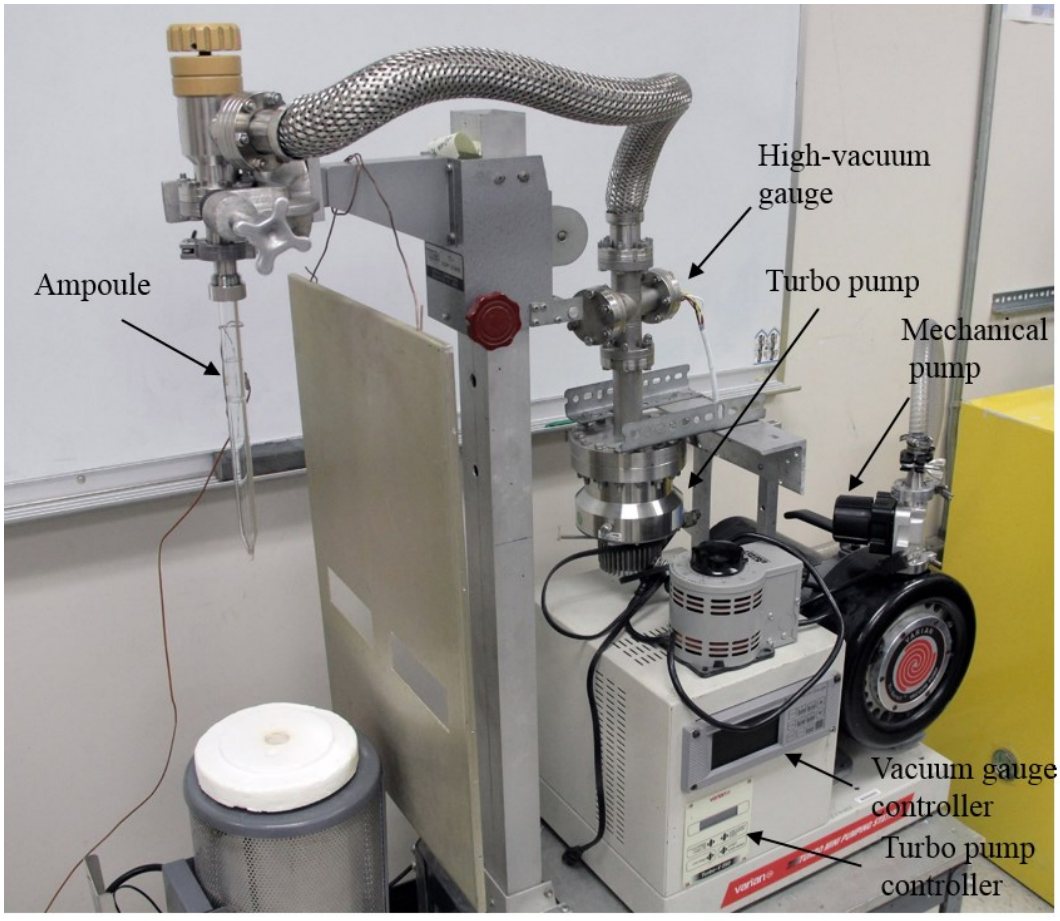

Figure C.2 In-house built quartz ampoule sealing station.